

國立交通大學
材料科學與工程研究所
博士論文

一維奈米氮化鋁的製備與光電特性分析

Synthesis and Characterization of
One-Dimensional AlN nanostructures



研究生：施士塵

指導教授：陳家富 博士

林麗瓊 博士

陳貴賢 博士

中華民國九十四年十月

一維奈米氮化鋁的製備與光電特性分析

Synthesis and Characterization of One-Dimensional AlN nanostructures

研究生：施士塵

Student: Shih-Chen Shi

指導教授：陳家富 博士

Advisor: Dr. Chia-Fu Chen

林麗瓊 博士

Dr. Li-Chyong Chen

陳貴賢 博士

Dr. Kuei-Hsien Chen

國立交通大學

材料科學與工程研究所

博士論文

A Thesis

1896

Submitted to Department of material Science and Engineering

College of Engineering

National Chiao Tung University

In partial Fulfillment of the Requirements

For the Degree of Doctor of Philosophy

In Material Science and Engineering

October 2005

Hsinchu, Taiwan, Republic of China

中華民國九十四年十月

一維奈米氮化鋁的製備與光電特性分析

研究生：施士塵

指導教授：陳家富 博士

林麗瓊 博士

陳貴賢 博士

國立交通大學材料與工程學系

摘要

利用常壓熱壁式的化學氣相沈積法(atmosphere pressure chemical vapor deposition; APCVD)，我們已成功地在矽基板上成長出氮化鋁(aluminum nitride; AlN)一維奈米晶體（包含奈米針尖- nanotips 與奈米柱- nanorod）。同時也藉由場發射掃描式電子顯微術(field-emission scanning electron microscopy; FESEM)，穿透式電子顯微術(transmission electron microscopy; TEM)，選區電子繞射術(selected-area electron diffractometry; SAED)，X 光繞射術(X-ray diffraction; XRD)，與拉曼散射(Raman scattering)等量測技術，對各式的氮化鋁樣品之形貌，結構，晶向與組成做了詳細的特性研究。應用方面，本實驗針對一維奈米氮化鋁的光學特性做了深入的研究，以及一維奈米氮化鋁基板於表面增強拉曼(surface enhanced Raman Spectroscopy; SERS)方面的特性分析，同時也針對具有奈米尖端的氮化鋁針尖做了詳盡的場發射特性研究。

論文中詳細描述了一維奈米氮化鋁的成長特性與結構分析。一維奈米氮化鋁材

料主要以氣相傳輸與凝結(vapor transport and condensation process; VTCP) 為合成的機制。在化學汽相沈積過程中，金屬鍍層的厚度控制對於一維奈米氮化鋁針尖材料的尺寸控制有很大的影響。此外，不管使用何種金屬鍍層厚度或種類，合成出來的一維奈米氮化鋁針尖具有類似的針尖角度，稱之為自我選擇的針尖角度(self-selective apex angle)。為此，我們提出了成長模型來描述一維奈米氮化鋁針尖的成長特性與機制。

針對不同的合成溫度對於一維奈米氮化鋁材料表面型態的影響也做了深入的探討。發現到了在低溫合成時(950 °C)，一維奈米氮化鋁會形成針尖狀(nanotip); 然而在高溫合成時(1200 °C)，一維奈米氮化鋁會長成柱狀 (nanorod)。為了解釋這種現象，我們引進了分子的擴散長度 (diffusion length) 以及表面能量 (Ehrlich-Schwoebel barrier) 的理論來討論一維奈米氮化鋁由低溫針尖狀轉變為高溫柱狀的現象。

一維奈米氮化鋁的光學特性方面，我們使用了陰極螢光 (cathodoluminescence), 光激發螢光 (photoluminescence), 熱螢光 (thermoluminescence), 以及紫外光吸收(UV absorption)等技術來研究分析，並觀察到了一維奈米氮化鋁材料同時具有直接能隙放光的特性以及因為氧及其它摻雜物所造成的缺陷放光特性。因此，我們提出了一維奈米氮化鋁材料的吸收與放光模型。

一維奈米氮化鋁材料於表面增強拉曼的應用上，我們利用離子束濺鍍系統將奈米銀微粒 (5-10 nm) 鍍在一維奈米氮化鋁基板上。並使用Rhodamine 6G (10^{-6} M) 當做測試的樣品。其實驗結果顯示，在拉曼強度的表現上，具有 10^6 的

增強效果。

電性方面，一維奈米氮化鋁材料成長於不同摻雜種類及電阻值的矽基板上 (p^+ , p , n^+ , and n type-Si)，來探討基板對於場發射特性的影響。針對一維奈米氮化鋁所特有的奈米尖端，其場發射的特性測試結果顯示，當一維奈米氮化鋁針尖 (AlNNTs) 成長於 p^+ -Si 基板時，此類材料具備最佳的場發射密度 (max. current density ~ 0.22 A/cm²)，其用於驅動 10 μ A/cm² 電流密度的最低啟動電場 (turn-on field) 約在 6.5 V/ μ m，且具有相當穩定的特性 (10 小時內僅 5% 變化)。反之如果將一維奈米氮化鋁材料成長於 n - or n^+ -Si 上的話，就沒有辦法得到任何的場發射電流。論文中也提出了矽-氮化鋁異質界面 (Si-AlN heterojunction) 的模型來解釋這種現象。



Synthesis and Characterization of One-Dimensional AlN nanostructures

Student : Shih-Chen Shi

Advisor : Dr. Chia-Fu Chen

Dr. Li-Chyong Chen

Dr. Kuei-Hsien Chen

National Chiao Tung University

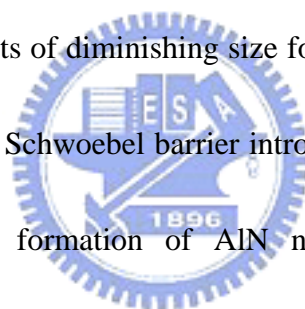
Material Science and Engineering

Abstract:

Single crystal hexagonal aluminium nitride nanotips are fabricated using vapor transport, from aluminium powders heated to 950°C in presence of ammonia gas, and condensation process (VTCP) on silicon substrates with or without catalyst layer. The resultant tips have very sharp nanoscale apexes (~ 1 nm) while their base and length up to hundreds of nm and several microns, respectively, are observed. Critical role of the gold catalyst layer thickness in controlling the size of tip has been demonstrated in addition to a catalyst-free growth mode resulting in lesser control over the nanotip morphology. Nevertheless, a remarkably narrow distribution in the apex angle of the nanotips, regardless of the use of catalyst in VTCP, has been obtained. Unlike the commonly observed ridge and pyramid structures, the nanotips produced by VTCP have higher angles (~81°) between the tilted (221) and the basal (001) planes that

encase it. A mechanism for this self-selective apex angle in aluminum nitride nanotip growth has been proposed.

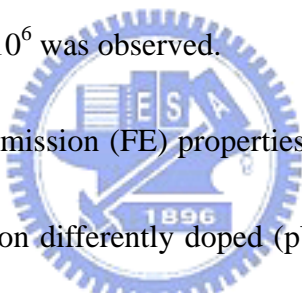
However, if we take the growth temperature as a variable parameter, but keep other condition fixed. At lower growth temperatures, around 950 °C, AlN nanotips with apex diameters of 10 nm, base diameters of ~100 nm, and length of ~2000 nm were obtained. On the other hand, as the growth temperature approached 1200 °C, we observed a broadening of the tip area, a shortening of the height and a complete transformation to AlN nanorods. Compelling microscopic evidences were obtained to show that stacked AlN platelets of diminishing size formed the building blocks of the nanotips. A reducing Ehrlich- Schwoebel barrier introduced into a diffusion mediated growth model explains the formation of AlN nanorods at increasing growth temperatures.



The optical properties of wurtzite AlN nanotips are characterized by cathodoluminescence (CL), photoluminescence (PL), thermoluminescence (TL), and UV absorption. CL measurement shows two defect related transitions around 2.1 and 3.4 eV and a well resolved excitonic feature in the near band-edge transition ~ 6.2 eV. Two broad peaks centered nearly at 2.1 and 3.4 eV were also observed from the PL and TL spectra. Analysis of the excitation spectra of both PL and TL measurements suggested the existence of multifold energy levels within the gap. The optical

absorption spectrum shows that the nanotips exhibited three absorption centers located at 6.2, 5.0, and 3.4 eV, respectively.

A new substrate for surface enhanced Raman spectroscopy has been developed in the form of AlN nanotips. The surface area of the nanotips is quiet high for the post-metal deposition. Ion beam sputtered silver self assemble on these substrates as nanoparticles of 5-10 nm diameter and these metallic nanoparticles act as surface enhancement centers for Raman spectroscopy. Standard molecule such as Rhodamine 6G of concentrations of 10^{-6} M has been studied on these substrates and enhancements in the range of 10^6 was observed.



Here, we report the field emission (FE) properties of the quasi-aligned aluminum nitride (AlN) nanotips grown on differently doped (p^+ , p , n^+ , and n type) silicon (Si) (100) substrates. The AlN nanotips grown on p^+ -type Si substrate showed the lowest turn-on field of 6 V/ μm (highest current density of 0.22 A/ cm^2 at a field of 10 V/ μm), whereas no significant emission could be obtained using n^+ - and n - type Si substrates. Band diagrams of the heterojunction between the Si substrate and the AlN nanotips have been used to explain this charge carrier related FE from wide band gap AlN nanotips. The FE from the AlN nanotips prepared on p^+ - and p - type Si substrates were found to be stable for more than 10 hours while extracting a constant current density of 100 $\mu\text{A}/\text{cm}^2$ with the applied field varying by only about 5% and 10%,

respectively.



致 謝

「因為需要感謝的人太多了，就感謝天罷。」—— 陳之藩

四年，一千五百個日子。

是痛苦，還是成長；是折磨，還是淬鍊；是頑固，還是堅持；是辛苦，還是快樂。

一切似乎都不再重要，所有的酸甜苦辣都融化在這些千百個溫馨回憶裏了。

非常感謝三位指導老師在研究上以及生活上的指導與關懷；感謝原分所與凝態中心的博士後研究員與研究助理以及學弟妹在實驗上的幫助；感謝原分所機械工廠的師傅們；感謝新竹新素材與薄膜實驗室的學長弟們；感謝所謝曾經幫助過與支持我的人。那怕是只有一句鼓勵的話，一個支持的眼神，對我來說都是意義重大的。沒有大家的熱情相挺，這些日子不會那麼快樂、對我那麼地重要。真的需要感謝的人、值得感謝的人太多了，就套用一句陳之藩的話，就感謝天吧。

最後要特別感謝我的家人和女友對我的包容與支持，尤其是父母親的無限關懷與照顧，女友 毓倫的鼓勵與叮嚀。謹以此論文獻給我最親愛的家人及朋友。

Table of Contents

	Page
Abstract (Chinese) -----	I
Abstract (English) -----	IV
Acknowledge (Chinese) -----	VIII
Table of Contents -----	IX
List of Figures -----	XII
List of Tables -----	XVI
Chapter 1	
Introduction-----	1
1.1 Preface-----	1
1.2 Nitride-based materials -----	2
1.3 Aluminum nitride -----	3
1.4 Nano-size requirement -----	4
1.5 One-dimensional nano-materials -----	5
1.6 Motivation-----	6
Chapter 2	
A brief review of growth and fundamental theory -----	8
2.1 Growth mechanism -----	8
2.1.1 Vapor-Liquid-Solid growth (VLS) -----	8
2.1.2 Vapor-Solid growth (VS) -----	11
2.2 Luminescence of semiconductor -----	11
2.3 Raman spectroscopy -----	17
2.4 Field Emission -----	27
2.4.1 Field Emission from metal -----	27
2.4.2 Field Emission from semiconductor -----	30
Chapter 3	
Experimental method-----	32
3.1 Experimental details-----	32

3.2	Atmospheric pressure chemical vapor deposition -----	32
3.3	Characterization of AlN nano-structures ---	35
3.3.1	Scanning electron microscopy (SEM)-----	35
3.3.2	Transmission electron microscopy (TEM) -	35
3.3.3	Electron energy loss spectroscopy (EELS)	35
3.3.4	X-ray diffraction spectroscopy -----	36
3.3.5	Micro-Raman spectroscopy-----	36
3.3.6	Cathodoluminescence -----	37
3.3.7	Photoluminescence -----	38
3.3.8	Thermoluminescence -----	38
3.3.9	UV absorption -----	39
3.3.10	Measurement of field emission characterization -----	39
Chapter 4	Growth of AlN nanotips by means of APCVD-----	41
4.1	AlN nanotips growth -----	41
4.2	Results and discussion -----	43
4.3	Growth mechanism of AlNNTs -----	54
4.4	Summary -----	58
Chapter 5	Structural evolution of AlN nano-structure: Nanotips and Nanorods -----	59
5.1	Nanotips and Nanorods -----	59
5.2	Structural evolution of AlN nano-structure	63
5.3	Magic ratio -----	73
5.4	Summary -----	79

Chapter 6	Luminescence of AlN nano-structures -----	80
6.1	Temperature dependent cathodoluminescence	81
6.2	Photoluminescence -----	84
6.3	Thermoluminescence -----	85
6.4	UV Absorption -----	87
6.5	Luminescence model -----	89
6.6	Summary -----	91
Chapter 7	Surface enhanced Raman properties of AlN nanotips -----	92
7.1	Experimental -----	95
7.2	Results and discussion-----	96
7.3	Summary -----	102
Chapter 8	Field emission from quasi-aligned AlNNTs	103
8.1	Experimental -----	104
8.2	Results and discussion-----	106
8.3	Summary -----	115
Chapter 9	Conclusions -----	116
Reference	-----	119
Publication		
list	-----	134
Vita	-----	136

List of Figures

FIG. 2.1	Schematic diagram of VLS growth mechanism. The nanowire growth includes three stages of (a) alloying, (b) nucleation, and (c) axial growth -----	10
FIG. 2.2	Energy diagram of (a) direct- and (b) indirect-gap semiconductors -----	14
FIG. 2.3	Schematic diagram of transitions in a semiconductor. E_c is the conduction band, E_v the valence band, E_e the exciton level, E_d the donor level, and E_a the acceptor level -----	15
FIG. 2.4	Energy gap of different compound semiconductors as a function of lattice constant -----	16
FIG. 2.5	Mechanism of (a) IR, and (b) Raman spectroscopy -----	18
FIG. 2.6	Energy levels of IR, normal Raman, resonance Raman, and fluorescence spectra. R: Rayleigh scattering, S: Stokes Raman scattering, A: anti-Stokes Raman scattering -----	22
FIG. 2.7	Crystal structure views of wurtzite along different directions: (a) $[0001]$, (b) $[11\bar{2}0]$, and (c) $[10\bar{1}0]$ -----	23
FIG. 2.8	Crystal structure views of zincblende along different directions: (a) $[100]$, (b) $[110]$, and (c) $[111]$ -----	23
FIG. 2.9	Optical phonon modes in wurtzite structure -----	25
FIG. 2.10	Diagram of potential energy of electrons at the surface of metal -----	29
FIG. 2.11	Diagram of potential energy of electrons at the surface of an n-type semiconductor with field penetration into semiconductor interior -----	31
FIG. 3.1	Schematic diagram of the atmospheric pressure chemical vapor deposition system -----	34
FIG. 4.1	Typical SEM images of the AlN nanotips grown with (a) 7 nm, (b) 15 nm, and (c) 50 nm thick Au layer on Si. (d) Typical cross section SEM image of AlN nanotips grown with 15 nm Au coated Si substrate -----	47
FIG. 4.2	SEM images of AlN nanotips grown with (a) Al (15 nm), (b) Pt (15 nm), (c) no metal coating, on the Si substrate, respectively -----	48
FIG. 4.3	SEM images of AlN nanotips grown with Au (15 nm on Si) for (a) 15 min, (b) 20 min, (c) 25 min, and (d) the corresponding TEM-EDS	

	spectra of the AlN nanotip and nanoparticle marked (A) and (B) in Fig. 3c -----	49
FIG. 4.4	(a) Typical XRD spectra taken at two different stages of growth. The initial stage shows only Al signals and the corresponding one with fully grown nanotips shows two crystalline phases of Al and hexagonal AlN. (b) Raman spectrum, with a discontinuous abscissa, of the AlN nanotips on silicon substrate. Inset shows a continuous Raman spectrum of the AlN nanotips with the silicon signal included. All the XRD and Raman spectra were measured from samples prepared on 15 nm Au coated Si substrate -----	51
FIG. 4.5	(a) TEM image of an AlN nanotip, (b) High resolution TEM image of a single AlN nanotip with clear lattice images. The inset shows a SAED pattern of the nanotip indicating the single-crystalline nature with [110] zone axis and the growth direction along [001]. (c) TEM of a single AlN nanotip with corresponding (d) Al, and (e) N mapping using EELS -----	53
FIG. 4.6	Schematic diagram of growth mechanism of AlN nanotips. (a) Au layer was coated on the Si substrate. (b) Gold or Gold-silicide nanoparticles shape up as the nucleation sites for the subsequent aluminum deposition. (c) Aluminum and nitrogen are absorbed on the nucleation sites bringing about the initial growth of AlN nanotips. (d) AlN nanotips elongate with time when reaction temperature is kept at 950 °C -----	55
FIG. 4.7	Atomic arrangement in AlN crystal showing the stable “nongrowth” surfaces of (a) (221), (b) $(\bar{1}\bar{1}1)$, and (c) $(\bar{1}\bar{1}2)$ making angles of 81°, 61° and 43°, respectively, with the basal plane. The c-axis shown in the figure is [001] direction -----	57
FIG. 5.1	Typical SEM images of the AlN nanotips on silicon substrates (coated with 15 nm of gold) grown under (a) 950, (b) 1000, (c) 1100, and (d) 1200 °C, respectively -----	60
FIG. 5.2	Typical cross section SEM image of AlN nanotips grown coated with 15 nm Au coated Si substrate under (a) 950, (b) 1200 °C, respectively. Inset in (a) and (b) show the SEM image of AlN nano-product grown	

for 25 minutes, respectively. (c) Typical XRD and (d) Raman spectra taken from the AlN nanostructures in Figure 2(a) and 2(b), respectively. The two vertical dashed lines in Figure 2(c) represent bulk AlN positions for (100) and (002) reflections (JCPDS 25-1133)---

- 62
- FIG. 5.3 (a) The cross-sectional view of hexagonally close packed wurtzite crystal structure of AlN. (b) The plan-view of a bilayer of hcp AlN. There are two types of lateral growth directions marked as A and B ---- 67
- FIG. 5.4 (a-d) High resolution SEM images of the AlN nanostructures produced at different growth temperatures; (e) HRTEM image of the edge of AlNNTs showing the step edges, including the step height (h) and step spacing (λ); a schematic aiding in the estimation of the semi apex angle ($\phi/2$) is also shown; (f) HRTEM image of the edge of AlNNRs showing uniform diameter without tapering via step edges ----- 70
- FIG. 6.1 Temperature-dependent CL spectra from AlNNTs grown on Si substrate measured between 4 to 300 K. The inset shows the near band edge transition which can be resolved into two peaks ----- 83
- FIG. 6.2 PL and PLE spectrum of AlNNTs measured at room temperature. PL were taken from by the 5.0 (\blacktriangle), and 3.5 (\bullet) eV excitation, respectively. PLE were taken with the detection at 3.2 (\triangle), and 2.1 (\circ) eV ----- 84
- FIG. 6.3 TL spectrum of AlNNTs measured at different temperature between 66 to 145°C with 206 nm excitation. TLE were observed at very near band edge ----- 86
- FIG. 6.4 UV absorption spectrum of AlNNTs showing major absorption process taking place ----- 88
- FIG. 6.5 Schematically drawing of luminescence model of AlN ----- 90
- FIG. 7.1 (a) Cross section and top view (inset) SEM image of quasi aligned AlN nanorods; (b) Top view SEM image of Ag-coated AlN nanorod; (c) Cross section view of Ag-coated AlN nanotips; (d) High magnification SEM image of Ag-coated AlN nanotips; (e) X-ray diffraction spectrum of as-grown and Ag coated AlN nanostructures clearly shows a preferred orientation along [002] ($2\theta=36.04^\circ$) ----- 97

FIG. 7.2	(a) TEM image of a single Ag-coated AlN nanorod (the arrows showing the nc-Ag); top and bottom inset shows the SAED pattern and the electron energy loss spectroscopy (EELS) spectrum of the as-grown AlN nanorod, respectively; b) HRTEM image of the as-grown AlN nanorod lattice; c) SAED pattern of the Ag-coated AlN nanorod -----	100
FIG 7.3	Raman spectrum of (a) the as-grown AlN nanorods, (b) as-grown AlN nanorods with R6G, and (c) SERS spectrum of Ag coated AlN nanorods with R6G, (d) as-grown AlN nanotips, (e) as-grown AlN nanotips with R6G, and (c) SERS spectrum of Ag coated AlN nanotips with R6G -----	102
FIG 8.1	Schematic diagram of field emission measurement -----	105
FIG. 8.2	Typical FESEM (a) top view, (b) cross section images of AlN nanotips ; (c) top view, (d) cross section images of AlN nanorods grown on p ⁺ -Si substrate -----	107
FIG. 8.3	(a) Field emission characteristic curves for quasi-aligned AlN nanotips emitter (emitting area 0.06 cm ²) grown on (▲) p ⁺ -type Si, (▽) p-type Si, (■) n ⁺ -type Si and (○) n-type Si, respectively. (★) is the AlNNRs grown on p ⁺ -type Si. Inset shows the F-N plot for field emission of the AlN nanotips grown on (▲) p ⁺ and (▽) p-type Si; (b) Emission stability of AlN nanotips grown on (▲) p ⁺ and (▽) p-type Si substrates, where the emission current was kept at a constant value of 100 μ A/cm ² -----	110
FIG. 8.4	Representative band diagram for (a) Si (n-type)-AlN and (b) Si (p-type)-AlN heterojunctions, before and after thermal equilibration. E _C , E _V , E _F stands for the conduction band, valence band and Fermi level, respectively, of AlN. E _{CN} , E _{VN} , E _{FN} stands for the conduction band, valence band and Fermi level, respectively, of n-type Si and E _{CP} , E _{VP} , E _{FP} stands for the conduction band, valence band and Fermi level, respectively, of p-type Si -----	114

List of Tables

Table 2.1	Typical phonon frequencies in hexagonal and cubic AlN obtained by Raman spectroscopy at room temperature -----	26
Table 5.1	n_1/n_2 ratio of AlN -----	75
Table 5.2	n_1/n_2 ratio of GaN -----	76
Table 5.3	n_1/n_2 ratio of InN -----	77
Table 5.4	n_1/n_2 ratio of BN -----	78

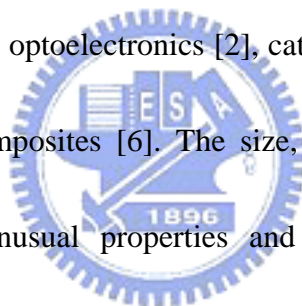


Chapter 1

Introduction

1.1 Preface

Technology in the twenty first century requires the miniaturization of devices into micrometer, even nanometer sizes while their ultimate performance is significantly improved. It raises many attentions concerning new materials for accomplishing specific demands. Nanostructured materials, a new branch of material research, represents an exciting and rapidly expanding research area due to their potential applications in electronics [1], optoelectronics [2], catalysis [3], sensors [4], magnetic data storage [5] and nanocomposites [6]. The size, surface state and inter-particle relationship dominate the unusual properties and rise up the performances of nanomaterials.



A splendid point of nanomaterials is the surface/interface to volume ratio which is crucial in applications, especially in sensing sphere. Moreover, the finite size of the nanomaterials confines the spatial distribution of the electrons, leading to the quantized energy levels due to the reduced size [7]. Therefore, investigate on nanomaterials supply a great platform for understanding effects in a nanostructured system, which could lead to major progress in developing solid state devices.

Since the discovery of carbon nanotubes [8], nanoscaled materials including

quantum dots, nanotubes, and nanowires have attracted great interest due to their exceptional properties. Nitride materials play a strategic position in materials science and engineering as one of the most versatile and far-reaching materials. A crowd of developed growth manners now have the opportunity to offer a large variety of nitride materials with tailored properties and functions. Nanostructured nitride-based materials, in particular, provide a growing number of applications which apparently depend on its nanoscale constitution. In behalf of understanding the relationship with materials performances and nanostructured materials, characterization and manipulation techniques have to be developed and fully mastered on the nanometric scale.



1.2 Nitride-based materials

The outstanding thermal and chemical stability of nitride-based materials enable them to operate at high temperatures and in hostile environment, and also make them attractive for high power/frequency operation. For optical emitters and detectors, nitride-based materials have demonstrated operation in the green, blue, or ultraviolet (UV) spectra [9]. Furthermore, for example, gallium nitride (GaN) is also chemically inert and radiation resistant and has been considered as a stable photocatalyst in photo-electrochemical fuel cell [10], while indium nitride (InN)/silicon (Si) tandem

cells have been proposed for high efficiency solar cells [11, 12].

1.3 Aluminum nitride

The properties of aluminum nitride (AlN) indicate that it has great potential for several applications. The direct band gap of 6.2 eV [13] suggests the possibility of windows which would transmit light in the UV region of the spectra and, if properly doped, optoelectronic devices which would emit light in the same spectral region, Second harmonic generators have also been proposed to make use of the high nonlinear optical susceptibilities [14]. This material also possesses very high surface acoustic wave velocity [15-16]. In addition, it is distinguished by high hardness, transparency in the visible, infrared (IR) ranges, a melting point in excess of 2275 K [17], high electrical resistivity and excellent thermal conductivity. These last two properties coupled with a static dielectric constant of ~ 9.0 have been commercially exploited in recent years in the manufacture of sintered ceramic heat sink [18]. The material is also unaffected by electromagnetic radiation, electron and ion bombardment or shock waves [19]. Consequently, it is of equal importance to just being an active component of the nitride optoelectronic devices, AlN has also attracted extensive interest for applications as electrical packaging material due to its high thermal conductivity and low coefficient of thermal expansion that closely

matches that of Si, and as components in structural composites owing to its excellent mechanical strength [20].

1.4 Nano-size requirement

Nano-system defined as having features or characteristic lengths between 1 ~ 100 nm, exhibits particularly uncommon and fascinating properties. The new generation nano-system compared to the former micro- and meso-systems represents significant superiorities list below:

(I) Miniaturization

In the world of electronics devices, “smaller” means faster response, lower cost, lower power consumption and higher performance. To achieve foregoing demands, it is thought to be efficient to use nanostructured materials instead of the micro-size ones.



(II) Amazing incredible property

Nanoscale materials exhibit great prospects in the fundamental physical and chemical sciences as well as modern nanotechnology, such as quantized excitation [1,21], Coulomb blockade [22] and metal-insulator transition [23]. For the application on field emission, nanoscale materials are expected to provide desirable improvement.

1.5 One-dimensional nano-materials

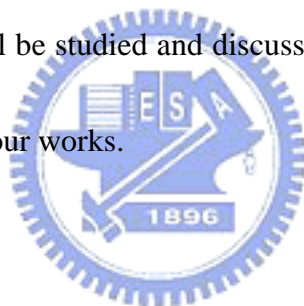
The discovery of carbon nanotubes (CNTs) [8] caused an avalanche in nano-scale research with perennial efforts to uncover new nanostructures of single elements and compounds. This saw the evolution of metallic, polymeric and more importantly semiconducting nanostructures, including CNT analogues (BC [24] and $B_xC_yN_z$ [25]), layered chalcogenides (WS_2 [26], ReS_2 [27], MoS_2 [28,29], NbS_2 , TaS_2 [30], $MoSe_2$ and WSe_2 [31]), and oxide-based compounds (ZnO [32-37], VO_x [38-43], TiO_2 [44-55], SnO_2 [56-61], GeO_2 [62,63], ZrO_2 [64], SiO_2 [65-67], Al_2O_3 [68,69], In_2O_3 [70,71], Ga_2O_3 [72-75], Y_2O_3 [76], Fe_3O_4 [77], $W_{18}O_{49}$ [78], IrO_2 [79-84], RuO_2 [85], and rare-earth oxides [86].) One-dimensional (1D) nano-scaled materials, such as nanorods (NRs), nanowires (NWs), nanobelts (NBs), and nanotips (NTs), proved to be an ideal system to study the effect of low dimensionality on their physical and chemical properties, which remain as critical functions of their dimensions and distinct morphology [87-89]. The huge surface area of these one dimensional nanostructures, that play an important role in governing their properties, is also the root cause for their degradation and instability. However the wide bandgap compound nanostructures such as SiCN nanorods [90] or BN [91-94] are comparatively stable. This fact has led researchers to apply an overcoat of stable silica [95] or boron nitride [96,97] on the otherwise nanostructures to enhance the performances. Also because

the nitride systems, most of them with direct bandgap, cover a broad emission range from IR well into UV, these scientific interests and potential applications have brought out significant efforts for the synthesis of certain 1D nanostructures of nitrides. Among them, group III-nitrides compounds, such as GaN NWs [98-103], and InN NWs [104-106] with near perfect crystal characteristic provide an opportunity to investigate the intrinsic properties that is difficult to achieve in bulk system.

1.6 Motivation

AlN has many important behaviors, especially in low dimensional nanostructured materials. However, there are only a few papers reported on either in synthesis process or characterized properties of nano-size AlN. The goal of this dissertation is to present the efforts to develop a new method of atmosphere pressure chemical vapor deposition (APCVD) to prepare 1D AlN nanomaterials. Development and modification of nanomaterials involve several key steps. First, synthesis of size and even shape controlled nanomaterials is the key for developing new materials. Second, characterization of nanostructures is indispensable to understand the behavior and properties of nanomaterials. Third, experimental results are vitally important to understand and predict the difference of material's performance. Finally, the ultimate aim is to utilize the nanomaterials for the application sphere.

The research background and the experimental section will be introduced in chapter 2 and chapter 3, respectively. Chapter 4 and chapter 5 will state the formation conditions of 1D nanostructured AlN in our APCVD experiments. The growth model of quasi-aligned AlN nanotips (AlNNTs) and AlN nanorods (AlNNRs) will be discussed. Very interesting optical properties of AlNNTs including cathodoluminescence (CL), photoluminescence (PL), thermoluminescence (TL), and ultraviolet absorption spectra will be presented in chapter 6. Chapter 7 will display the surface enhanced Raman properties by using nanostructured AlN. The field emission characteristics of AlNNTs will be studied and discussed in chapter 8. Finally, chapter 9 will conclude the results of our works.



Chapter 2

A brief review of growth and fundamental theory

2.1 Growth mechanism

2.1.1 Vapor-Liquid-Solid growth (VLS)

There are several growth techniques for nanowire-like materials. Conventional vapor-liquid-solid (VLS) growth is the most common synthetic process [107,108].

The synthesis of nanowire via the VLS process commonly relies on metal clusters

such as Au, Fe, Co, and Ni, which inevitably results in undesired contamination within the otherwise single-crystalline nanowires. VLS growth mechanism has three

stages. (a) Alloy process: a metal or oxide catalyst is deposited on the substrate, first.

With increasing nanowire elements (NE) vapor condensation and dissolution, catalyst and NE vapor form alloy and liquefy. The volume of the alloy droplets increases, and

the NE contrast decreases. A biphasic region (catalyst and catalyst/NE liquid alloy)

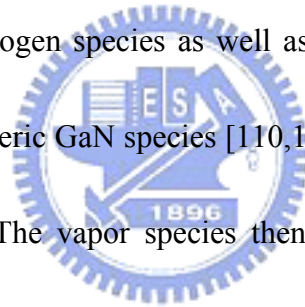
and a single phase region (liquid) coexist. (b) Nucleation: Once the composition of the alloy crosses the liquidus line, it enters a biphasic region (catalyst/NE alloy and NE).

This is where the nucleation starts. (c) Axial growth: Once the NE nucleates at the liquid/solid interface, further condensation/dissolution of NE vapor into the system

will increase the amount of NE crystal precipitation from the alloy. Then, the

nanowire is grown, and the lateral size is confined by the catalytic size. Schematic illustration of the VLS growth mechanism is shown in Fig. 2.1 [108].

A similar process of VLS growth is self-catalytic VLS growth [109]. The self-catalytic VLS growth mechanism is a reassembled process, which is different from conventional VLS process as mentioned above. The nanowires nucleate and grow from metal droplets formed during thermal deposition of compound material, like Ga droplets formed from GaN, at elevated temperatures in a vacuum. The Ga acts a self-catalytic role as well as the foreign metal or oxide catalyst. The decomposition of GaN generates atomic nitrogen species as well as small percentage of congruent evaporated diatomic or polymeric GaN species [110,111]. Liquid Ga further catalyzes the decomposition of GaN. The vapor species then re-dissolve into the Ga liquid droplets and initiate the VLS nanowire growth by supersaturating the liquid Ga and establishing a liquid-Ga/solid-GaN interface.



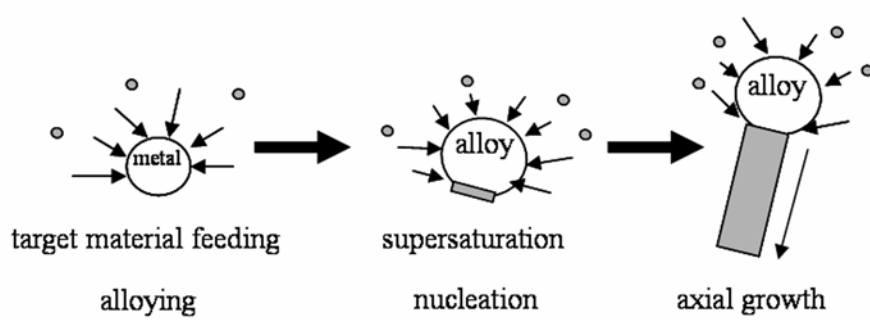
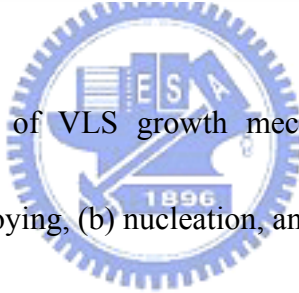
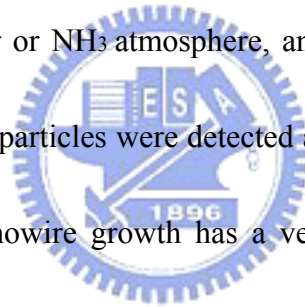


FIG. 2.1 Schematic diagram of VLS growth mechanism. The nanowire growth includes three stages of (a) alloying, (b) nucleation, and (c) axial growth [108,112].



2.1.2 Vapor-Solid growth (VS)

Vapor-solid (VS) growth is a vapor species directly transformed into solid nanowire process [72,113,114]. The VS process does not need catalyst to assist the nanowire growth. Therefore, it does not undergo a liquid-alloy stage. In VS growth, structural defect of substrate plays an important role both during the nucleation and the preferable axial growth of the nanowires. The originated elements of the nanowire can be a compound material itself or the composition of the raw materials. For example, GaN nanowire was synthesized by evaporation of GaN powders at very high temperature at 1200 °C in Ar or NH₃ atmosphere, and subsequently cooled to room temperature. No Ga-rich nanoparticles were detected at any GaN nanowire tips [114]. As mentioned-above, the nanowire growth has a very important characteristic, i.e. nanowires are grown independently from each other.



2.2 Luminescence of semiconductor

When a solid is supplied with a certain form of energy, it may emit photons besides thermal radiation. This process is called luminescence. There are several types of luminescence, which dependent on the excitation source. For example, photoluminescence (excitation by photo), cathodoluminescence (excitation by energetic electron or cathode rays), electroluminescence (excitation by application of

an electric field), chemiluminescence (energy supplied by chemical reaction), and so on [115]. The emission of photon in luminescence processes is due to transition of an electron from an initial state E_i to a final state E_f . The emitted photon energy, or wavelength, has a relation of

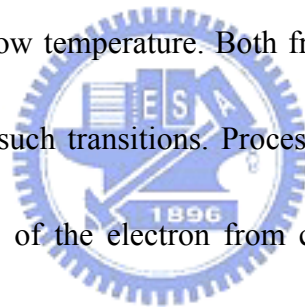
$$h\nu = hc/\lambda = \Delta E = E_i - E_f$$

where h is the Plank constant, ν is the photon frequency, c is the light speed in vacuum, λ is the photon wavelength, and ΔE is the energy difference between initial and final state.

Luminescence emission spectra can be divided into intrinsic (fundamental, edge) emission and extrinsic (activated, characteristic) emission. Intrinsic luminescence is due to recombination process of electrons and holes across the fundamental energy gap E_g , so it is an intrinsic property of the material. The emission spectra, which depend on the presence of impurity atoms or other defects, are extrinsic in nature. Energy and crystal momentum must be conserved during the electronic transitions. Energy band gaps of semiconductors can be separated into direct- and indirect gaps. When valence band maximum and conduction band minimum occur at the same value of wave vector \mathbf{k} (see Fig. 2.2(a) [112]), the material is a direct-gap semiconductor. If the band extreme do not occur at the same wave vector \mathbf{k} (see Fig. 2.2(b) [112]), the bandgap is indirect. Since the momentum of a photon is negligibly small and direct

bandgap is required for the emission of photon in order to meet total momentum conservation.

In the optical transition process [116], a simplified set of transitions in semiconductor is shown in Fig. 2.3. Process (a) is an interband transition; this produces intrinsic luminescence. Although this recombination occurs from states close to corresponding band edges, the thermal distribution of carriers in these states will lead to broad emission spectra. Process (b) is a higher-energy emission involving energetic or hot carriers, sometimes related to avalanche emission. Process (c) is the exciton decay observable at low temperature. Both free-excitons and excitons bound to an impurity may undergo such transitions. Process (d) is a deep transition. Deep transitions involve transitions of the electron from conduction band to an acceptor level or transition from donor level to valence band. Process (e) is a donor-acceptor pair recombination. Process (f) is called a shallow transition. This transition is from the acceptor level to valence band or from the conduction band to donor level. Process (g) is an intraband transition involving hot carriers, sometimes called deceleration emission. As mentioned above, the transition involves radiative and non-radiative recombination. Not all transition can occur in the same material or under the same condition. An efficient luminescence material is one in which radiative transitions predominate over nonradiative ones. Figure 2.4 shows the energy gap versus the



lattice constant for several compound semiconductors [117]. For AlN, both wurtzite and zincblende structures are direct bandgap semiconductors, and the band gaps are about 6.2 eV and 5.0 eV, respectively [118].

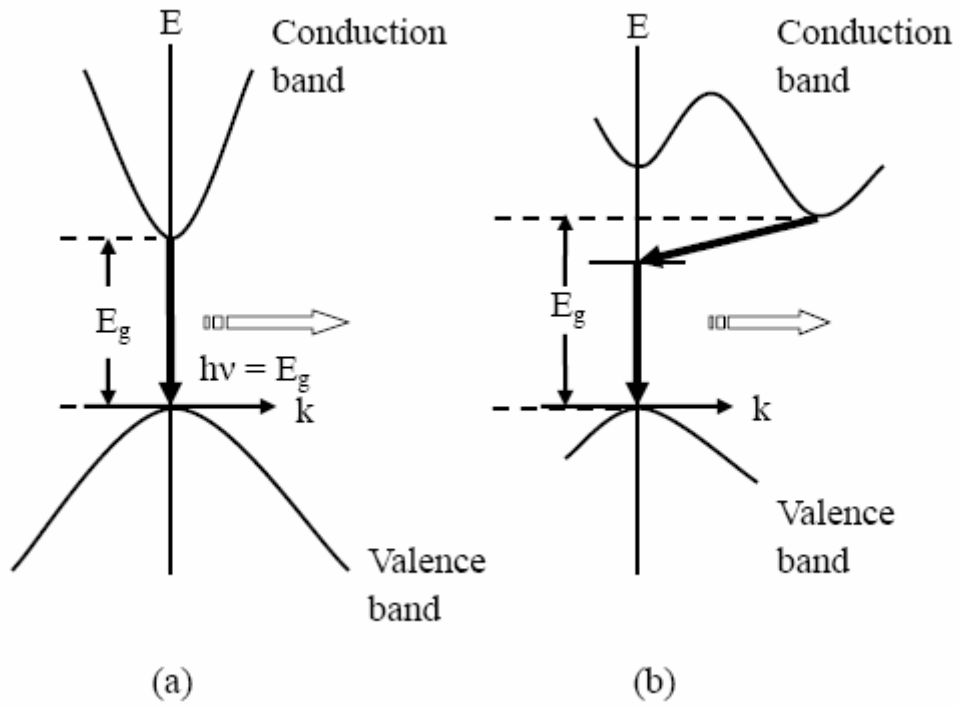


FIG. 2.2 Energy diagram of (a) direct- and (b) indirect-gap semiconductors. [112,116]

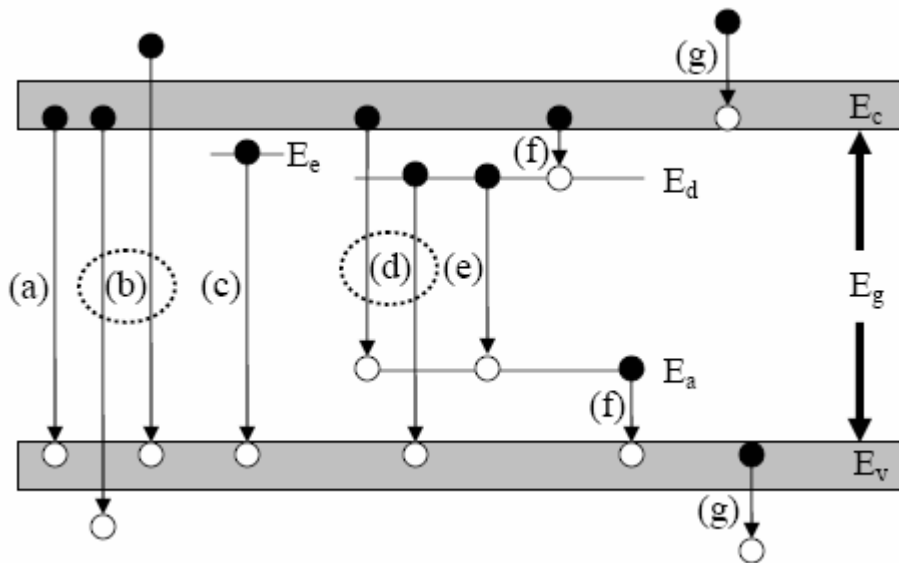


FIG. 2.3 Schematic diagram of transitions in a semiconductor. E_c is the conduction band, E_v the valence band, E_e the exciton level, E_d the donor level, and E_a the acceptor level. [112,116]

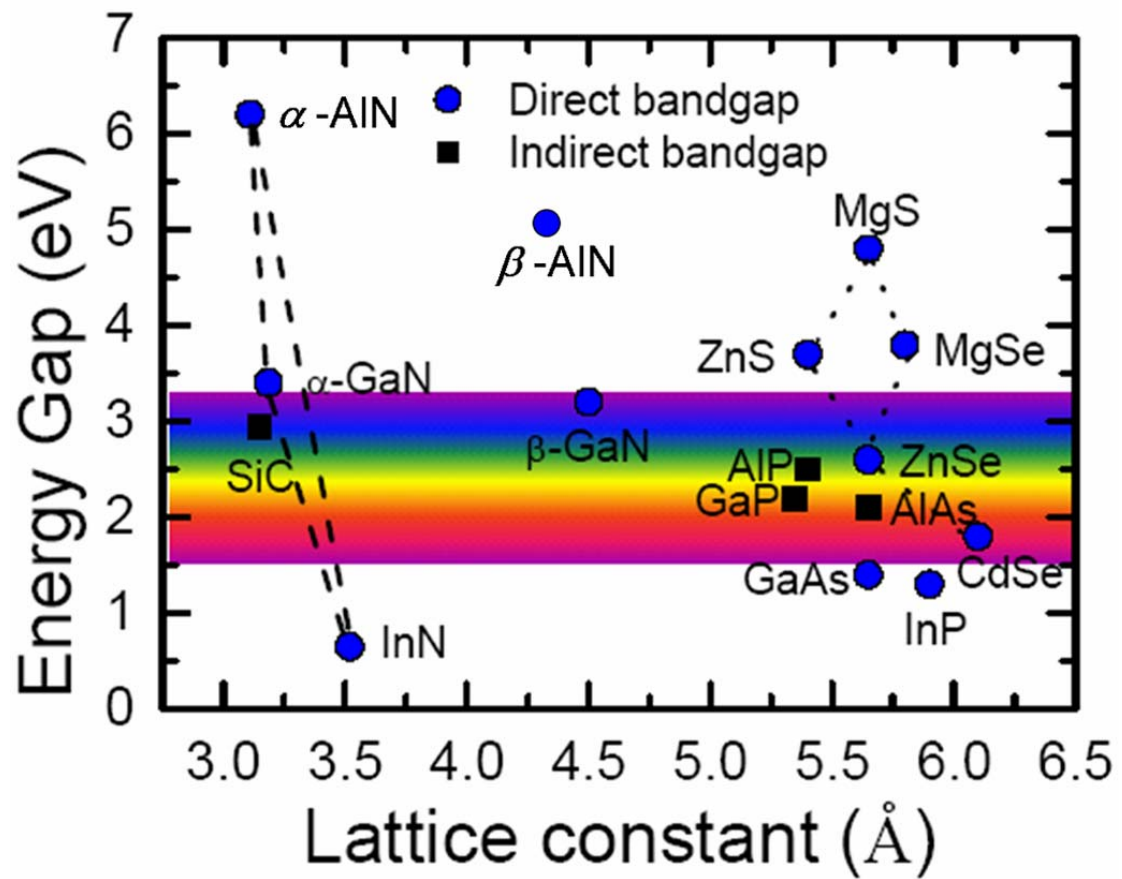


FIG. 2.4 Energy gap of different compound semiconductors as a function of lattice constant. [112,117]

2.3 Raman spectroscopy

Vibrational transition can be observed in IR (infrared) or Raman spectra. Figure 2.5 shows differences in mechanism of Raman and IR. According to quantum mechanics [119], a vibration is IR-active if the dipole moment is changed during the vibration, and is Raman-active if the polarizability is changed during the vibration. In IR spectroscopy, a molecule absorbs energy $\nu = \Delta hE$ from IR source at vibrational transition. The intensity of absorption is governed by Beer-Lambert law:

$$I = I_0 e^{-\alpha d} \quad (2.3.1)$$

where I and I_0 are the intensities of incident and transmitted light, respectively. α is the molecular absorption coefficient [120], and d is the sample thickness. The percentage of transmittance $T(\%)$ is given as

$$T(\%) = \frac{I}{I_0} \times 100 \quad (2.3.2)$$

The absorbance (A) is defined as

$$A = \log \frac{I_0}{I} = \alpha d \quad (2.3.3)$$

The IR spectroscopy often plots percentage transmittance $T(\%)$ or absorbance A with respect to the wavenumber to obtain the molecular vibrational modes.

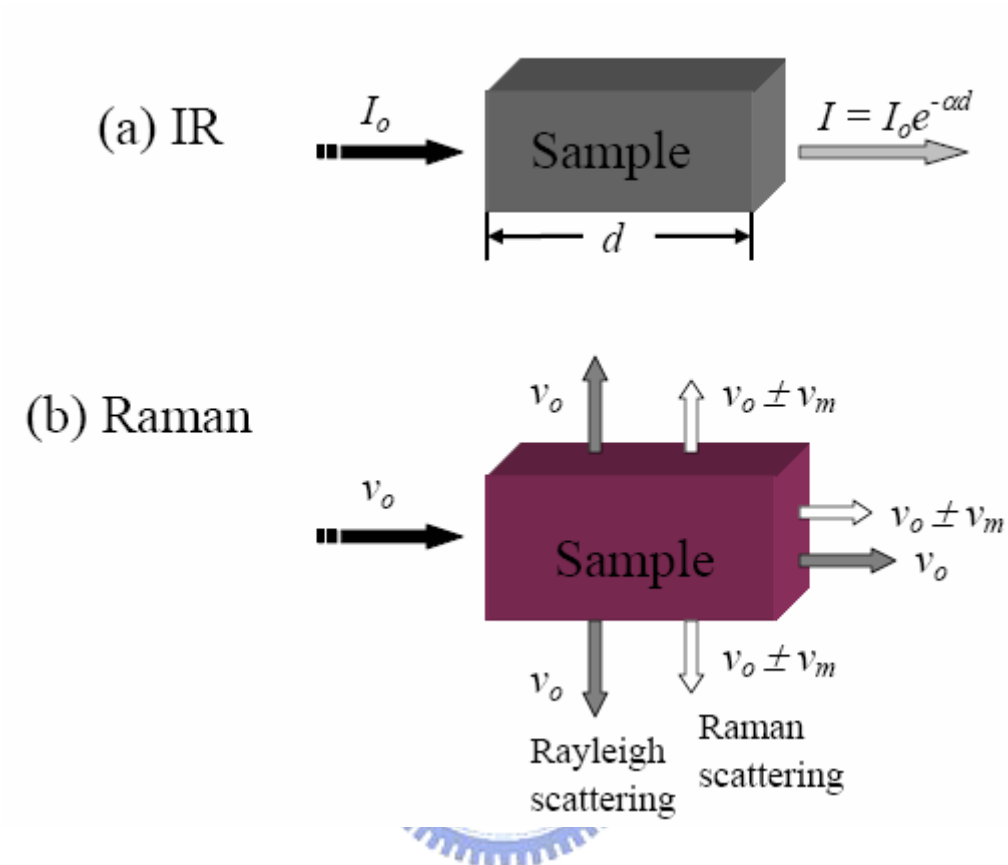


FIG. 2.5 Mechanism of (a) IR, and (b) Raman spectroscopy. [112,119]

In Raman spectroscopy, an intensive laser with linear polarization is often used as the excitation source. According to the classical theory, Raman scattering can be explained in the following. The oscillating electric field strength (E) of an electromagnetic wave is given by

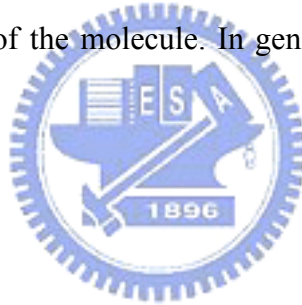
$$E = E_0 \cos 2\pi\nu_0 t \quad (2.3.4)$$

where E_0 is the amplitude of electric field and ν_0 is frequency of incident laser. If a diatomic molecule is irradiated by the laser, an electric dipole moment P is induced:

$$P = \alpha E = \alpha E_0 \cos 2\pi\nu_0 t \quad (2.3.5)$$

where α is the polarizability of the molecule. In general, α is a 3 x 3 matrix. In the Cartesian coordinates,

$$\begin{bmatrix} P_x \\ P_y \\ P_z \end{bmatrix} = \begin{bmatrix} \alpha_{xx} & \alpha_{xy} & \alpha_{xz} \\ \alpha_{yx} & \alpha_{yy} & \alpha_{yz} \\ \alpha_{zx} & \alpha_{zy} & \alpha_{zz} \end{bmatrix} \begin{bmatrix} E_x \\ E_y \\ E_z \end{bmatrix} \quad (2.3.6)$$



The matrix, α , is called the polarizability tensor. In normal Raman scattering, $\alpha_{xy} = \alpha_{yx}$, $\alpha_{xz} = \alpha_{zx}$, and $\alpha_{yz} = \alpha_{zy}$. The vibration is Raman-active if one of these components of the polarizability tensor is changed during the vibration. If the vibrational frequency of the molecule is ν_m , the nuclear displacement q is given by

$$q = q_0 \cos 2\pi\nu_m t \quad (2.3.7)$$

where q_0 is the vibrational amplitude. For a small vibration, α can be expanded in terms of q as

$$\alpha = \alpha_0 + \left(\frac{\partial \alpha}{\partial q} \right)_0 q + \dots \quad (2.3.8)$$

Here, α_0 is the polarizability at equilibrium position $\left(\frac{\partial \alpha}{\partial q} \right)_0$ is the rate of change of α

with respect to the change in q evaluated at the equilibrium position. Substituting Eqs.

2.3.4, 2.3.7 and 2.3.8 into Eq. 2.3.5, Eq. 2.3.5 becomes

$$\begin{aligned} P &= \alpha E_0 \cos 2\pi\nu_0 t \\ &= \alpha_0 E_0 \cos 2\pi\nu_0 t + \left(\frac{\partial \alpha}{\partial q} \right)_0 q_0 E_0 \cos 2\pi\nu_0 t \cos 2\pi\nu_m t + \dots \\ &= \alpha_0 E_0 \cos 2\pi\nu_0 t + \frac{1}{2} \left(\frac{\partial \alpha}{\partial q} \right)_0 q_0 E_0 [\cos\{2\pi(\nu_0 - \nu_m)t\} + \cos\{2\pi(\nu_0 + \nu_m)t\}] + \dots \end{aligned} \quad (2.3.9)$$

The first term in Eq. 2.3.9 represents an oscillating dipole that radiates light of frequency ν_0 , which is called Rayleigh scattering. The $\nu_0 - \nu_m$ and $\nu_0 + \nu_m$ in the second term are called Stokes and anti-Stokes Raman lines, respectively. It should be

noticed that if $\left(\frac{\partial \alpha}{\partial q} \right)_0$ is zero, the vibration is not Raman-active. In other words, to be

Raman-active, the rate of change of polarizability with the vibration must not be zero.

A simple diagram vibrational transitions is illustrated in Fig. 2.6 [121]. In IR spectroscopy, only transition of $\nu = 0$ (vibrational ground state) $\rightarrow 1$ (vibrational first excited state) at the electronic ground state can be observed. For normal Raman spectroscopy, an exciting laser energy ν_0 is chosen so that its energy is far below the first excited state. The virtual states are plotted as dotted lines to distinguish the real excited state. According to the Maxwell-Boltzmann distribution law, the population

ratio of the $\nu = 1(P_{\nu=1})$ and $\nu = 0(P_{\nu=0})$ states is given by

$$\frac{P_{\nu=1}}{P_{\nu=0}} = e^{\frac{-\Delta E}{kT}} \quad (2.3.10)$$

where ΔE is the energy difference between two states, T is the absolute temperature, and k is Boltzmann's constant (1.38×10^{-23} Joule/degree). In general, the population of molecules at $\nu = 0$ is much larger than that $\nu = 1$. Thus, the Stokes lines (S) are stronger than the anti-Stokes (A) lines under normal condition. Resonance Raman (RR) scattering occurs when the exciting line is chosen so that its energy intercepts the manifold of an electronic excited state. Finally, the fluorescence spectra are observed when the excited state decays to the lowest vibrational state via radiationless transitions and then emits radiation.

AlN normally has a wurtzite structure with the space group of $P6_3mc(C_{6v}^4)$. The wurtzite structure consists of alternating biatomic close-packed (0001) planes of Al and N pairs stacked in an *ABABAB* sequence. Figure 2.7 shows the views of wurtzite AlN along $[0001]$, $[11\bar{2}0]$, and $[10\bar{1}0]$ directions [122]. The zincblende structure of AlN belongs to space group of $F\bar{4}3m(T_d^2)$. The stacking sequence for the (111) close-packed planes in this structure is *ABCABC*. Views of the zincblende structure are shown in Fig. 2.8 [122].

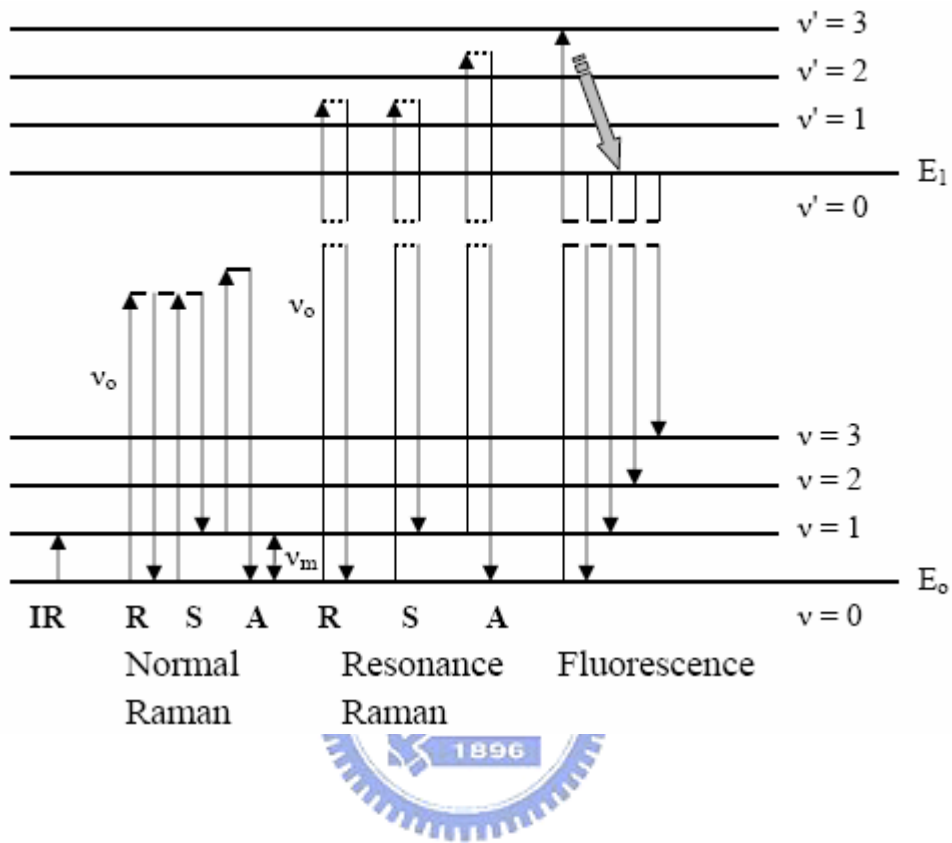


FIG. 2.6 Energy levels of IR, normal Raman, resonance Raman, and fluorescence spectra. R: Rayleigh scattering, S: Stokes Raman scattering, A: anti-Stokes Raman scattering. [112,121]

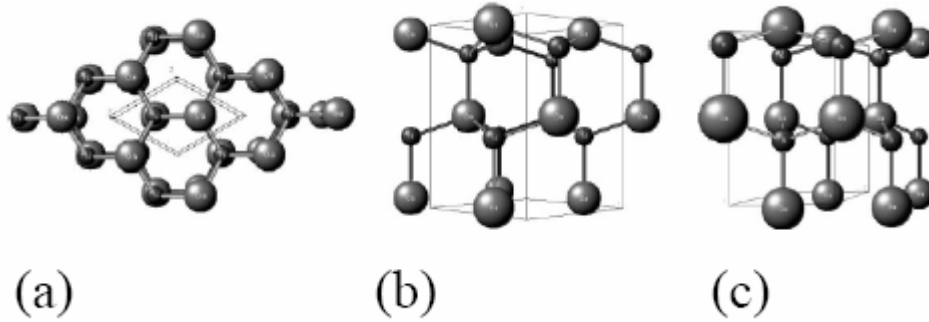


FIG. 2.7 Crystal structure views of wurtzite along different directions: (a) $[0001]$, (b) $[1\bar{1}20]$, and (c) $[10\bar{1}0]$. [112,122]

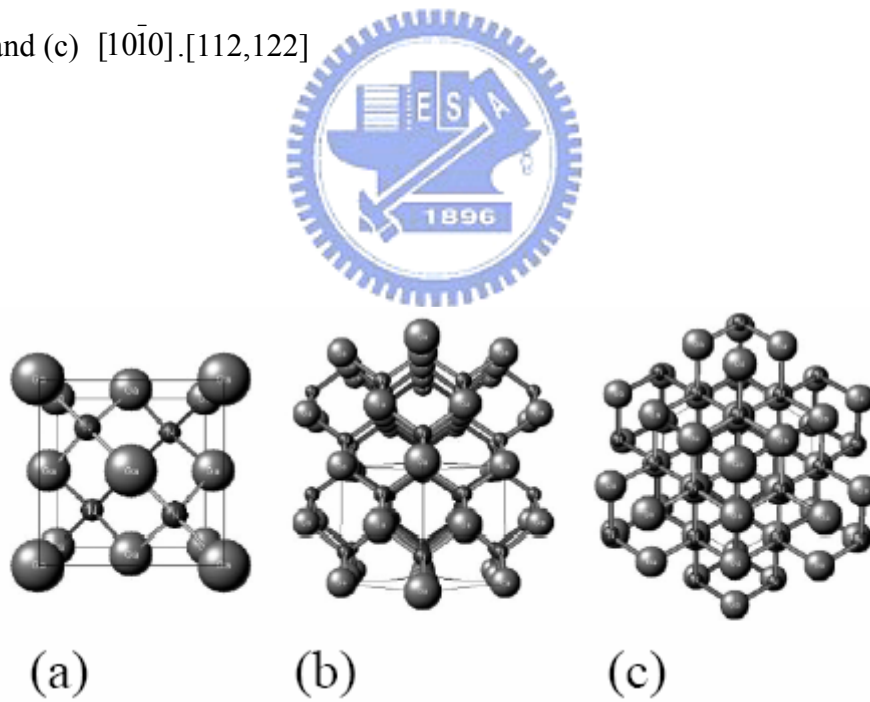


FIG. 2.8 Crystal structure views of zincblende along different directions: (a) $[100]$, (b) $[110]$, and (c) $[111]$. [112,122]

The first-order Raman scattering is caused by the phonon with a wavevector near Γ point ($k = 0$), because the light scattering process must follow the momentum conservation rule. According to the group theory selection rule, zincblende-type materials have a doubly degenerate TO and a single LO phonon modes close to $k = 0$. The wurtzite-type crystal structure has eight sets of phonon modes at the Γ point namely $2A_1 + 2E_1 + 2E_2 + 2B_1$. A_1 and E_1 modes are acoustic phonon modes. The remained six modes of $A_1 + E_1 + 2E_2 + 2B_1$ are optical phonon modes. Figure 2.9 shows an atomic displacement scheme of these optical phonon modes. Atomic displacements in A_1 and B_1 modes are along the c -axis, while the atomic displacements in E_1 and E_2 modes are give perpendicular to the c -axis. The A_1 and E_1 modes are both Raman and IR active, while the two E_2 modes are only Raman-active, and the two B_1 modes are silent modes of Raman and IR [123-125]. Typical wurtzite- and zincblende-AlN phonon modes are summarized in Table 2.1 [126-128].

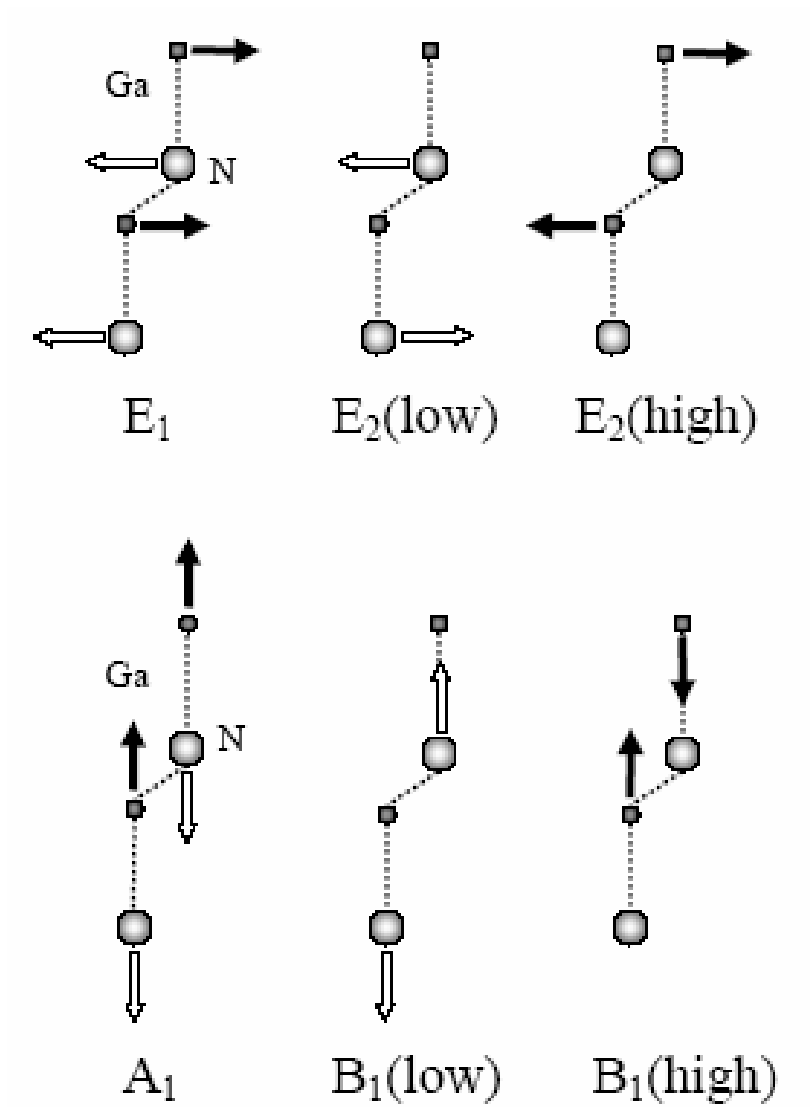
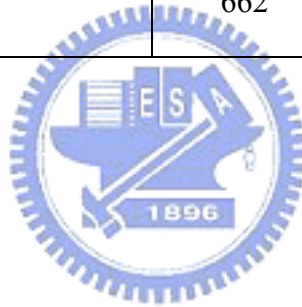


FIG. 2.9 Optical phonon modes in wurtzite structure. [112]

Table 2.1 Typical phonon frequencies in hexagonal and cubic AlN obtained by Raman spectroscopy at room temperature.

Hexagonal	A₁(TO)	E₂(high)	E₁(TO)	A₁(LO)	E₁(LO)
126	607.3	653.6	666.5	884.5	912
127	610	656	669	890	911
128	619		677	893	918
Cubic			TO		LO
128			662		907



2.4 Field Emission

2.4.1 Field Emission from metal

Field emission is a quantum-mechanical phenomenon in which electrons tunnel through a potential barrier at the surface of a solid as a result of the application of a large electric field. Field emission is distinct from thermionic emission and photoemission in which electrons acquire sufficient energy via heating or energy exchange with photons, respectively, to overcome the potential barrier. In field emission external electric fields on the order of $10^7 \text{ V}\cdot\text{cm}^{-1}$ are required for appreciable electron currents. The presence of the electric field makes the width of the potential barrier being finite, and therefore permeable to the electrons. This can be seen with the Fig. 2.10 [129], which presents a diagram of the electron potential energy at the surface of a metal. The dashed line in Fig. 2.10 shows the shape of the barrier in the absence of an external electric field. The height of the barrier is equal to the work function of the metal, ϕ , which is defined as the energy required to remove an electron from the Fermi level E_F of the metal to a rest position just outside the material (the vacuum level). The solid line in Fig. 2.10 corresponds to the shape of the barrier in the presence of the external electric field. As can be seen, in addition to the barrier becoming triangular in shape, the height of the barrier in the presence of the electric field E is smaller, with the lowering given by Eq.(2.4.1) [130].

$$\Delta \phi = \left(\frac{eE}{4\pi\epsilon_0} \right)^{1/2} \quad (2.4.1)$$

where e is the elementary charge and ϵ_0 is the permittivity of vacuum.

Knowing the shape of the energy barrier, one can calculate the probability of an electron with a given energy tunneling through the barrier. Integrating the probability function multiplied by an electron supply function in the available range of electron energies leads to an expression for the tunneling current density J as a function of the external electric field E . The tunneling current density can be expressed by Eq. (2.4.2)

which is often referred to as the Fowler-Nordheim equation [131]

$$J = \frac{e^3 E^2}{8\pi h \phi t^2(y)} \exp \left[\frac{-8\pi(2m)^{1/2} \phi^{3/2}}{3h e E} v(y) \right] \quad (2.4.2)$$

where $y = \Delta\phi/\phi$ with $\Delta\phi$ given by Eq. (1), h is the Planck's constant, m is the electron mass, and $t(y)$ and $v(y)$ are the Nordheim elliptic functions; to the first approximation $t^2(y) = 1.1$ and $v(y) = 0.95 - y^2$. Substituting these approximations in Eq. (2.4.2), together with Eq. (2.4.1) for y and values for the fundamental constants, one obtains

Eq. (2.4.3) [131].

$$J = 1.42 \times 10^{-6} \frac{E^2}{\phi} \exp \left(\frac{10.4}{\phi^{1/2}} \right) \exp \left(\frac{-6.44 \times 10^7 \phi^{3/2}}{E} \right) \quad (2.4.3)$$

where J is in units of $A \text{ cm}^{-2}$, E is in units of $V \text{ cm}^{-1}$ and ϕ in units of eV. Plotting $\log(J/E^2)$ vs. $1/E$ results in a straight line with the slope proportional to the work function value, ϕ , to the 3/2 power. Eq. (2.4.3) applies strictly to temperature equal to 0 K.

However, it can be shown that the error involved in the use of the equation for moderate temperatures (~ 300 K) is negligible.

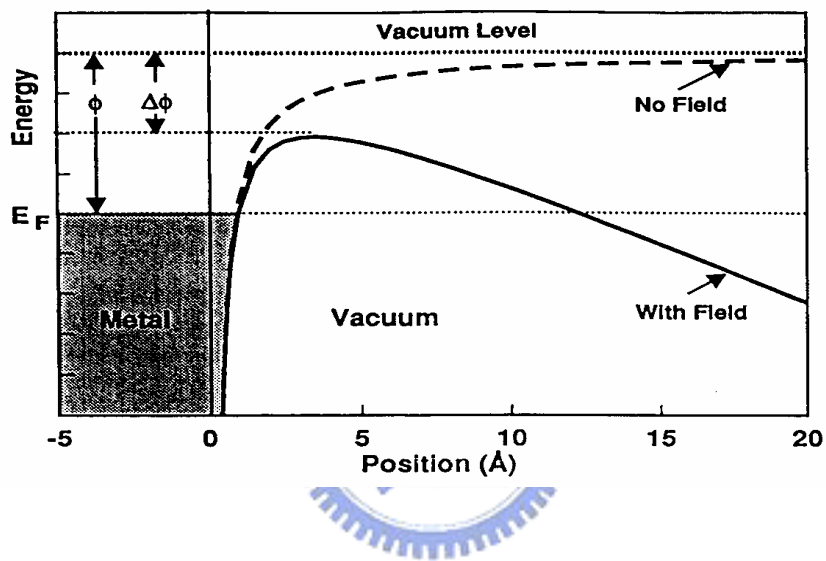


Fig. 2.10 Diagram of potential energy of electrons at the surface of metal. [129]

2.4.2 Field Emission from Semiconductor

To a large degree, the theory for electron emission from semiconductors can be derived parallel to the theory for metals. However, special effects are associated with semiconductors due to the state of their surface and the fact that an external field applied to a semiconductor may penetrate to a significant distance into the interior. The classic theoretical treatment of electron emission from semiconductors is given in. For the case when the external electric field penetrates into the interior of an n-type semiconductor and the surface states are neglected, $\log(J/E^2)$ is shown to be a linear function of $1/E$, as for metals. However, in place of the work function ϕ in the Fowler-Nordheim equation one needs to substitute a quantity $\chi - \delta$, where χ is the electron affinity defined as the energy required for removing an electron from the bottom of the conduction band of the semiconductor to a rest position in the vacuum, and δ denotes the band bending below the Fermi level. These parameters are illustrated in Fig. 2.11 [129].

The linear dependence of $\log (J/E^2)$ on $1/E$ is expected only if the density of the current flowing through the sample is much smaller than the current limiting density $J_{lim} = en\mu_n E/\varepsilon$, where μ_n is the electron mobility and n is the electron concentration in the bulk of the semiconductor [132,133]. At $J \approx J_{lim}$ the Fowler-Nordheim character of the relationship $J(E)$ passes into the Ohm's law (if the dependence of electron mobility

on the electric field is neglected) which results in the appearance of the saturation region in the emission current vs. voltage curve. Such saturation regions were observed experimentally for lightly doped n-type semiconductors and for p-type semiconductors [134,135].

Electron emission from semiconductors has been a subject of more recent theoretical considerations, which takes into account complications due to electron scattering, surface state density, temperature, and tip curvature [136,137].

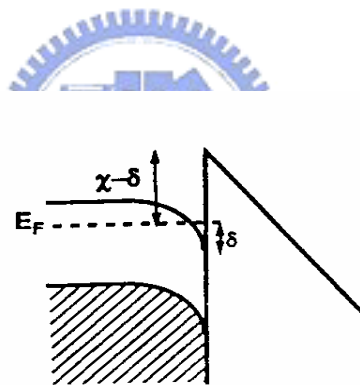


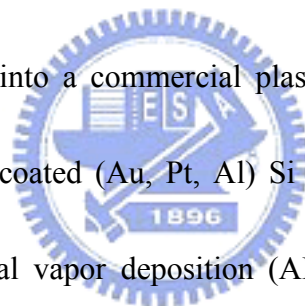
Fig. 2.11 Diagram of potential energy of electrons at the surface of an n-type semiconductor with field penetration into semiconductor interior. [129]

Chapter 3

Experimental method

3.1. Experimental Details

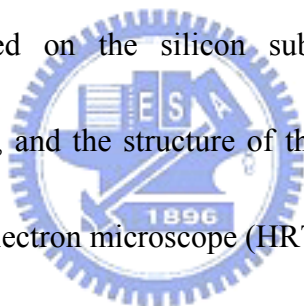
Starting substrates were mirror-polish, (100) oriented wafer, differently doped, including p⁺-type (boron doping, resistivity ~ 2-5 mΩ cm), p-type (boron doping, resistivity ~ 10 Ω cm), n-type (phosphor doping, resistivity ~ 10 Ω cm), and n⁺-type (phosphor doping, resistivity ~ 2-5 mΩ cm) silicon substrates. After the pre-treatment of substrates, they were put into a commercial plasma metal coater to deposit the metal layer. Then, the metal-coated (Au, Pt, Al) Si substrates were placed into the atmospheric pressure chemical vapor deposition (APCVD) system to prepare AlN nanomaterials with various deposition parameters. Finally, several apparatuses were used to analyze the characterization of these nanomaterials.



3.2. Atmospheric pressure chemical vapor deposition

Figure 3.1 schematically depicts the layout of the APCVD system [99,106,138]. The AlNNTs were grown by vapor transport and condensation process using silicon substrates covered with gold, platinum or aluminum that act as catalysts. An aluminum oxide boat, carrying the metal coated silicon substrate and pure aluminum

powders (SHOWA, Japan), was placed inside a quartz tube (1 inch in diameter). The Al powders were kept up stream and the Au-coated Si substrate was placed upside down (Au-coated side facing the Al powders) and downstream with respect to the flow of the nitriding gas, in this case NH_3 . The quartz tube was housed in a conventional tube furnace. The quartz tube was degassed and then purged with ammonia NH_3 (30 sccm) as the atomic nitrogen precursors. During the growth process, the furnace was ramped up to 950, 1000, 1100, and 1200°C, respectively, and held at that temperature for 30 mins with an ammonia flow rate of 30 sccm. After cooling down, the products collected on the silicon substrate were characterized by high-resolution SEM analysis, and the structure of the nanotips was studied using a high resolution transmission electron microscope (HRTEM), XRD and Micro-Raman.



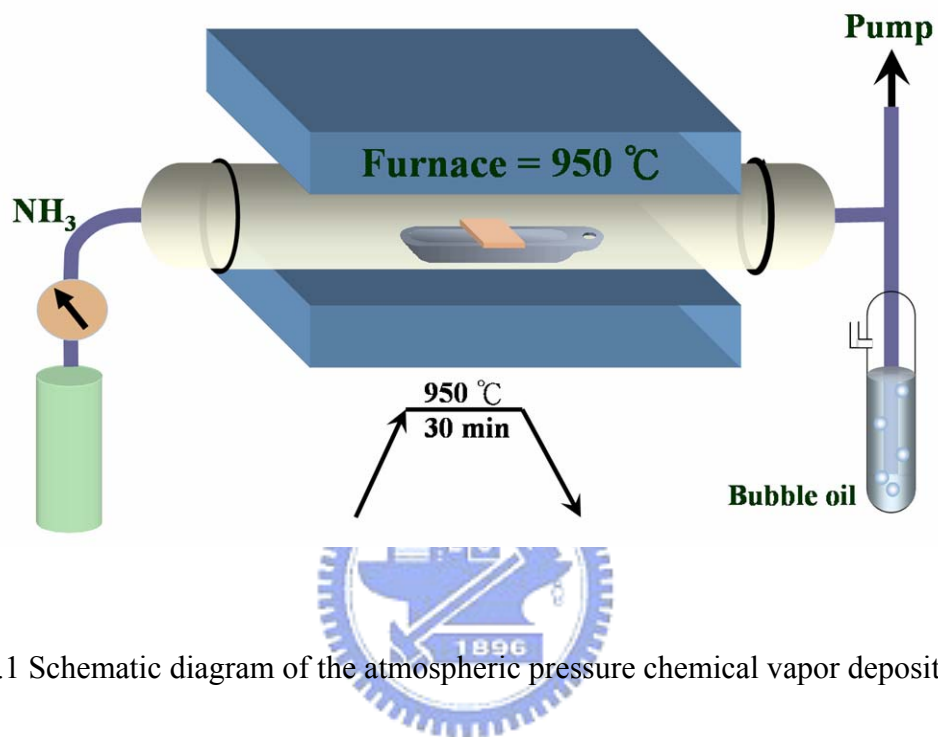


FIG. 3.1 Schematic diagram of the atmospheric pressure chemical vapor deposition

3.3 Characterization of AlN nanomaterials

3.3.1. Scanning electron microscopy (SEM)

The scanning electron microscopy (SEM) was used the secondary electron mode to observe the morphology of AlN nanomaterials. The model of the SEM used here is JEOL JSM6700F.

3.3.2. Transmission electron microscopy (TEM)

One of the typical characters of nano-phase materials is the small object size. Although some structural features can be revealed by x-ray and neutron diffraction, direct imaging of nanomaterials is only possible using high resolution transmission electron microscopy (HRTEM, Philips TECNAI 20). TEM is a unique technique because it can produce a real space image on the atom distribution in the nanocrystal surface. With a finely focused electron probe, the structural characteristic of a single nanomaterial can be fully understood. Normally, the chemical analysis system, the energy disperse X-ray spectrometer (EDX), was attached on TEM system.

3.3.3. Electron energy loss spectroscopy (EELS)

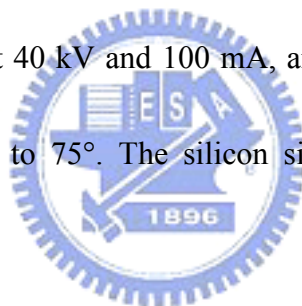
EELS is a nano-analytical technique that uses the characteristic spectrum of energy losses of transmitted electrons to obtain information about elemental composition, chemical bonding, and electronic structure [139,140]. An EELS spectrum consists of a monotonically-decreasing background on which several broad

peaks, each characteristic of a particular inelastic scattering process, are superimposed.

The spatial resolution is limited by the diameter of the incident illumination focused on the sample. The energy loss spectrum displays the intensity distribution of the imaging electrons as a function of the energy loss. It supplies qualitative and quantitative information about the atomic and molecular structure of this specimen.

3.3.4. X-ray diffraction spectroscopy

X-ray diffraction analysis of the AlN nanomaterials specimens was carried out by using a Rigaku D/max diffractometer using $\theta/2\theta$ mode. The X-ray was generated by a Cu target (Cu $K\alpha$) operated at 40 kV and 100 mA, and the scanning speed was 0.02 deg/step, 1deg/min from 20° to 75°. The silicon signal was used to calibrate the diffraction patterns.



3.3.5. Micro-Raman spectroscopy

Raman spectroscopy is an excellent technique for characterization of the crystalline quality either in films or nanostructures. The various products were qualitatively analyzed by laser micro-Raman spectroscopy (Renishaw Raman Microscope, Model 2000). In the Raman experiment, an Nd-YAG laser excitation with the wavelength of 532.2 nm was used as an exciting light source. The laser light with the power of 500 mW was reflected by a half-mirror, and focused on to the sample with an objective lens. The operational region can be conducted from 150~8000 cm^{-1} with the

resolution of $1\sim 5\text{ cm}^{-1}$.

3.3.6. Cathodoluminescence (CL)

Cathodoluminescence is the light emission associated with the excitation of materials by an electron beam. The optics of a scanning electron microscope can be utilized to produce a focused beam and to excite a small region of the sample. The beam diameter in the SEM is of the order of a few nanometers. The excited volume depends on the energy of the electron beam. Electron energies ranging from 0.1 keV to 20 keV are commonly used in the SEM. The resulting probe volumes range from tens of nanometers to a few microns in radius. The light emitted from such region is captured by a parabolic mirror, and a spectrum is obtained using a grating and a high efficiency light detector. By changing the energy of the electron beam it is possible to perform a depth profile of the optical properties of the specimen. By scanning in the form of a raster, it is possible to produce images of the light emitting intensities for specific wavelengths. The resolution of the technique depends on the diffusion length of the excited carriers. It can be as small as the electron probe in the case of very small diffusion lengths. Temperature-dependent CL study was performed using a Gatan MonoCL3 system with an accelerating voltage of 15 kV, current density of electron beam of 20 mA attached to a JEOL JSM-6700F field emission scanning electron microscope. The photomultiplier is biased at -1500 volt. The scanning rate

was kept at 1 nm/ step with each step dwell for one second.

3.3.7. Photoluminescence (PL)

The photoluminescence and photoluminescence excitation properties of AlN nanomaterials were measured by a Tau-3 lifetime system. The light source is a Xe lamp with power of 450 W. The excitation area is ranging from 2.06 to 5.65 eV, and emission area is ranging 1.46 to 4.13 eV with a high resolution of 0.4 meV. The tau-3 lifetime system has two mode of operation: one is steady-state mode, the other is lifetime (kinetic) mode. The life-time range can be conducted from 10 pico-second to 10 micro-seconds.

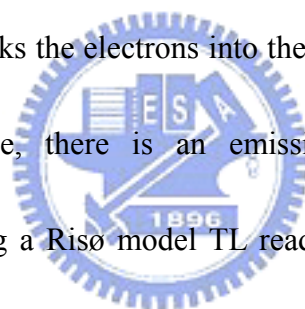
3.3.8. Thermoluminescence (TL)

Thermoluminescence (TL) is the process in which a material emits light while it is being heated [141-143]. The light emitted is due to the recombination of charges trapped at metastable defect sites within the material lattice, and its amount is proportional to energy absorbed by the mineral as a result of its previous exposure to ionizing radiation. However, TL is totally different from the incandescence, which is emitting light due to high temperature of the solid.

Normally, charges trapped in deep traps in a material's lattice will remain there indefinitely if the material rests at the ambient temperature. However, heating a material to such a specific temperature immediately evicts trapped electrons from the

deep traps. They promptly undergo recombination, and in doing so emit photons in the visible spectrum. The amount of light emitted is proportional to the material's intrinsic sensitivity to radiation and the total amount of radiation energy absorbed. Comparisons made of the light emitted by a natural sample and the amount of light emitted by a sample with a known added radiation dose, plus separate dosimetry measurements, allow the sample's age since it was last exposed to a clock-resetting event to be calculated.

First, samples were irradiated by UV light through an UV lamp with interference filters. The UV irradiation locks the electrons into the defects. When the electrons are induced to leave the lattice, there is an emission of luminescent light. TL measurement was made using a Risø model TL reader with linear planchet heating and equipped with a built-in $^{90}\text{Y}/^{90}\text{Sr}$ software-controlled beta source.



3.3.9. UV absorption

UV absorption was done in Model U-3010 (Hitachi, Japan) spectrophotometer covers the UV/Visible range from 190-900 nm by employing both a tungsten-iodide (WI) lamp for the visible region and a deuterium (D2) lamp for the ultraviolet region.

3.3.10. Measurement of field emission characterization

The turn-on field for $10 \mu\text{A}/\text{cm}^2$ has been used as the merit parameters to distinguish various emitter materials [144-146]. Field emission properties were

measured by using diode-type structure. An anode plate (ITO Glass) was placed at 70 μ m above the AlN nanomaterials emitters, which served as the cathode electrode. The field emission (FE) measurement was carried out in a vacuum chamber at a pressure of $\sim 10^{-7}$ torr at room temperature. The applied voltage was biased from 0 to 1100 V and current which was collected from the emitters was recorded by using a Keithley 237 system.



Chapter 4

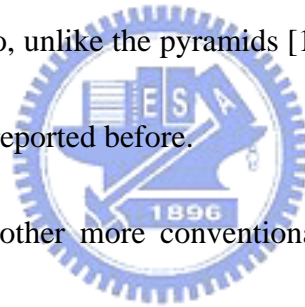
Growth of AlN nanotips by means of APCVD

In this chapter, preparations of AlN nanotips (AlNNTs) on the Si (100) substrates by APCVD method will be presented. The effects of the thickness of catalyst, type of catalysts, and preparation time on the formation of single-crystalline AlN in the CVD experiments are studied. The surface morphology, structure, and composition properties of the as-deposited samples are characterized in detail. The overall structural and morphological results are discussed in section 4.2 via FESEM Raman scattering and XRD measurements, respectively. The growth mechanism of AlNNTs formation was described in section 4.3. Finally, section 4.4 will make a summary according to the obtained results.

4.1. AlN nanotips growth

AlN nanowires, whiskers and nanotubes have been obtained by chloride assisted growth [115,116], arc process [117], carbothermal reduction [118,119], and gas-reduction-nitridation [120]. However, very recently, there has been an increased activity in this field with quite a few reports on nanowires, nanotubes and nanobelts decorating the 1D AlN domain. Vapour-liquid-solid (VLS) growth of hexagonal AlN

nanowires and nanotubes with [001] growth direction have been reported at temperatures above 1100°C [121,122]. Hexagonal AlN nanobelts with rectangular cross-section and having [001] growth direction also made their appearance [123]. Vapor-solid (VS) growth is a vapor species directly transformed into solid nanowire process [124]. The VS process does not need catalyst to assist the nanowire growth. Therefore, it does not undergo a liquid-alloy stage. A cubic AlN nanotube with a boron nitride (BN) wrapping (AlN-BN composite nanotube) has been made possible at a temperature of 1200°C using a two stage growth mechanism [125]. However, AlN nanotips with high aspect ratio, unlike the pyramids [126], also form a special class in the 1D family, have not been reported before.



Nanotips in Si-based and other more conventional semiconductor systems have been demonstrated and explored for various potential applications as field-emitters [146-148], solar cells [149], bio/chemical sensing devices [150-152], and optical nanodevices [36,153]. Until now, optical lithography has been playing the major role in fabricating sharp tips but limited to 50 nm in radius [154-156]. A novel electron-cyclotron-resonance plasma assisted dry-etching technique has recently been developed for producing ultra-fine tips (~ 1 nm) in a wide range of material systems, excluding AlN [157]. These tips (Si, poly-Si, GaN, GaP, Al) can have apex diameters from 2-20 nm, and growth directions depending upon the orientation of the starting

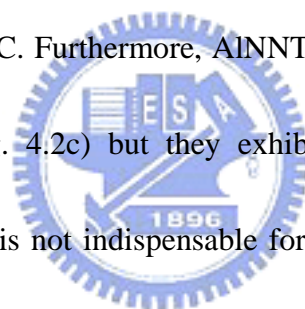
wafers. The approaches captioned above can be classified as top-down techniques and are most suitable for plate or wafer process. In this study, we report on the first synthesis of single-crystalline AlNNTs with a monodispersed angle distribution via simple vapor transport and condensation process (VTCP), in both catalytic and catalyst-free modes, at 950 °C, which is significantly lower than that of the conventional carbothermal reduction and nitridation process for AlN. Metal (Au, Pt, Al) coated silicon (Si) substrates have been used to produce the AlNNTs, where the metal nanoparticulates formed at the high temperature acted as the nucleation sites for the AlNNTs growth.



4.2 Results and discussion

The as-grown AlNNTs on silicon substrates coated with an Au layer of various thicknesses were shown in Fig. 4.1a-c. AlNNTs grown on a 7 nm Au covered Si substrate exhibited a mean diameter of 10 nm at the apex, 80 nm at the base, and 250 nm in length (Fig. 4.1a). AlNNTs grown with progressively thicker Au layers produced longer nanotips (300-3000 nm) with wider apex (20-100 nm) and base (100-700 nm) diameters (Fig. 4.1b-c). Typical cross-sectional SEM image of AlNNTs is shown in Fig. 4.1d. This image displays a high density of quasi-aligned AlNNTs uniformly distributed over the entire substrate. The tip like morphology suggests that

the growth rate of the AlNNTs along the axial direction far outpace the growth rate along the radial direction. Along with the AlNNTs containing pure Al nanocrystals at its base some unreacted metallic Al residue could be found. The beauty of this VTCP technique lies in the size control of the nanotips which can be simply achieved by adjusting the thickness of the gold layer keeping the other growth parameters such as temperature and gas flow rates fixed. However, a number of other metals, such as aluminum (Al) (Fig. 4.2a) or platinum (Pt) (Fig. 4.2b), can be used to produce the AlNNTs since the eutectic temperatures of these metals with silicon lie below the reaction temperature of 950 °C. Furthermore, AlNNTs can be grown on even bare Si (without metal coating) (Fig. 4.2c) but they exhibit relatively poor morphology, indicating that metal coating is not indispensable for the growth, but it does help in controlling the morphology of the AlNNTs and perhaps some increase in the yield. But to come to any such conclusion, a closer look at the initial stages of growth was deemed necessary. SEM images in Fig. 4.3a-c demonstrate the initial growth of AlNNTs. The Al nanocrystals form within the first 20 minutes of growth and can be easily seen at the base of the AlNNTs (Fig. 4.3a). Figure 4.3b and 3c represent the morphology during the first 20 and 25 minute of growth, respectively, with typical nanotip formation completed in 25-30 minutes. The corresponding energy dispersive X-ray spectroscopy (EDS) elemental analysis of the nanotip body and nanoparticles



lying at the base of the nanotip is shown in Fig. 4.3d. It is quite clear that the nanotip body showed a much pronounced nitrogen component whereas no Au signal could be obtained from the apex of such tips marked (A) in Fig. 4.3c which excludes the possibility of VLS growth mechanism. The crystallites lying at the base of the nanotips, marked (B) in Fig. 4.3c, from which the nanotips evolved, yielded signals predominantly from Al, Au, and Si with no or little nitrogen component (Fig. 4.3d). The carbon and copper signals in Fig. 4.3d come from the amorphous carbon coated copper grids used for the TEM measurements. Two interesting inferences can be drawn from Fig. 4.3d. First, the nanocrystal at the base is predominantly Al, and second, the Al at the tip is compounded with nitrogen. Both of these facts will be corroborated from the XRD results to be discussed later. However, the establishment of the AlN phase in the nanotips comes conclusively from the TEM and XRD results.

Presence of Au along with Al in the nucleating crystallites only, indicates that either pure gold or a gold silicide phase may be controlling the nucleation and the smooth and finer morphology of the AlNNTs. In fact, the thickness of the Au layer is the key to the resultant morphology of the AlNNTs (Fig. 4.1). Au redundancy during growth resulted in larger and corrugated edge morphology of the AlNNTs (Fig. 4.2c). The fact that AlNNTs can be grown on bare silicon (Fig. 4.2c) as well as on silicon covered with Al (Fig. 4.2a) indicates that a self catalytic role of pure aluminum



nanocrystals, cannot be ruled out. Al vapors condense as crystalline Al on the catalytic gold or the gold-silicide sites, and we believe that these crystallized Al nanoparticles present at the bases of the AlNNTs served as the nucleation sites for subsequent AlNNTs growth following deposition of reacted Al and N vapors.



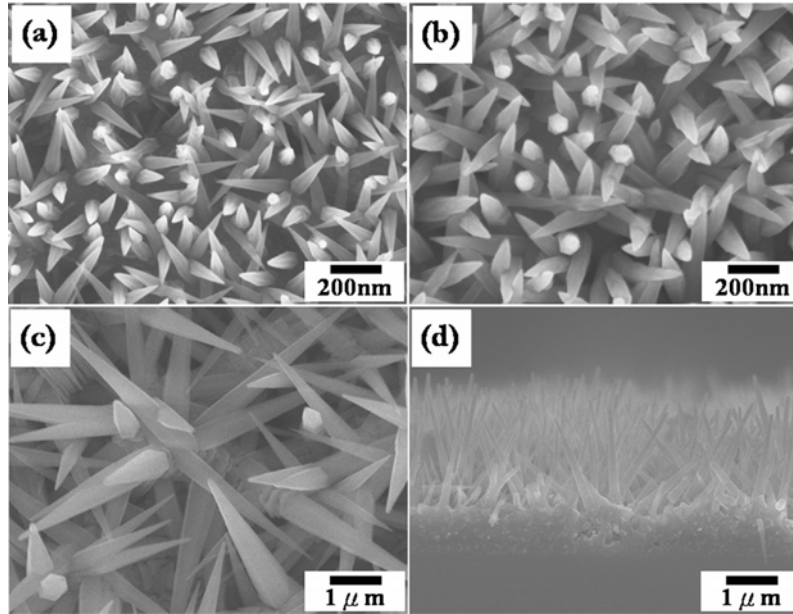


FIG. 4.1 Typical SEM images of the AlN nanotips grown with (a) 7 nm, (b) 15 nm, and (c) 50 nm thick Au layer on Si. (d) Typical cross section SEM image of AlN nanotips grown with 15 nm Au coated Si substrate.

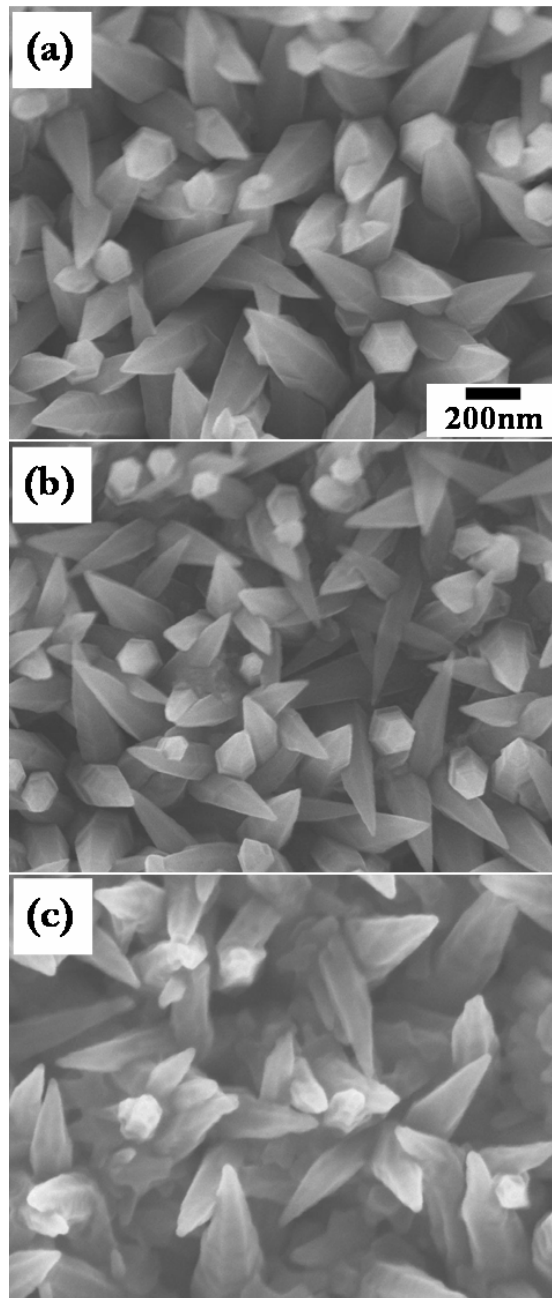


FIG. 4.2 SEM images of AlN nanotips grown with (a) Al (15 nm), (b) Pt (15 nm), (c) no metal coating, on the Si substrate, respectively.

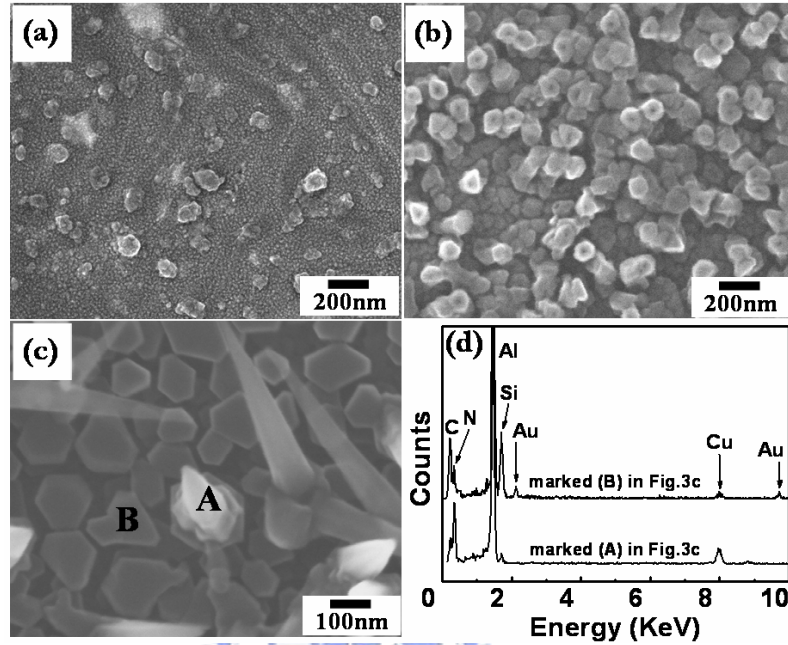


FIG. 4.3 SEM images of AlN nanotips grown with Au (15 nm on Si) for (a) 15 min, (b) 20 min, (c) 25 min, and (d) the corresponding TEM-EDS spectra of the AlN nanotip and nanoparticle marked (A) and (B) in Fig. 4.3c.

In order to investigate the structure evolution of the AlNNTs, XRD analyses were performed at various stages of growth. As shown in Fig. 4.4a, the XRD data for the initial stage shows the presence of Al only whereas the corresponding data for the later stage shows a number of relatively sharp diffraction peaks that can be indexed to a hexagonal structure with lattice constant of $a = 0.311$ nm and $c = 0.498$ nm, which is consistent with the standard value for bulk hexagonal AlN (JCPDS 25-1133). While there are negligible signals from Au, the Al signals remain detectable in the XRD spectra, presumably due to the un-reacted aluminum crystallizing on the Au particles at the base of the AlNNTs during the initial high temperature processing of the reactants. It should be noted that all samples showed similar XRD patterns, indicating that the nanotips have good structural reproducibility in all deposition conditions used. This kind of reproducibility is a pre-requisite for any synthetic technique to be accepted as a major force.

Raman spectra of the AlNNTs were obtained at room temperature as shown in Fig. 4.4b, to further the knowledge of its structure. In this spectrum, distinct first-order modes of the peaks corresponding to A_1 (TO), E_2 (high), E_1 (TO) and A_1 (LO) modes at around 609.4, 653, 668 and 894 cm^{-1} , respectively, were observed. These Raman peaks are signatures for wurtzite AlN as reported previously for bulk, thin film, nanowires, and nanobelt structures [126,127,158-159]. However, these peak

positions were given alternative assignments in an earlier work [160]. These Raman peaks were not detected from the samples containing predominantly nanocrystals (such as those grown for 15 min or less as shown in Fig. 4.3a), suggesting that AlN signal is indeed originating from the well crystallized tips.

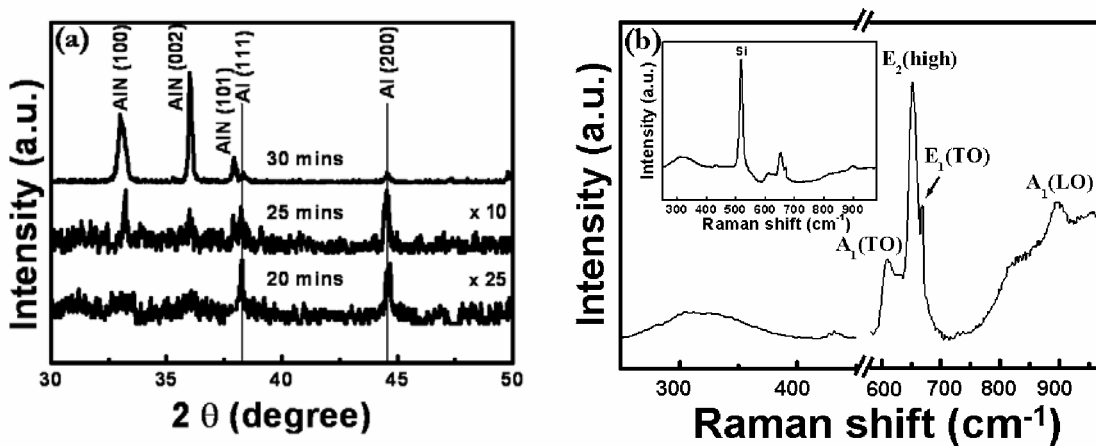


FIG. 4.4 (a) Typical XRD spectra taken at three different stages of growth. The initial stage shows only Al signals and the corresponding one with fully grown nanotips shows two crystalline phases of Al and hexagonal AlN. (b) Raman spectrum, with a discontinuous abscissa, of the AlN nanotips on silicon substrate. Inset shows a continuous Raman spectrum of the AlN nanotips with the silicon signal included. All the XRD and Raman spectra were measured from samples prepared on 15 nm Au coated Si substrate.

High resolution TEM along with the selected-area electron diffraction (SAED) was employed to further analyze the structure and crystallographic orientations of these AlNNTs. All nanotips appear to be homogeneous without any grain boundaries, indicating the single crystal nature of each individual AlNNT. As shown in Fig. 4.5b, the HRTEM image of the apex reveals a lattice spacing of 0.497 and 0.269 nm (in parallel and normal to the axial direction) that is in good agreement with the d_{001} and d_{1-10} spacing of h-AlN, respectively. Corroborating with the SAED pattern, the direction of the AlNNTs was found to be [001] along the long axis (inset, Fig. 4.5b). AlN whiskers growing along $\{10\bar{1}0\}$ and $\{12\bar{1}0\}$ close packed planes have already been reported [161], and [001] growth direction of some 1 dimensional nanostructures was also observed [159,162]. HR-TEM examination and SAED performed over several nanotips made from different thickness of gold films and also at different locations on each nanotips yielded similar diffraction patterns. Elemental analysis on a single AlNNT body (Fig. 4.5c) done by electron energy loss spectroscopy (EELS) measurements clearly established a stoichiometric AlN composition with Al (Fig. 4.5d) and N (Fig. 4.5e) mapped with similar rate of occurrence.

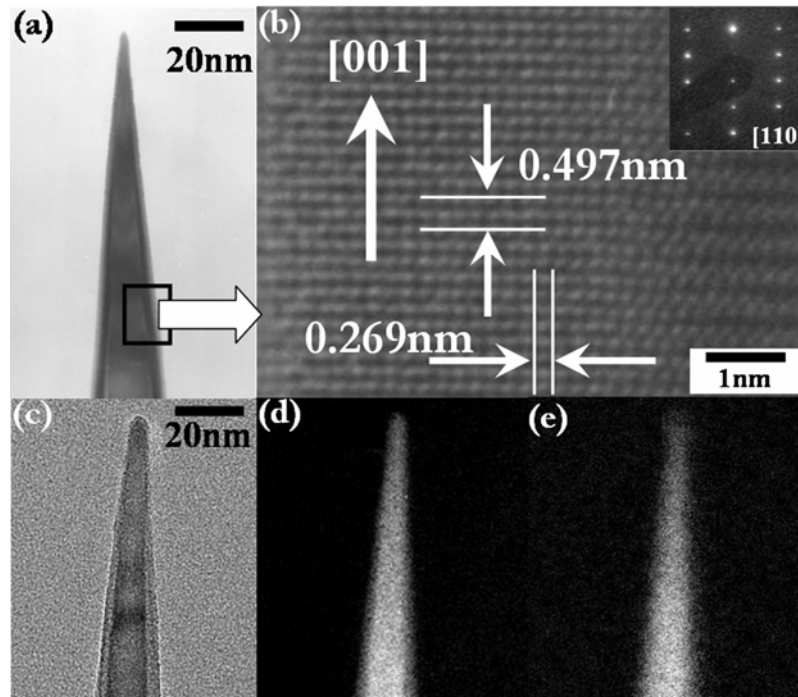
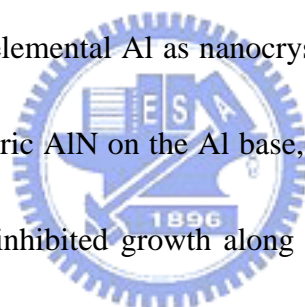


FIG. 4.5 (a) TEM image of an AlN nanotip, (b) High resolution TEM image of a single AlN nanotip with clear lattice images. The inset shows a SAED pattern of the nanotip indicating the single-crystalline nature with [110] zone axis and the growth direction along [001]. (c) TEM of a single AlN nanotip with corresponding (d) Al, and (e) N mapping using EELS.

4.3 Growth mechanism of AlNNTs

Based on the above results, a complete growth mechanism of AlNNTs can be proposed whose schematic description is given in Fig. 4.6. As the reaction temperature was ramped up from room temperature to 950°C, droplets of catalyst metals (Au, Pt) or their respective silicide phases will be formed in the vicinity of the respective eutectic temperatures. In the case of uncoated Si, the self catalytic Al or Al alloy droplets, possibly Al-Si, is believed to be the nucleation site. Al vapors, generated above 660°C, dissolve in these droplets supersaturating them, finally resulting in the expulsion of elemental Al as nanocrystals. Fully reacted vapors of Al and N deposits as stoichiometric AlN on the Al base, where a rapid growth along the axial direction [001] and an inhibited growth along an orthogonal (radial) direction was observed giving rise to the tip shape. Physically speaking, progressively decreasing surface diffusion lengths (increasing sticking coefficients) of oncoming AlN radicals onto the growth surface along the axial direction will result in a reducing cross section of the growing nanostructure promoting the tip shape. This argument gets support from our observation that an increased growth temperature, hence increased diffusion lengths, resulted in AlN nanorods instead of nanotips, which will be reported separately. The diffusion length of the radicals is a strong function of growth temperature and is believed to be key parameter in controlling the morphology



of the 1D nanomaterial. The growth inhibition along the radial direction is possible via passivation of the dangling bonds on that surface by, possibly, oxygen.

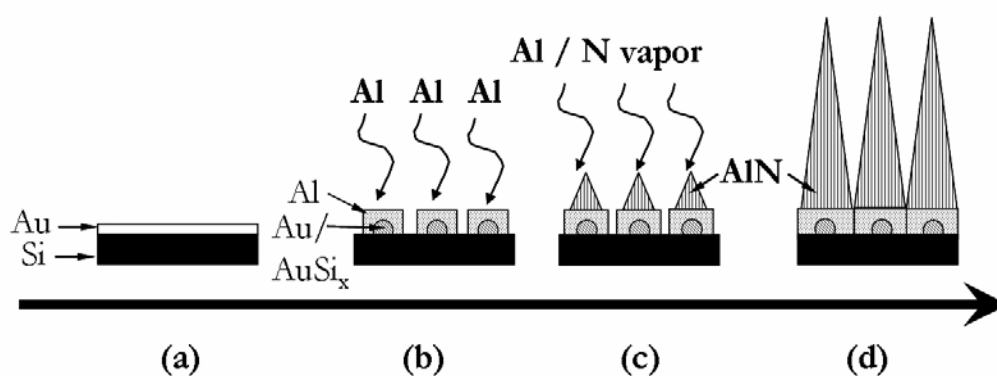


FIG. 4.6 Schematic diagram of growth mechanism of AlN nanotips. (a) Au layer was coated on the Si substrate. (b) Gold or Gold-silicide nanoparticles shape up as the nucleation sites for the subsequent aluminum deposition. (c) Aluminum and nitrogen are absorbed on the nucleation sites bringing about the initial growth of AlN nanotips. (d) AlN nanotips elongate with time when reaction temperature is kept at 950 °C.

As it was mentioned in a review by Felice *et al.* [161], the aluminum side of AlN can bond to the silicon side of SiC (001) whereas the nitrogen face prefers the carbon side. In our case, the basal (001) plane is the Al-terminated surface having the higher growth rate. From the evidence of etching of AlN single crystal [163], it was found that the angle between the basal plane and tilted plane of the AlN pyramid was about 61.6° , which is close to the angle between (001) and $(1\bar{1}1)$ planes in AlN. The $(1\bar{1}1)$ planes are energetically stable because of a smaller number of bonds cutting through these planes. The energetically stable surface was exposed after the completion of etching. In the case of epitaxial AlN thin film on SiC substrate, there exist a stable plane (namely $(1\bar{1}2)$) with 43° angle with respect to the basal plane [164]. However, in our case, the angle between basal plane and tilted plane of the nanotip is much higher at roughly 81° corresponding to the angle between basal plane (001) and (221). It is thus suggested that these AlN nanotips are bound by (221) planes, which are “*nongrowth*” surfaces, having fewer dangling bonds and hence non-reactive, and the (001) basal plane provides the growth surface. Fig. 4.7a shows the atomic arrangements in an AlN crystal with the “*nongrowth*” planes (221) observed in the present work as well as $(1\bar{1}1)$ [163] and $(1\bar{1}2)$ [164] (Fig. 4.7b and 4.7c) reported previously. The similar dangling bond environments in each of these cases will rationalize the existence of the stable higher index plane observed in this case of AlN

nanotips. A similar basis for facet formation in GaAs ridge morphology has recently been reported [165]. The (221) planes can be H or N terminated depending on the bond enthalpies of Al-H and Al-N, where the former is smaller. The rapid etching rate on the N- terminated surface may lead to dangling bond passivation by H, which is decomposed from the ammonia gas at 950 °C. However at such high reaction temperatures, the stability of Al-H may be a question. In general, a high growth rate along the (001) basal plane with the stable (221) tilted surface generates the shape of the AlNNTs. Clearly the nanotips, with higher aspect ratios and high index tilted planes, are different morphological species than the pyramids or the ridges observed earlier.

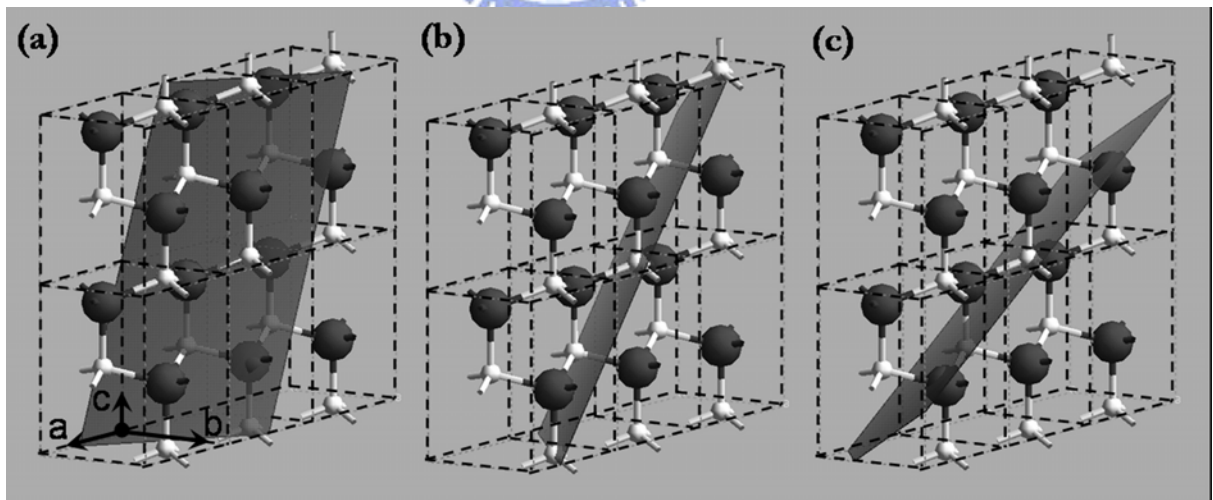


FIG. 4.7 Atomic arrangement in AlN crystal showing the stable “nongrowth” surfaces of (a) (221), (b) $(\bar{1}\bar{1}1)$, and (c) $(\bar{1}\bar{1}2)$ making angles of 81°, 61° and 43°, respectively,

with the basal plane. The c-axis shown in the figure is [001] direction.

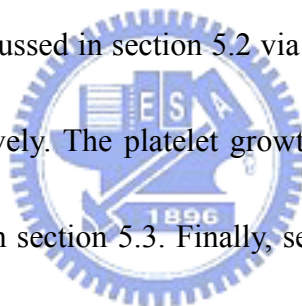
4.4. Summary

Aluminum nitride nanotips growth on metal (gold, aluminum and platinum) coated or even uncoated silicon substrates via vapor transport and condensation process has been demonstrated. A pure metal or metal silicide phase acts as the nucleation site for the precipitation of crystalline aluminum seed for the aluminum nitride nanotip growth. In case of aluminum nitride nanotip growth on bare silicon, a self catalytic activity of aluminum itself or its silicide phase was visualized. The resultant AlN nanotips exhibit a monodispersed apex angle distribution. Structural properties of the nanotips studied by TEM and XRD suggest that these tips have hexagonal crystal symmetry with a preferred growth direction of (002) along the long axis and a stable (221) plane as the tilted surface.

Chapter 5

Structural Evolution of AlN Nano-structure: Nanotips and Nanorods

In this chapter, Nanostructures produced on the silicon substrates at different temperatures set-points, controlled between 950 and 1200 °C, were studied. An observation in the crystal morphology change from tip-like structure to rod-like crystallites is reported. The surface morphology, structure, and composition properties of the as-deposited samples are characterized in detail. The overall structural and morphological results are discussed in section 5.2 via FESEM, Raman scattering, and XRD measurements, respectively. The platelet growth model, which is governed by the n_1/n_2 ratio are discussed in section 5.3. Finally, section 5.4 will make a summary according to the obtained results.



5.1. Nanotips and Nanorods

A series of experiments were carried out to study the effect of growth temperature (T_d) variation on the shape evolution of the AlN products. Figure 5.1a-d shows SEM images of AlN nano-products grown for 30 min on the Au coated Si substrates at different T_d of 950, 1000, 1100, and 1200°C, respectively. At $T_d = 950^\circ\text{C}$, the AlNNTs evolved (Fig. 5.1a). As T_d increased, a (001) facet (c-facet) appeared on the

top of the nanotips, forming a flat section at the top instead of the tip shape. The area of this (001) facet increased with increasing T_d as shown in Fig. 5.1b - d. As shown clearly in Fig. 1d, $T_d = 1200^\circ\text{C}$ produced AlN nanorod (AlNNR) which has a simple six-sided faceted structure. The cross-section of AlNNTs and AlNNRs were both hexagonal.

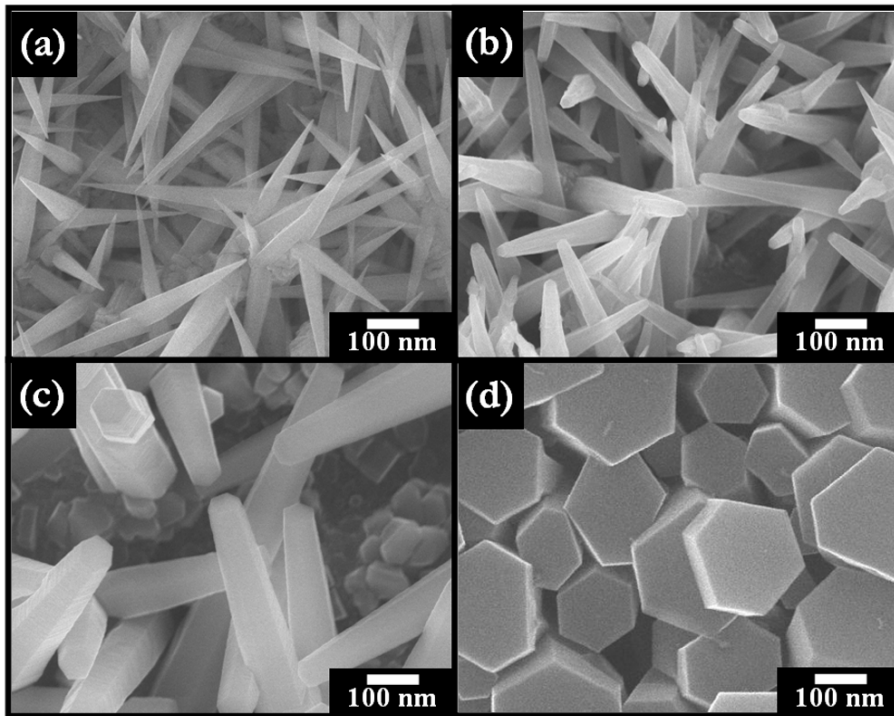


FIG. 5.1 Typical SEM images of the AlN nanotips on silicon substrates (coated with 15 nm of gold) grown under (a) 950, (b) 1000, (c) 1100, and (d) 1200 °C, respectively.

The cross-sectional SEM images of AlNNTs and AlNNRs shown in Fig. 5.2a and 2b, respectively, indicates their relative dimensions. The inset of Fig. 5.2a and 2b depict the early stages of growth of AlNNTs and AlNNRs, respectively. It indicates that the shapes of the AlN nanostructures were probably decided at the very early stages of the growth. Fig. 5.2c represents the X-ray diffraction analysis of the AlN nanostructures. It shows the strongest reflection of the (002) plane compared to (101) of the h-AlN, indicating a preferential growth perpendicular to the basal plane along [001]. The Raman spectra of the AlNNTs and AlNNRs, as shown in Fig. 5.2d, were collected using Ar⁺ laser as the excitation source. Three clear Raman-active phonon modes can be observed. These are in agreement with those of the h-AlN crystal [126].



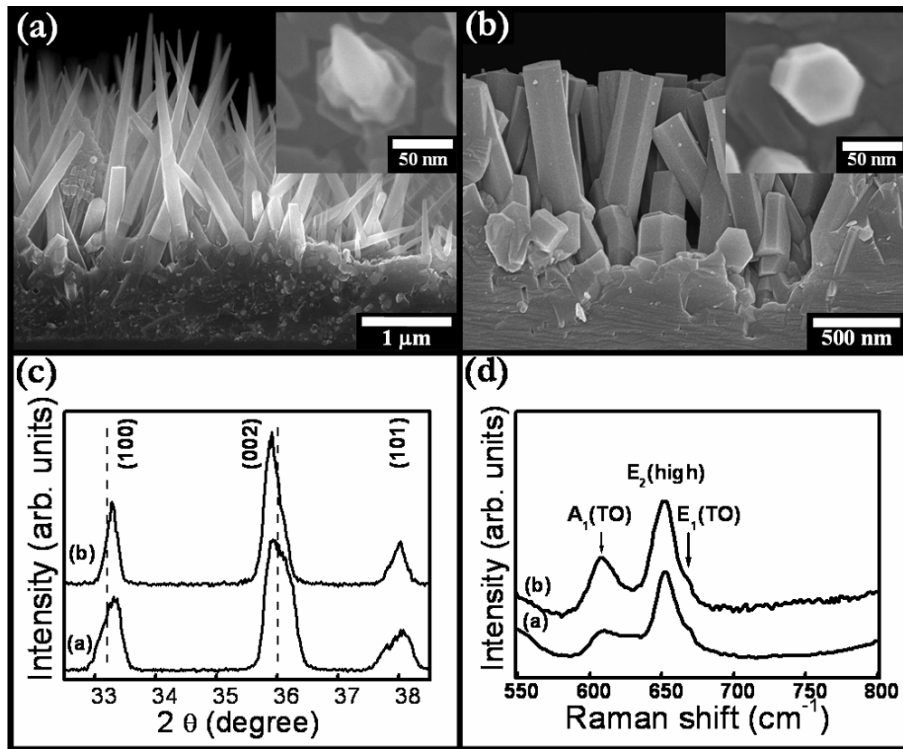


FIG. 5.2 Typical cross section SEM image of AlN nanotips grown coated with 15 nm Au coated Si substrate under (a) 950, (b) 1200 °C, respectively. Inset in (a) and (b) show the SEM image of AlN nano-product grown for 25 minutes, respectively. (c) Typical XRD and (d) Raman spectra taken from the AlN nanostructures in Figure 2(a) and 2(b), respectively. The two vertical dashed lines in Figure 2(c) represent bulk AlN positions for (100) and (002) reflections (JCPDS 25-1133).

5.2 Structural revolution of AlN nanostructures

The shape evolution of the AlN nanostructures as a function of T_d is interesting as the result (Fig. 5.1) shows. The digestion of the results presented in this paper as well as our earlier work on AlNNTs [166,167] yields certain facts as listed below:

Observation 1: AlN nanostructures have pure Al signatures from the seed crystal present at its base [166];

Observation 2: The body of the nanostructure is purely hexagonal AlN growing along [001] and no metallic Al phase is present [166,167];

Observation 3: A high aspect ratio (>10) nanotip structure, having apex angles of $\sim 14^\circ$, produced at $T_d = 950^\circ\text{C}$ modifies into a low aspect ratio (~ 5) flat top ((001) facet) AlNNRs at $T_d = 1200^\circ\text{C}$. Any proposed growth model should explain these listed facts of which the last one is of most importance.

We begin with a discussion on a diffusion mediated growth mechanism which is the most obvious as we are dealing with a temperature activated process. The growth of AlN nanostructures proceeds by the transport of Al vapors to the growth region as the temperature inside the quartz tube is ramped up. Note, although a thin Au layer, intended to be a catalyst, was used on the Si substrate, it was not detected at the tip of the nanostructures or in its body. Again the AlNNTs could be obtained even without any Au catalyst on the substrate. This allowed us to exclude a VLS mechanism and

pursue the vapor-solid (VS) route instead. We introduce a diffusion mediated growth mechanism here. Al vapors landing on the growth surface will migrate with a large diffusion length, L_{Al} , and can be adsorbed and deposited on the substrate as Al itself when T_d is low (but above 660°C, the melting point of Al powders). This results in the basal Al islands since T_d is not sufficient to dissociate the nitriding gas NH_3 . This explains *observation 1*. The Al vapors may then encounter and react with NH_3 or its dissociation products when T_d is higher (dissociation temperature for NH_3 is) producing AlN following eqn. 1:



Then AlN will migrate in molecular form with a diffusion length, L_{AlN} . Consequently, an effective diffusion length L_{eff} is defined as

$$L_{eff} = L_{Al} + L_{AlN} \quad (2)$$

where L_{Al} and L_{AlN} are temperature activated according to the following [168]

$$L_{Al} \sim t_{Al}^{1/2} \exp\left(-\frac{E_{Al}}{2k_B T}\right) \quad (3)$$

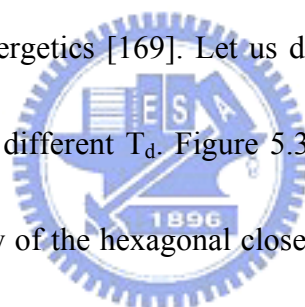
$$L_{AlN} \sim t_{AlN}^{1/2} \exp\left(-\frac{E_{AlN}}{2k_B T}\right) \quad (4)$$

t and E are the diffusion times and activation energies for surface diffusion, respectively, and k_B is the Boltzmann constant. The AlN molecule can be deposited at

a low energy site and contribute to the growth or can be desorbed also. This happens in a condition close to $t_{Al} \sim t_{AlN}$, and $L_{Al} \sim L_{AlN}$. Thus, to permit the growth of AlN from a predominantly metallic Al seed, $L_{AlN} \geq L_{Al}$. Above the dissociation temperature of NH_3 the thermodynamics of the system (negative Gibb's free energy for eqn. 1) promotes the formation of AlN. This explains *observation 2*.

To address *observation 3* we discuss the anisotropy as well as strains that might be present during the growth. We are now studying the growth of AlN on Al seed crystal. The initial islands may have edges beveled at an angle θ , with respect to the substrate,

determined by the surface energetics [169]. Let us discuss first the diameters of the AlN nanostructures grown at different T_d . Figure 5.3 shows a schematic drawing of the cross-section and top view of the hexagonal close packed (hcp) wurtzite structure of AlN crystal with the Al- terminated (001) face and the N- terminated $(00\bar{1})$ face.



From our TEM and XRD results we have already established that we have a [001] growth direction for all kinds of nanostructures grown at different T_d . Number of dangling bonds available per oncoming growth precursors, say Al, on the Al (001) and N $(00\bar{1})$ face are 3 and 1, respectively (Fig. 5.3a). The lateral facets have two kinds of surfaces, namely A and B, which have 2 and 1 dangling bonds, respectively, per oncoming Al atom. Hence on the average each Al atom has 1.5 dangling bonds available for bonding to a N atom on the lateral faces. Evidently, based on the

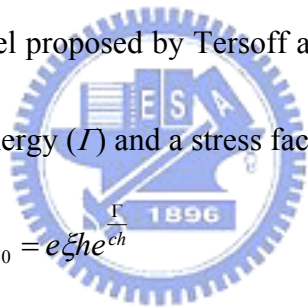
availability of dangling bonds, diffusion lengths on the lateral faces of the hexagonal islands will be less than that on the N-terminated $(00\bar{1})$ face [170]. This will lead to an anisotropy in the growth rate resulting in large platelets/islands of AlN following eqn.

(1). Since the diffusion length is temperature activated, a larger T_d will produce larger but thin platelets. This exactly explains why the AlNNTs produced at 950 °C (Fig. 5.1a) had smaller base diameters than the AlNNRs (Fig. 5.1d) prepared at 1200 °C.

However, this also means that the AlNNRs are closer to equilibrium than the AlNNTs which is understandable because of a larger diffusion length of the AlN precursors at higher T_d .

Following the model proposed by Tersoff and Tromp [169], the island size

(a_0) is related to the surface energy (Γ) and a stress factor (c) by the following:



$$a_0 = e\xi h e^{\frac{\Gamma}{ch}} \quad (5)$$

where h is the height of the initial island and $\xi = e^{-1.5} \cot \theta$. This model predicts that if $ch \gg \Gamma$, then the island sizes a_0 will be smaller. So the AlNNTs having a smaller

base diameter are the stressed ones. However the model presumed a slant edge ($\theta \neq$

90°) island and cannot directly predict a perfect ($\theta = 90^\circ$) wide base rod-like crystal,

since then $\xi = 0$ and $a_0 \rightarrow 0$. There are indications that such perfect ($\theta = 90^\circ$) islands

[171] can be the seeds for nanorod growth via the VS mechanism.

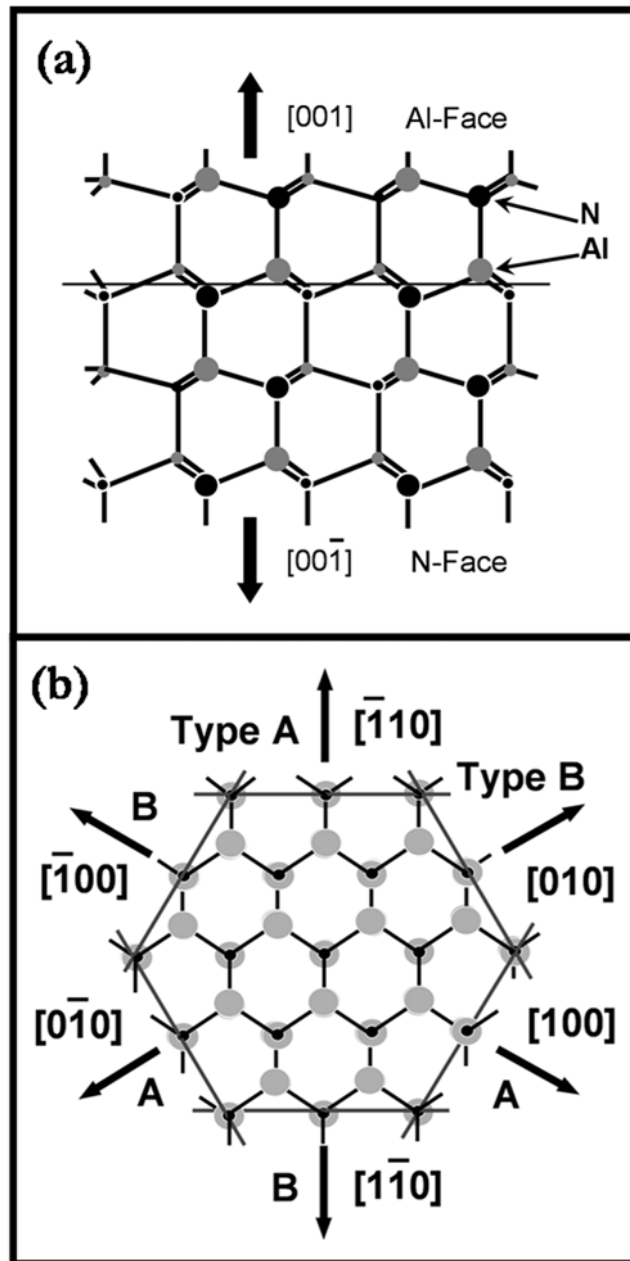
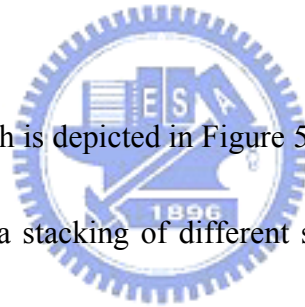


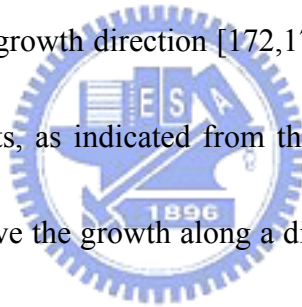
FIG. 5.3 (a) The cross-sectional view of hexagonally close packed wurtzite crystal structure of AlN. (b) The plan-view of a bilayer of hcp AlN. There are two types of lateral growth directions marked as A and B.

Now consider the vertical growth of the AlN nanostructures along the [001] direction which is an Al-terminated face (Fig. 5.3a). For $T_d \geq 950$ °C, the dissociation rate of NH_3 was very fast and the Al vapor pressure was high, suggesting $t_{Al} \rightarrow 0$ and $0 \leftarrow L_{Al} \ll L_{AlN}$; so $L_{eff} = L_{AlN}$. When Al atoms arrive at the growth face, every Al atom has three bonds connecting with three N atoms. That means, $E_{AlN}(001) \gg E_{AlN}(00\bar{1})$ and also $E_{AlN}(001) > E_{AlN}(010)$, resulting in growth rates $R[001] > R[010] > R[00\bar{1}]$. A higher growth rate along the Al-terminated [001] direction is observed than that along the normal to the lateral faces. When this condition is satisfied, we expect an aspect ratio >1 .



The beauty of crystal growth is depicted in Figure 5.4. The AlNNT produced at 950 °C (Fig. 5.4a) clearly shows a stacking of different sized platelets along the growth direction generating the tip shape. The platelets/islands behaves similar to a building block and a repetitive stacking of these, layer by layer, gives rise to the nanostructures. A similar stacking of double bilayer steps has been observed along the sidewalls of InN pyramids also [171]. However the existence of these distinct platelets started to disappear from $T_d = 1000$ °C (Fig. 5.4b) signifying deposition along the lateral facets of the platelets. A significant portion of this deposition may be due to adatom hopping down a step. Fig. 5.4a – d demonstrates the growth along the radial direction of the nanostructures due to adatom hopping as a result of a reducing Ehrlich- Schwoebel

barrier, and increased diffusion lengths as T_d is increased. When $T_d = 1100$ °C, the top (001) facet clearly appears and the lateral face growth becomes more pronounced giving it a smoother appearance than that observed during 1000 °C. However the conical nature of the structure is still maintained. As T_d creeps up to 1200 °C, the diffusion length was sufficient to push the system towards equilibrium resulting in larger hexagonal platelets and growth along the lateral facets generating the pillar like structure of the AINNRs with a near perfect uniformity in diameter. Note that the existence of the Ehrlich- Schwoebel barrier at low T_d will also give rise to a large driving force along the [001] growth direction [172,173]. In addition, the stress along the basal plane of the platelets, as indicated from the smaller base diameters of the AINNTs, is also known to drive the growth along a direction perpendicular to it. This explains why the AINNTs have a higher aspect ratio than the AINNRs.



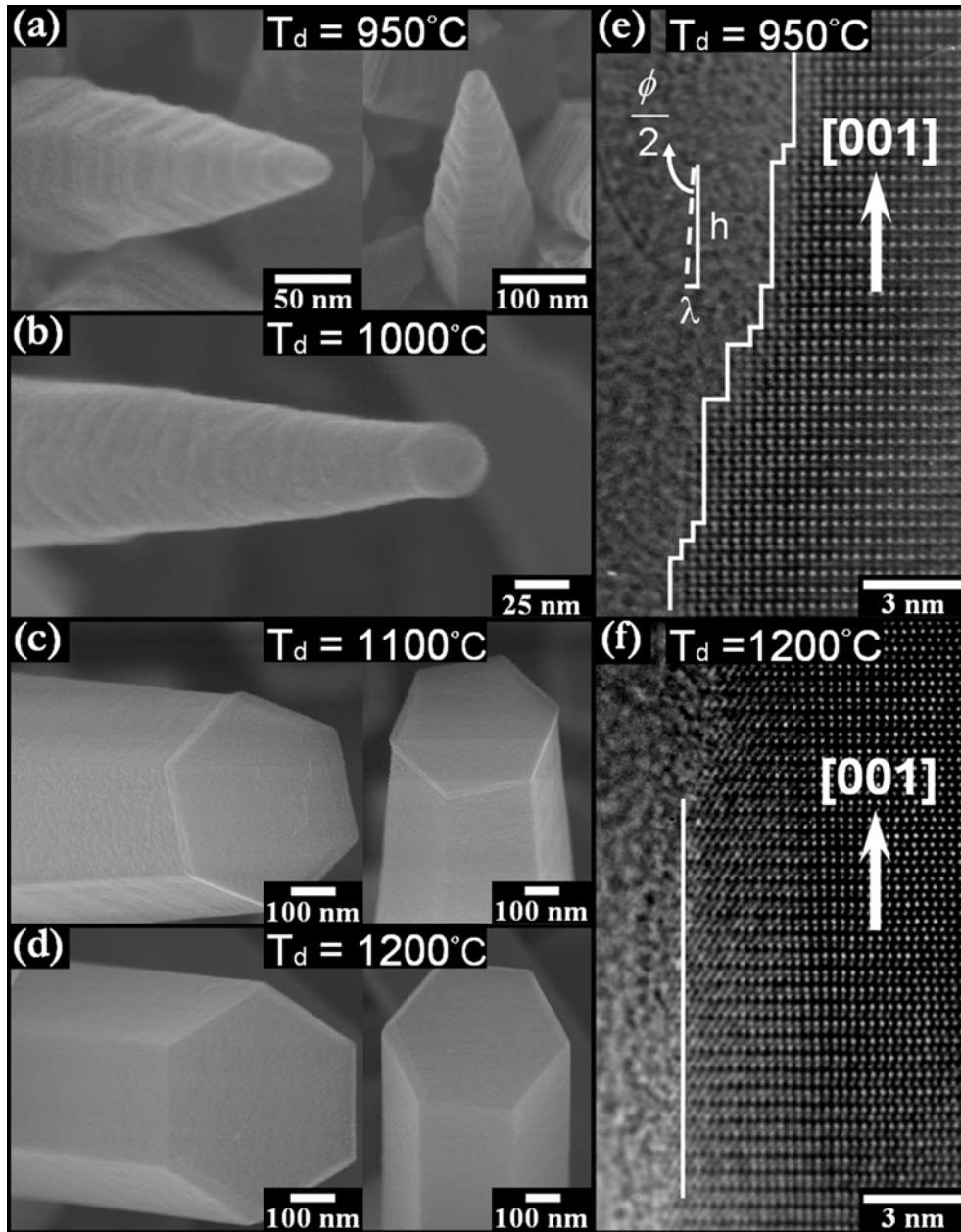
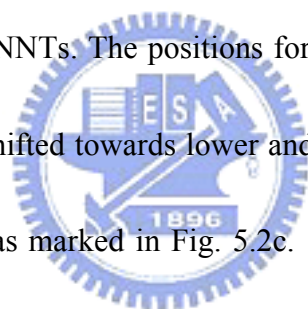


FIG. 5.4 (a-d) High resolution SEM images of the AlN nanostructures produced at different growth temperatures; (e) HRTEM image of the edge of AlNNTs showing the step edges, including the step height (h) and step spacing (λ); a schematic aiding in the estimation of the semi apex angle ($\phi/2$) is also shown; (f) HRTEM image of the edge of AlNNRs showing uniform diameter without tapering via step edges.

Lastly, the origin of the tip shape has to be addressed for the growth at 950 °C. Since the growth units were clearly identified as islands/platelets stacked on each other, it is only obvious that a certain arrangement of these produced the tip shape. Careful TEM observations proved what we conjectured in our earlier work [166]. This is a pyramidal growth of 3D islands growing on top of each other (Fig. 5.4e). A rapid 2D nucleation, which may be due to precursor supersaturation, can lead to these 3D islands/platelets. The tilted surface of the AlNNTs consist of a train of parallel steps of polyatomic step heights (h), with a small step spacing (λ) (Figure 5.4e) and a high step density ($p = h / \lambda$) [10]. Clearly, $h = n_1 \times d_{001}$, and $\lambda = n_2 \times d_{110}$, where d_{001} and d_{110} are the lattice spacings along and perpendicular to the growth direction, respectively, as determined from TEM studies [174] and n_1, n_2 are integer. The apex angle (ϕ) of the AlNNTs, as determined microscopically, is dictated by the large h/λ ratio and hence small magnitudes of the ratio, though present, are neglected. Calculating h/λ from the TEM micrograph shown in Fig. 5.4e we can roughly estimate a set of ϕ values for our AlNNTs which falls within 8-22° in agreement with that measured from the SEM images. Note that the apex angles mentioned here are 2D projections of the solid angle at the apex. For a particular material system the lattice spacings are constant and hence h/λ is a function of n_1/n_2 . Hence following this model, a set of apex angles for solid nanotips or pyramids of any material system (for

example, GaN, InN, AlN) can be predicted based only on the n_1/n_2 ratio. The AlNNRs does not exhibit these step structures (Fig. 5.4f). The growth model proposed in ref. 8 is inadequate in a sense that reducing precursor concentration is a general reaction feature and if the model is true should necessarily produce nanotips, which is not the case. However their observation is very similar to us since they can generate the nanotips and nanorods as a function of growth temperature alone and that has been attributed to diffusion mediated process. Our results indicate rather a stress related phenomenon for the step spacing (λ) and a high Ehrlich-Schwoebel barrier to preserve the steps that build up the AlNNTs. The positions for the (002) and (100) reflections from the nanostructures are shifted towards lower and higher 2θ values, respectively, from their bulk counterparts as marked in Fig. 5.2c. Note that the $[\bar{1}\bar{1}0]$ and $[100]$ have identical 2θ positions in the XRD and that $[\bar{1}\bar{1}0]$ is the radial direction of the nanostructures shown in the TEM images in Fig. 5.4e and f. The tensile and compressive stress along the axial and radial direction, respectively, of the AlNNTs and AlNNRs is clearly visible from the XRD spectra (Fig. 5.2c). The AlNNRs produced at 1200 °C manages to counter the stress deformation while AlNNTs produced at a lower temperature yields to it by getting tapered as growth progresses.



5.3 Magic ratio

Following the report in chapter 5.2, we deliver a model of platelet growth of AlN nanostructures which will lead to a train of parallel steps of polyatomic step heights (h), with a small step spacing (λ). It is obvious that the step height and spacing should be the integer multiple of lattice spacing of d_{001} and $d_{\bar{1}10}$, respectively, are known if the growth direction was fixed at [001]. The angle (θ_c) between the existing facet and basal plane can be compute by the following expression.

$$\tan \theta_c = \frac{h}{\lambda} = \frac{n_1 \times d_{001}}{n_2 \times d_{\bar{1}10}}$$

where d_{001} and $d_{\bar{1}10}$ for AlN are 0.497 and 0.269 nm, respectively. Therefore the angle (θ_c) can be realized by varying the n_1/n_2 ratio. As shown in Table 5.1, we illustrate a series of n_1/n_2 ratio, θ_c (calculated from n_1/n_2 ratio), θ_r (the angle between the cleaved facet and the basal plane in the crystallography point of view, CaRIne v 3.1), existing facet (adapted from CaRIne v 3.1), apex angle and reported literatures.

The digestion of the results presented in table 5.1 as well as listed references on AlN provide certain information as lined up below: First, the apex angle (ϕ) will be determined by the a simple n_1/n_2 ratio (or h/λ); second, θ_c are highly match with θ_r , especially for the n_1/n_2 ratio equal to 0.5 [164], 1 [175], and 3.5 [166], respectively which were well documented; third, the apex angle will not be a any number, it is confined by the n_1/n_2 ratio, showing a discrete distribution; fourth, the apex angle

seems to be predictable following the table.

Surprisingly, this model can be applied for group-III nitride nanostructures with long axis at [001] direction as shown in table 5.2, 5.3, and 5.4. The identical calculation was made for the GaN, InN and BN, respectively. Here we propose a regulation which can be applied to predict and describe the tip formation and apex angle variation of group-III nitride nanostructures. However, the reason for the apex angle variation is not clear for the moment.



Table 5.1 n_1/n_2 ratio of AlN

AlN: Growth direction: [001]

$$\tan \theta_c = \frac{n_1 \times d_{001}}{n_2 \times d_{\bar{1}\bar{1}0}} = \frac{n_1}{n_2} \times (1.847), \text{ where } d_{001} = 0.497 \text{ nm}; d_{\bar{1}\bar{1}0} = 0.269 \text{ nm}$$

n_1/n_2	θ_c	θ_r	facet	ϕ	Reference
0.1	10.4	x			
0.2	20.2	x			
0.25	24.7	x			
0.33	31.3	x			
0.5	42.7	42.7	(1-12)	94.6	[164]
0.75	54.1	x			
1	61.5	61.5	(1-11)	57.0	[163]
1.25	66.5	x			
1.5	70.1	70.1	(3-32)	39.8	
1.75	72.8	72.7	(111)	34.4	
2	74.8	74.8	(2-21)	30.4	
2.5	77.7	78.2	(332)	23.6	
3	79.7	79.7	(3-31)	20.6	
3.5	81.1	81.1	(221)	17.8	[166]
4	82.2	82.2	(4-41)	15.6	
4.5	83.1	83.2	(411)	13.6	
5	83.8	x			
5.5	84.3	84.1	(241)	11.8	
6	84.8	84.9	(431)	10.2	
6.5	85.2	x			
7	85.5	85.5	(441)	9.0	

Ref.: Pearson's Handbook of Crystallographic Data, p213.

Table 5.2 n_1/n_2 ratio of GaN

GaN: Growth direction: [001]

$$\tan \theta_c = \frac{n_1 \times d_{001}}{n_2 \times d_{\bar{1}10}} = \frac{n_1}{n_2} \times (1.876), \text{ where } d_{001} = 0.517 \text{ nm}; d_{\bar{1}10} = 0.275 \text{ nm}$$

n_1/n_2	θ_c	θ_r	facet	ϕ	Reference
0.1	10.6	x			
0.2	20.5	x			
0.25	25.1	x			
0.33	31.7	x			
0.5	43.1	43.1	(1-12)	93.8	
0.75	54.6	x			
1	61.9	61.9	(1-11)	56.2	[176]
1.25	66.9	x			
1.5	70.4	70.4	(3-32)	39.2	
1.75	73.0	72.9	(111)	34.0	
2	75.0	75.0	(2-21)	30.0	
2.5	77.9	78.4	(332)	23.2	
3	79.9	79.9	(3-31)	20.2	
3.5	81.3	81.3	(221)	17.4	
4	82.4	82.4	(4-41)	15.2	
4.5	83.2	83.3	(411)	13.4	
5	83.9	x			
5.5	84.4	84.2	(241)	11.6	
6	84.9	84.9	(431)	10.2	
6.5	85.3	x			
7	85.6	85.6	(441)	8.8	

Ref.: Pearson's Handbook of Crystallographic Data, p3492.

Table 5.3 n_1/n_2 ratio of InN

InN: Growth direction: [001]

$$\tan \theta_c = \frac{n_1 \times d_{001}}{n_2 \times d_{\bar{1}10}} = \frac{n_1}{n_2} \times (1.864), \text{ where } d_{001} = 0.570 \text{ nm}; d_{\bar{1}10} = 0.306 \text{ nm}$$

n_1/n_2	θ_c	θ_r	facet	ϕ	Reference
0.1	10.5	x			
0.2	20.4	x			
0.25	24.9	x			
0.33	31.5	x			
0.5	42.9	42.9	(1-12)	94.2	
0.75	54.4	x			
1	61.7	61.7	(1-11)	56.6	
1.25	66.7			46.6	
1.5	70.3	70.3	(3-32)	39.4	
1.75	72.9	72.8	(111)	34.2	
2	74.9	74.9	(2-21)	30.2	
2.5	77.8	77.8	(332)	24.4	
3	79.8	79.8	(3-31)	20.4	
3.5	81.2	81.2	(221)	17.6	
4	82.3	82.3	(4-41)	15.4	
4.5	83.1	83.3	(411)	13.8	
5	83.8	x			
5.5	84.4	84.2	(241)	10.6	
6	84.9	84.9	(431)	10.2	[104]
6.5	85.2	x			
7	85.6	85.5	(441)	8.8	
7.5	85.9	x			
8	86.0	86.0	(541)	8.0	

Ref.: Pearson's Handbook of Crystallographic Data, p4017.

Table 5.4 n_1/n_2 ratio of BN

BN: Growth direction: [001]

$$\tan \theta_c = \frac{n_1 \times d_{001}}{n_2 \times d_{\bar{1}10}} = \frac{n_1}{n_2} \times (1.847), \text{ where } d_{001} = 0.497 \text{ nm}; d_{\bar{1}10} = 0.269 \text{ nm}$$

n_1/n_2	θ_c	θ_r	facet	ϕ	Reference
0.1	10.8	x			
0.2	20.9	x			
0.25	25.5	x			
0.33	32.2	x			
0.5	43.7	43.7	(1-12)	92.6	
0.75	55.1	x			
1	62.3	62.3	(1-11)	55.4	
1.25	67.2	x			
1.5	70.7	70.7	(3-32)	38.6	
1.75	72.9	73.2	(111)	34.2	
2	75.3	75.3	(2-21)	29.4	
2.5	78.1	78.6	(332)	23.8	
3	80.1	80.1	(3-31)	19.8	
3.5	81.5	81.5	(221)	17.0	
4	82.5	82.5	(4-41)	15.0	
4.5	83.3	83.4	(411)	13.4	
5	84.0	x			
5.5	84.5	84.3	(241)	11.0	
6	85.0	85.0	(431)	10.0	
6.5	85.4	x			
7	85.7	85.7	(441)	8.6	

Ref.: Pearson's Handbook of Crystallographic Data, p1572.

5.4 Summary

To summarize, the growth of high purity and dense hexagonal aluminum nitride nanotips and nanorods on gold coated silicon substrates via a thermal chemical vapor deposition system has been demonstrated. A single growth parameter, namely the growth temperature, is able to dictate the formation of nanotips or nanorods in this vapor transport and condensation process. Optimal growth temperature for these nanotips and nanorods were 950°C and 1200°C, respectively. The AlN nanotips and nanorods grow by vapor solid mechanism and their preferred growth direction (long axis) is [001]. Composition and structures of the nanostructures have been confirmed by TEM, XRD, and Raman spectroscopy. A diffusion mediated growth model incorporating an Ehrlich-Schwoebel barrier and compressive stress at lower growth temperatures has been proposed to explain the formation of high aspect ratio nanotips with substantial microscopic and structural evidence.

Chapter 6

Luminescence of AlN nanotips

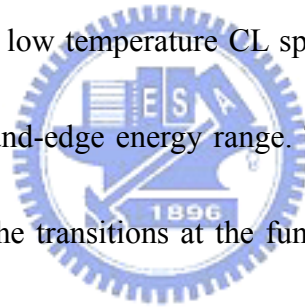
In recent times, wide band-gap III-nitrides have attracted considerable interest due to their outstanding thermal and chemical stability, leading to major advances for the devices which are active in the short-wavelength and capable of operation at high temperatures and in hostile environments [9]. Recently, the synthesis of one-dimensional nanostructured AlN opened potential applications in electronic/optic devices [177,178]. Therefore, understanding of electronic/ optic properties of AlN is of a great interest. Previous studies on the optical properties of AlN were well-documented. The near band-edge transition was investigated by using cathodoluminescence (CL) [179-181], photoluminescence (PL) [182,183], thermoluminescence (TL) [184,185], and optical reflectance [186] measurements on bulk as well as epi-AlN samples. Defect-related transitions were characterized in these systems as well [184,185,187-190]. Optically simulated luminescence measurements using visible or infra-red light and TL studies assisted with excitation spectral analysis showed that defect related emission peaks are due to radiative recombination process involved in complex formed due to oxygen related impurity (O_N) and aluminum vacancies (V_{Al}) [184,185].

Single crystalline, free-standing, nearly strain free and high quality nanostructures are preferred over thin film or bulk materials, since they serve as ideal systems for measurements of the fundamental properties of AlN [191]. However, there are only a few reports on the optical properties of nano-size AlN [192]. Therefore, it is useful to study and understand the luminescence features of AlN nano-structure. In this chapter, the optical properties nanostructures were studied by various optical techniques. Temperature dependent cathodoluminescence results are discussed in section 6.1. The photoluminescence and photoluminescence excitation properties were reported in section 6.2. Section 6.3 displays thermoluminescence and thermoluminescence excitation spectra. Absorption phenomenon was exhibited in the section 6.4. A luminescence model of AlN was proposed in section 6.5. Finally, section 6.6 will make a summary according to the obtained results.

6.1 Temperature dependent cathodoluminescence (CL)

Temperature-dependent CL studies (Fig. 6.1) showed two broad emission bands at 3.4 and 2.1 eV. The peak at 3.4 eV dominates the spectral range from 1.8 to 6.2 eV. This peak appears at the same wavelength as the well-known peak due to oxygen-related defects. According to Youngman *et al.*, [187,193] the dominant line (3.4 eV) was related to the defect created when oxygen substitutes for nitrogen in the

AlN lattice. Interestingly, the position of the oxygen related defects luminescence in AlN can vary from 3.3 to 4.0 eV as the concentration of oxygen content are changed. Based on M. Strassburg *et al.* [190], it was presumed that nitrogen vacancies and Al interstitial point defects are responsible for the 2.1 eV emission band. The CL spectra obtained from R. A. Youngman [193], where two peaks at 3.4 eV and 2.1 eV were evident suggesting that it is likely that our materials had the same level of oxygen content dissolved in the AlN lattice. The origin of these two peaks will be discussed in more detail subsequently, with the analysis of the midgap luminescence of AlNNTs. The inset in Fig. 6.1 shows a low temperature CL spectrum of AlNNTs measured at high resolution in the near-band-edge energy range. This short wavelength emission close to ~6 eV is related to the transitions at the fundamental absorption edge. This emission can be further deconvoluted into two peaks (inset, Fig. 6.1), centered at 6.07 and 6.20 eV, respectively, which are corresponding to the band edge splitting of AlN [194,195].



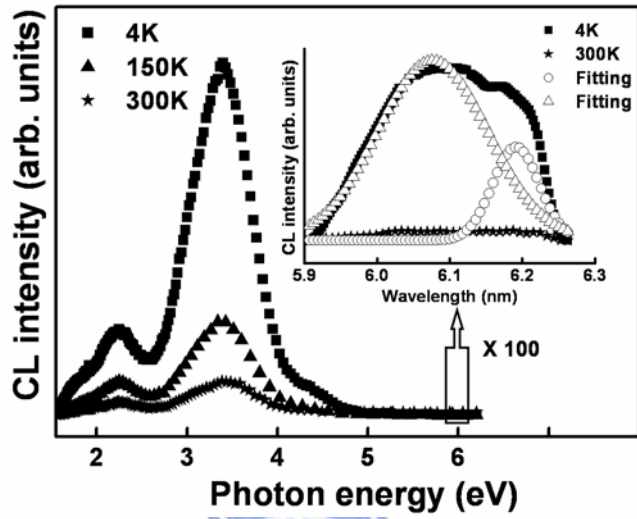


FIG. 6.1 Temperature-dependent CL spectra from AlNNTs grown on Si substrate measured between 4 to 300 K. The inset shows the near band edge transition which can be resolved into two peaks.

6.2 Photoluminescence (PL)

For further understanding of the light emission processes, the spectra were recorded by measuring the luminescence intensity of the nanotips as a function of excitation energy at selected detection energies. Figure 6.2 shows a typical PL spectra and PL excitation (PLE) spectra corresponding to the emission spectra (accumulated) obtained with different excitation wavelengths. The PL spectra show two broad emission bands centered at 3.2 (\blacktriangle), and 2.1 (\bullet) eV, respectively. PLE spectrum was taken by fixing the detector at energy of 2.1 eV, then varying the wavelength of excitation light. We found that the emission of 2.1 eV originated from the absorption of 3.4 eV light.

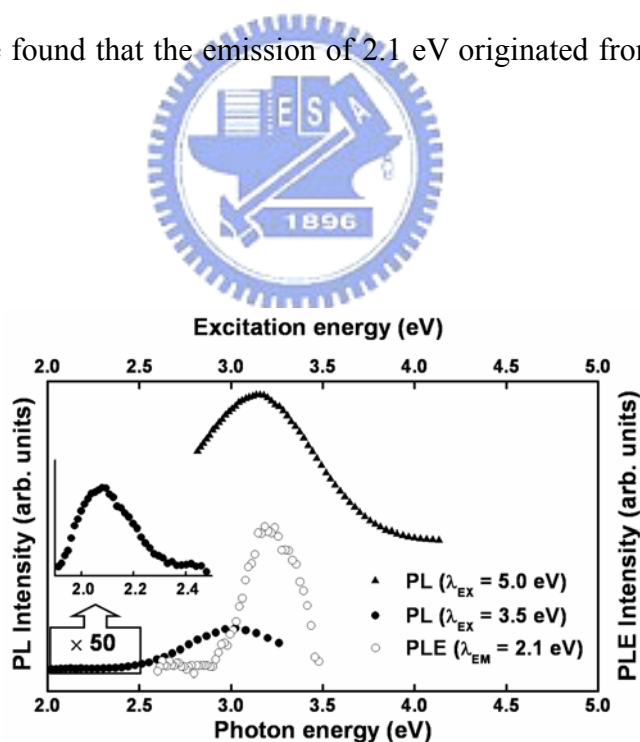
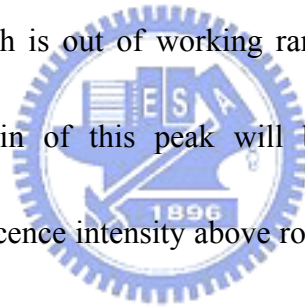


FIG. 6.2 PL and PLE spectrum of AlNNTs measured at room temperature. PL were taken from by the 5.0 (\blacktriangle), and 3.5 (\bullet) eV excitation, respectively. PLE were taken with the detection at 3.2 (\triangle), and 2.1 (\circ) eV.

6.3 Thermoluminescence (TL)

A broad emission ranging from 1.7 to 4.1 eV were observed in TL spectra (Fig 6.3) in the temperature range of 66-145°C with a pre-excitation of 6.0 eV. The observed spectra are in good agreement with the results of CL and PL, with defect peaks arising around 3.0 eV (slightly shifted to lower energy) and 2.1 eV. From the evidence of TL excitation (TLE), we understand that the source of emission around 3.0 eV is the near host-lattice absorption (~ 6.2 eV). Peak around 2.1 eV, however, is unaltered and no optical excitation could be made responsible for this emission, presumably due to the extremely low intensity which is out of working range of the detector in our TLE measurements. Possible origin of this peak will be discussed in the following paragraph. Sufficient luminescence intensity above room temperature in AlN, with its high resistance to radiation conditions, makes it a potential candidate as an UV detector applicable even at high temperature.



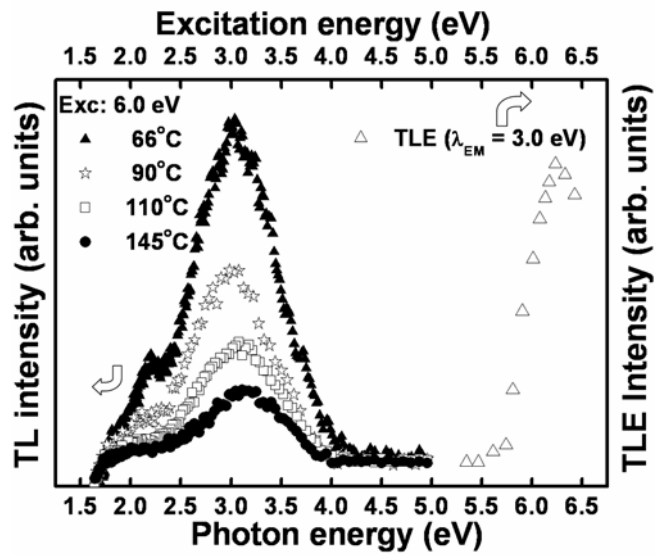


FIG. 6.3 TL spectrum of AlNNTs measured at different temperature between 66 to 145

°C with 206 nm excitation. TLE were observed at very near band edge.

6.4 UV Absorption

Further support of the CL, PL, and TL results comes from the UV absorption spectra (Fig. 6.4). We found three broad absorption peaks occurring in the process, centered at 3.4 eV, 4.5 eV, and 6.2 eV, respectively. Berzina *et al.* [196] have defined defect levels in AlN to be of three types: O_N - V_{Al} complex level at around 1.2 eV from valance band (VB), separated O_N ions level at around 4.6 eV from the VB, and a set of levels representing different electron traps. Slack *et al.*[197] have reported that oxygen incorporation in AlN proceeded by the substitution of oxygen on nitrogen sites (O_N) with the formation of attendant aluminum vacancies (V_{Al}) for charge compensation. A state related to O_N - V_{Al} complex formed inside the AlN band-gap with a probable excited state close to or overlapping (providing ionization to the excited centre) to conduction band. According to the energy scheme proposed by Berzina *et al.* [196], O_N - V_{Al} complex excited to the separated O_N ions level, O_N - V_{Al} complex level excited to near band edge, and band to band absorption are the source of the three broad absorption peaks centered at 3.4, 4.5, and 6.2 eV, respectively. Youngman *et al.* [193] has suggested that one possible origin of the peak broadness is due to the coulombic interaction between donor (O_N) and acceptor (V_{Al}) pairs. However, more detailed experiments, including time-resolved measurements, are necessary to clear this picture.

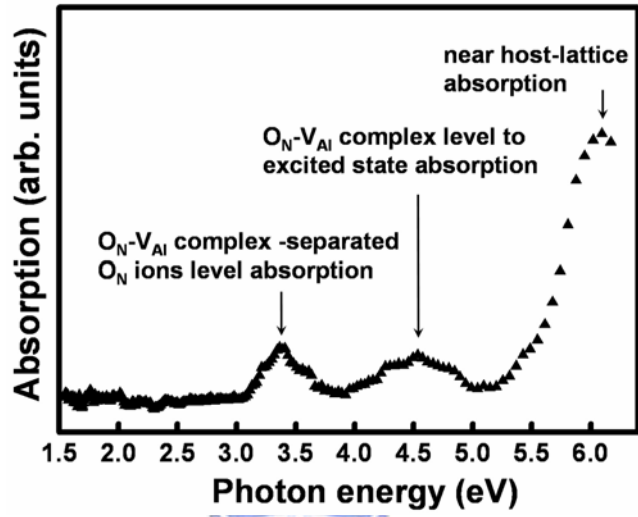


FIG. 6.4 UV absorption spectrum of AlNNTs showing major absorption process taking place.

6.5 Luminescence model

In brief, as shown in Fig. 6.5, absorption of a light quanta, $h\nu$ (~ 6.2 eV) owing to host lattice absorption [6.2 eV, as indicated in the TLE (Fig. 6.3), and UV absorption (Fig. 6.4) measurements]. Excitation of the O_N-V_{Al} complex level [4.0-5.0 eV, as indicated in UV absorption (Fig. 6.4) measurement] transforms the O_N-V_{Al} to an acceptor level and the excited electrons relaxes and gets trapped in the state created by separated O_N ions at 4.6 eV forming a donor state. The radiative recombination taking place between the donor and the acceptor states will emit a light of around 3.2 eV, as observed in CL (3.4 eV, Fig. 6.1), PL (Fig. 6.2) and TL (3.0 eV, Fig. 6.3) measurements. Simultaneously, another low energy emission ~ 2.1 eV, [CL (Fig. 6.1), PL (Fig. 6.2) and TL (Fig. 6.3) measurements] may occur due to some still unknown oxygen-related luminescence centers, which can be excited either in its own excitation bands, or reabsorbing the 3.4 eV emission as indicated in our PLE (Fig. 6.2) study. The electrons may also be released from the conduction band or released from the trap states during optical stimulation [185] or thermally by heat (TL) [184].

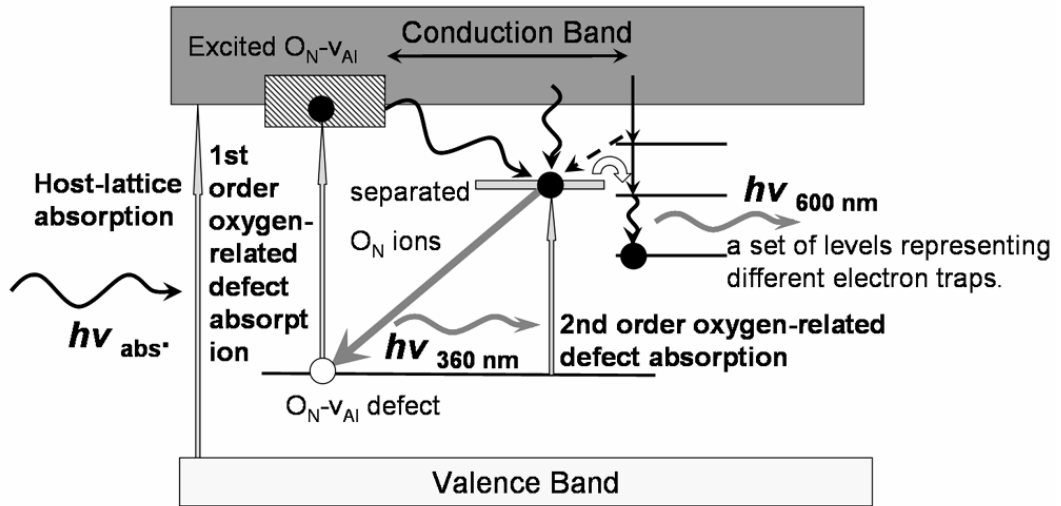


FIG. 6.5 Schematically drawing of luminescence model of AlN



6.6 Summary

A comprehensive description of luminescence properties for AlN nanotips is provided. Three prominent bands at 2.1, 3.4, and 6.2 eV were detected in CL, PL, and TL measurement. Excitation spectral analysis (PLE and TLE) combined with optical absorption measurements reveal that emission peaks at 2.1, 3.4, and 6.2 eV are due to O_N-V_{Al} complex excited to the separated O_N ions level absorption (3.4 eV), and host lattice absorption (6.2 eV), respectively. Finally, a complete illustration of luminescence model of AlN was presented.



Chapter 7

Surface enhanced Raman properties of AlN nanostructures

Surface enhanced Raman spectroscopy (SERS) has evolved as a powerful and sensitive tool for detection and identification of a wide range of adsorbate molecules down to the limit of single molecule detection [198-200]. Due to the low scattering cross section (10^{-30} cm²/molecule), Raman spectroscopy was much inferior to fluorescence spectroscopy, which had a larger cross section (10^{-16} cm²/molecule), for trace detection. Using specially prepared rough metallic surfaces the otherwise weak Raman signals can be enhanced by several orders making detection possible [201]. This enhancement can be as large as 10^{14} [198]. Hence, SERS has the capability to unite the sensitivity of fluorescence with the rich structural content inherent to Raman spectroscopy. This extraordinary enhancement is believed to be predominantly due to two mechanisms, a long range classical electromagnetic (EM) effect and a short range chemical effect [202]. The respective contributions of these mechanism to the overall SERS enhancement is debated but the EM effect is believed to be few orders more than that due to the chemical effect. Nie and Emory [198] showed that the commonly observed enhancement of the order of $\sim 10^6$ may have only been an ensemble average over several hundred nanoparticles, whereas a few of these SERS active metallic

particulates, called hot particles, can actually give an enhancement of about 10^{15} . At this level of enhancements SERS, with the richness of the molecular information, supercedes laser induced fluorescence experiments that carry molecular information only at low temperatures.

Even as we lack a complete quantitative understanding of the fundamentals of SERS, the progress in application developmental research has been remarkably fast and successful. Probing single molecules [203-205] or nanostructures [206,207], and development of nanoscale chemical sensors [208-209] utilizing SERS independently or in conjunction with liquid chromatography was made possible. The first step for achieving such advanced stages of application development was the fabrication of proper substrates which are SERS active and provide high enhancement factors. The first substrate on which SERS was observed was electrochemically roughened silver (Ag) electrode.⁴ Since then Ag films produced by Tollens reaction [210], or by vapor deposition methods [211,212] has been common place. Nitric acid etched Ag foils [213], or Ag photodeposited on anatase TiO₂ substrates [214] are also relatively easy to prepare. Self assembled Ag or Au colloid particles on polymer coated substrates and silver particles layered on to etched polymer substrates has also been used as SERS active substrates [211]. These substrates demonstrate enhancement factor of 10^3 - 10^6 which can be further enhanced by resonance effects. However, most of these


techniques, apart from photolithography [215], involve wet chemical etching and thus cannot be readily integrated into existing silicon device technologies. Achieving nanometer size metal prints is several years down the line even for lithographic techniques [215,216]. However, a special tip induced SERS aiding in nanoscale chemical analysis has been demonstrated which does not require a substrate fabrication [217]. SERS active substrate generation techniques compatible to silicon device technology is important since only then it can have a wider scope in applications such as micro electro mechanical systems (MEMS). In this chapter we report AlN nanostructured substrate on which silver nanoparticles, with less than 10 nm in diameter, can be self assembled at an extremely high density that readily exhibit the surface enhancement.



Having discussed the preparation and structure of AlN nanotips and nanorods, we now proceed to use them as template for nanocrystalline Ag (nc-Ag) generation. SERS have been mostly observed on metal colloids prepared by wet chemistry [218] which are often more efficient than roughened silver electrodes [201] used conventionally. The problem with colloids is however their instability resulting from agglomeration. But, very importantly, clean room compatible plasma processes are always preferred, over wet chemical means, to incorporate the metal nanocrystals in a sensing device. Noble metals, such as Ag, that demonstrate the best SERS, do form

rough island-like films when deposited on silicon. The SERS activity of the metal is enhanced in the nanophase when a high packing density [219] is attained. Use of a wide band gap template, such as AlN, for the nanoparticle support is essential to eliminate any background luminescence effect from the support and accentuate the Raman signals. AlN being chemically inert and immiscible to Ag will also preserve the purity and integrity of the nc-Ag and can be utilized in fabricating stable and reliable plasma engineered sensing devices.

7.1 Experimental



The AlN nanotips and nanorods were coated with silver by the ion beam sputtering (IBS) process. A base pressure of 1×10^{-6} Torr was achieved in the sputtering chamber that contained a high purity silver target, mounted on a rotating stage, and the AlN NTs and NRs substrates held about 10-15 cm away from the target. An argon (Ar) ion beam (Ar flow rate of 2 sccm) was accelerated toward the silver target using a Commonwealth Scientific (CS) IBS controller. The sputtered silver was collected on the substrate, kept at room temperature, for different durations of time. The working pressure was about 5×10^{-4} Torr.

Commonly used molecule for SERS experiment such as Rhodamine 6G was then dispersed by drop coating onto these substrates, in measured quantities, from its

solution and dried. They were then used for the Raman measurements using a Renishaw-2000 micro Raman spectroscope. Single accumulations with integration times of 5s were used to collect the spectra in a backscattered mode. A 532 nm laser with a source intensity of 100 mW was used with a probe beam diameter of 1 μm .

7.2 Results and discussion

Scanning electron microscope (SEM) images of the deposit reveal AlN nanorods to be sharply faceted quasi-aligned nanorods with a hexagonal cross-section. Figure 7.1a shows the SEM images of the as-grown AlN nanorods. Fig. 7.1b displays the SEM image of Ag-coated AlN nanorods. Fig. 7.1c shows the Ag-coated AlNNTs, and Fig. 7.1d exhibit the high magnification SEM image of Ag nanoparticles coated on AlN nanotips.

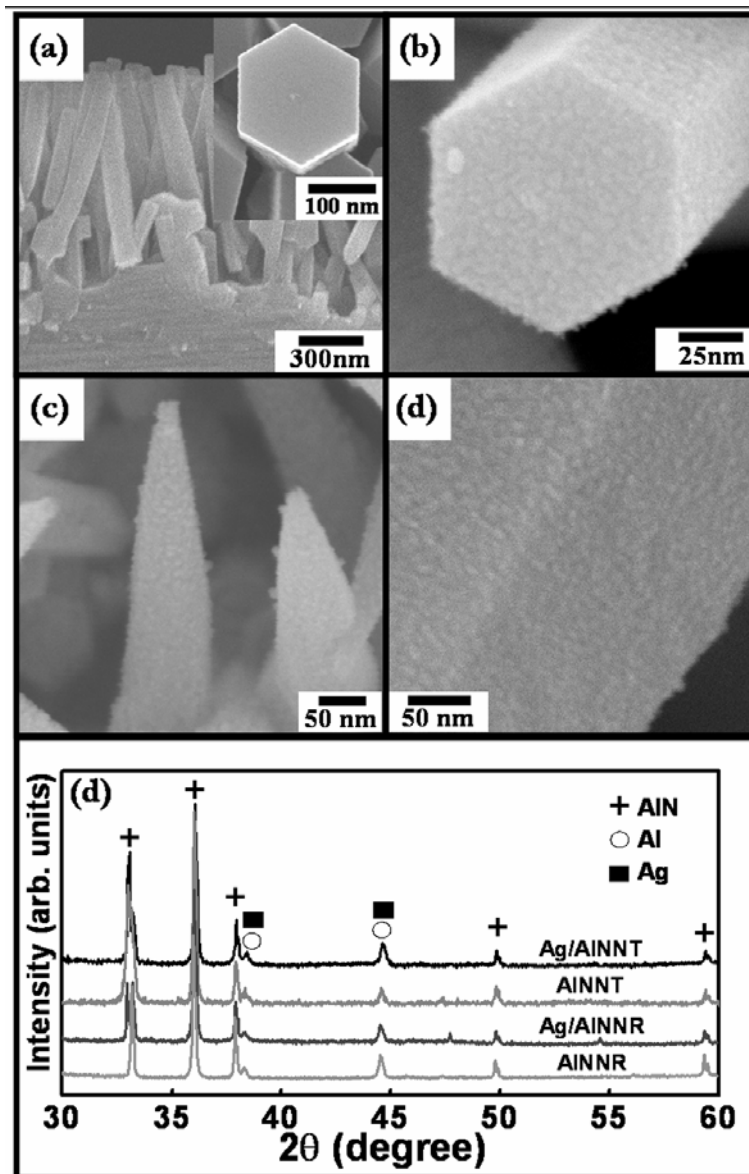
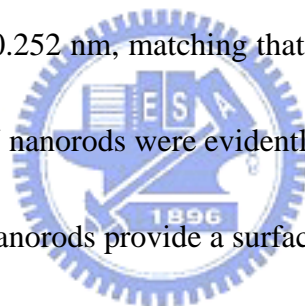


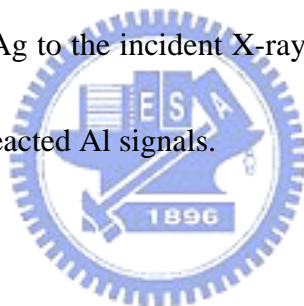
FIG. 7.1 (a) Cross section and top view (inset) SEM image of quasi aligned AlN nanorods; (b) Top view SEM image of Ag-coated AlN nanorod; (c) Cross section view of Ag-coated AlN nanotips; (d) High magnification SEM image of Ag-coated AlN nanotips; (e) X-ray diffraction spectrum of as-grown and Ag coated AlN nanostructures clearly shows a preferred orientation along [002] ($2\theta=36.04^\circ$).

The XRD spectra of the as-grown AlN nanotips and nanorods shows strong signatures of h-AlN phases ((100), (002) and (101)) (JCPDS 25-1133) along with unreacted pure Al (JCPDS 04-0787) residue. In addition to the XRD spectrum, the selected area electron diffraction (SAED) pattern (top inset, Fig. 7.2a), and electron energy loss spectroscopy (EELS) (bottom inset, Fig. 7.2a), carried out during the transmission electron microscopy (TEM) measurements conclusively prove that they are AlN in composition having hexagonal symmetry. Figure 7.2a shows a TEM image of an Ag-coated AlN nanorod. Figure 7.2b shows the lattice image of the as grown AlN nanorods with a $d_{(002)} = 0.252$ nm, matching that of h-AlN. The growth direction of the single crystalline h-AlN nanorods were evidently [002].



The h-AlN nanotips and nanorods provide a surface, with suitable interface energy and lattice mismatch that promotes the generation of nc-Ag, instead of a thin film, under an incident flux of Ag vapors in a sputtering chamber with specified deposition parameters. Argon ion beam sputtering [209] of a Ag target for 10 minutes under room temperature and 5×10^{-4} Torr pressure, used in this case, produced a single overcoat of nc-Ag on the entire surface of the h-AlN nanotips and nanorods. The sizes of the nc-Ag are mostly ~5 nm in diameter but not exceeding 10 nm, having an extremely high packing density such that they touch each other (Fig. 7.1b and 1d). Note that the packing density of the nc-Ag, per unit probe volume, is further enhanced

due to the rough nanostructured template compared to a flat template surface. Figure 7.2c shows the SAED pattern of the AlN nanorods with a post synthesis coating of sputtered Ag. Clear and sharp diffraction spots, which are signatures of h-AlN, were observed in the SAED pattern along with sharp ring patterns arising from nc-Ag (Fig. 7.2c). The sharp ring features present in the SAED pattern (Fig. 7.2c), but absent in Fig. 7.2a (top inset), confirms the presence of nc-Ag in the Ag coated samples. However, crystalline Ag signal cannot be detected unambiguously from the XRD spectrum of the Ag coated h-AlN nanostructures shown in Fig. 7.1c mainly due to a small cross-section of the nc-Ag to the incident X-rays and the close proximity of the Ag (JCPDS 03-0921) and unreacted Al signals.



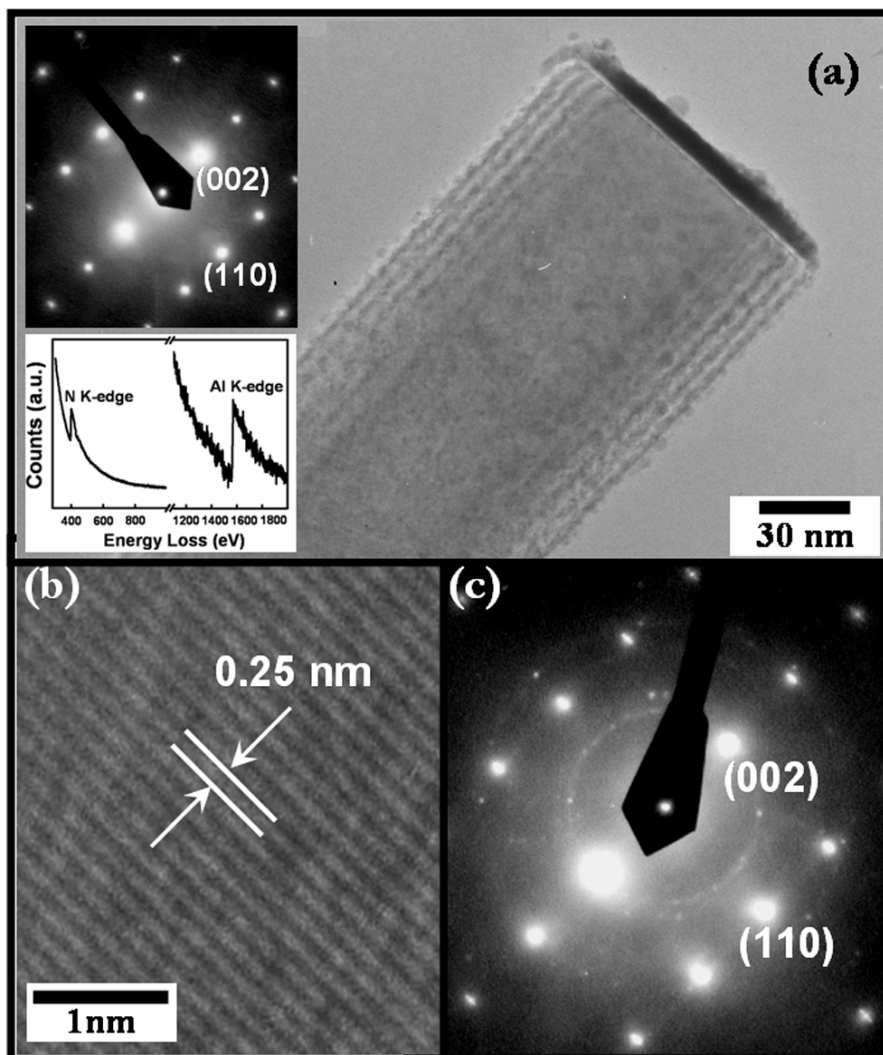
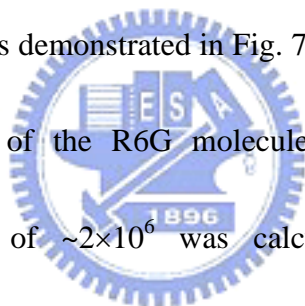


FIG. 7.2 (a) TEM image of a single Ag-coated AlN nanorod (the arrows showing the nc-Ag); top and bottom inset shows the SAED pattern and the electron energy loss spectroscopy (EELS) spectrum of the as-grown AlN nanorod, respectively; b) HRTEM image of the as-grown AlN nanorod lattice; c) SAED pattern of the Ag-coated AlN nanorod.

The Raman spectrum of the as-grown h-AlN nanostructures excited by a 532 nm laser is shown in Fig. 7.3a (AINNRs) and 3d (AINNTs). Measured quantities (2-5 μL) of micro-molar (10^{-6} M) solutions of Rhodamine 6G (R6G) in methanol when dropped on these as-grown h-AlN nanostructures show only a broad and strong fluorescence characteristic of R6G as shown in Fig. 7.3b (AINNRs) and 3e (AINNTs). The nc-Ag coated h-AlN nanorod surface demonstrates SERS of 10^{-6} M R6G solution. The generally fluorescent R6G molecule has its fluorescence quenched when adsorbed on the nc-Ag present on the h-AlN nanostructures template and the Raman signals are promoted as demonstrated in Fig. 7.3c (AINNRs) and 3f (AINNTs). Assuming 100% adsorption of the R6G molecules on the nc-Ag, a minimum enhancement in the range of $\sim 2 \times 10^6$ was calculated [220] for the Raman cross-section.



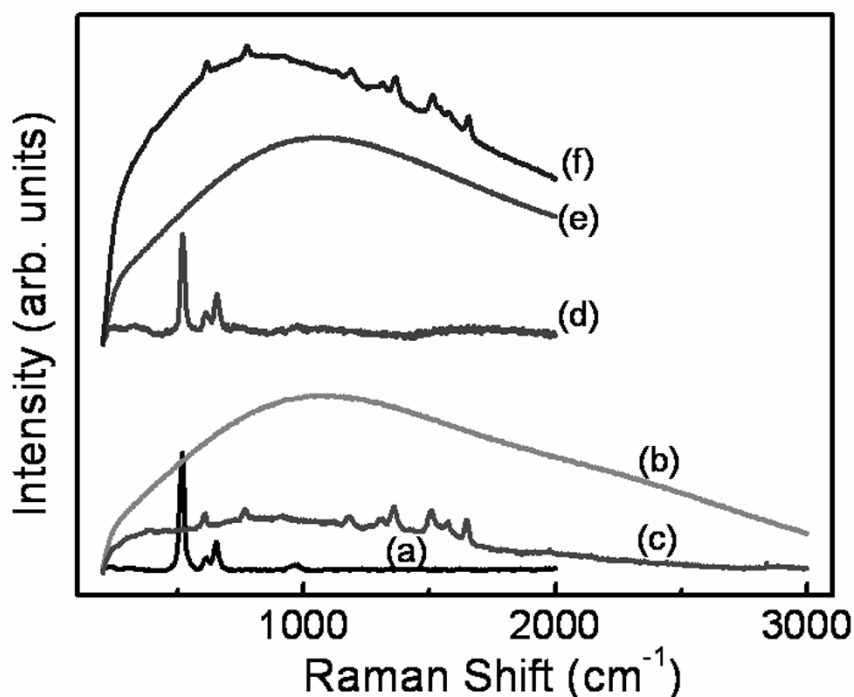


FIG 7.3 Raman spectrum of (a) the as-grown AlN nanorods, (b) as-grown AlN nanorods with R6G, and (c) SERS spectrum of Ag coated AlN nanorods with R6G, (d) as-grown AlN nanotips, (e) as-grown AlN nanotips with R6G, and (c) SERS spectrum of Ag coated AlN nanotips with R6G.

7.3 Summary

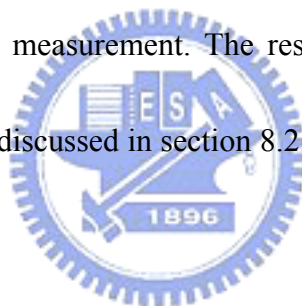
In final, we have demonstrated the synthesis of quasi-aligned h-AlN nanostructures from pure Al powders heated to 900 and 1200°C in presence of ammonia. Ion beam sputtered silver self-assembles as nanocrystals on these h-AlN nanostructures and readily exhibits surface enhanced Raman scattering. Minimum SERS cross-section enhancement factors in the range of 2×10^6 have been obtained.

Chapter 8

Field emission from quasi-aligned AINNTs

One-dimensional (1-D) nanostructures have recently brought significant research activities for its unique properties in different applications such as atomic-resolution scanning tunneling microscopy [221], near field optical microscopy [222], and high-resolution atomic force microscopy [223]. At the same time, wide band-gap materials have been promising as cold-cathode materials [224,225] due to their low electron affinities as well as their excellent thermal, chemical, and mechanical stability. Recently, the field emission characteristics of few 1-D wide bandgap semiconductors, such as well-aligned ZnO nanowires [226], SiC nanowires [227,228], SiCN nanorods [229], GaN nanowires [138], and diamond-like nanostructure [230], have been widely investigated and reported. Superior field emission performance can be achieved by adjusting the aspect ratio and spacing of the nanomaterials to optimize the enhancement of the local electric field at the emitting sites. It is clear that sharper tips give higher field enhancement factor which provides higher field emission current. One dimensional nanostructures including nanotips are interesting systems to investigate the field emission phenomenon [145,146,156]. The inherent current or voltage stressing of the nanostructures during the FE process however creates a

concern over the stability of the process and the nanostructures itself. Wide bandgap materials such as AlN may provide important clues or answers to this problem and that remains the focus of this report. According our previous observations, the hexagonal and faceted AlNNTs always reveal a sharp end with point tip. This geometrical feature and the intrinsically low electron affinity nature make AlNNTs an emitter material of potential. In this chapter, the field emission properties of the quasi-aligned AlNNTs grown on p^+ -, p-, n-, and n^+ - type Si substrates were studied. Section 8.1 will introduce the experimental section including the sample and parameters for field emission measurement. The results of geometrical feature and field emission of AlNNTs are discussed in section 8.2. Finally, section 8.3 will make a summary.



8.1. Experimental

The sample of AlNNTs and AlNNRs for field emission measurement were grown on gold coated p^+ -type Si (p^+ -Si) (resistivity ~ 2 -5 $m\Omega$ cm), p- (resistivity ~ 10 Ω cm), n- (resistivity ~ 10 Ω cm), and n^+ -Si (resistivity ~ 2 -5 $m\Omega$ cm) Si substrates, respectively via APCVD. Field emission measurements were carried out using parallel-plate configuration under a base pressure of $\sim 1 \times 10^{-7}$ Torr. The schematic drawing of FE is shown in Fig. 8.1. A Keithley 237 high voltage source-measure unit

was used for sourcing the voltage (up to 1100 V) and measuring the current (with pico-ampere sensitivity). The quasi-aligned AlN nanostructures served as the cathode and an indium tin oxide (ITO) coated glass was used as the anode for our FE measurement. The effective emission area is defined by the patterned ITO anode (emitting area 0.06 cm^2). The distance between these two electrodes could be controlled, and kept at $70 \text{ }\mu\text{m}$.

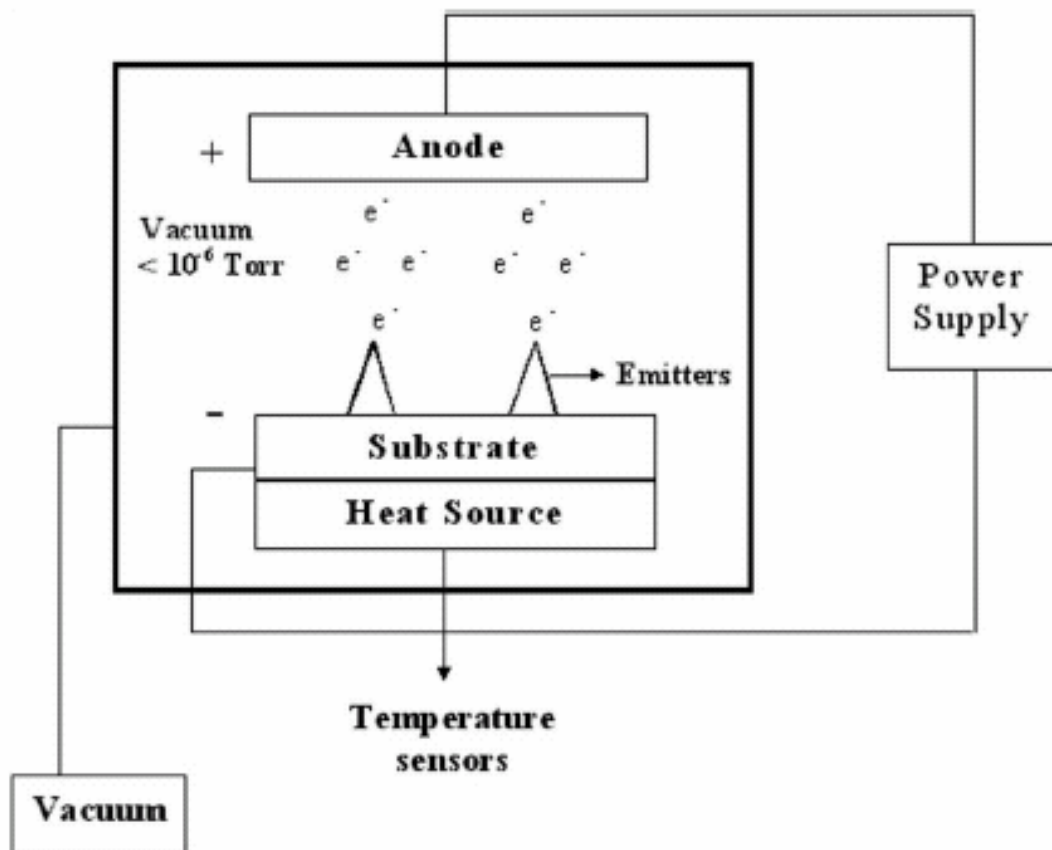
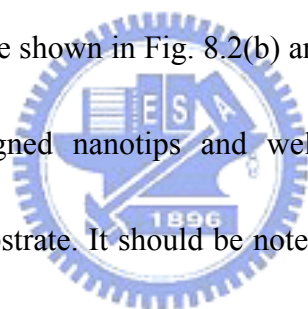


FIG. 8.1 Schematic diagram of field emission measurement [231].

8.2. Results and discussion

Figure 8.2 a-b display the field emission scanning electron microscope image of the AlN nanotips grown on p⁺-type Si (p⁺-Si) substrate, and AlN nanorod grown on n⁺-type Si (p⁺-Si) substrate (Fig. 8.2 c-d). All AlN nanostructures prepared on differently doped Si substrates have very similar morphologies to each other. It was found that AlN nanostructures could be successfully synthesized depending only on the growth parameters, such as temperature, reaction time and gas flow rate but independent of the dopants in the Si substrate. Typical cross-sectional SEM image of AlN nanotips and nanorods are shown in Fig. 8.2(b) and (d). This photograph displays a high density of quasi-aligned nanotips and well aligned nanorods uniformly distributed over the entire substrate. It should be noted that all the nanotips exhibited the same self-selective apex angle, indicating the formation of nanotips was subjected to a surface energy controlled process [166].



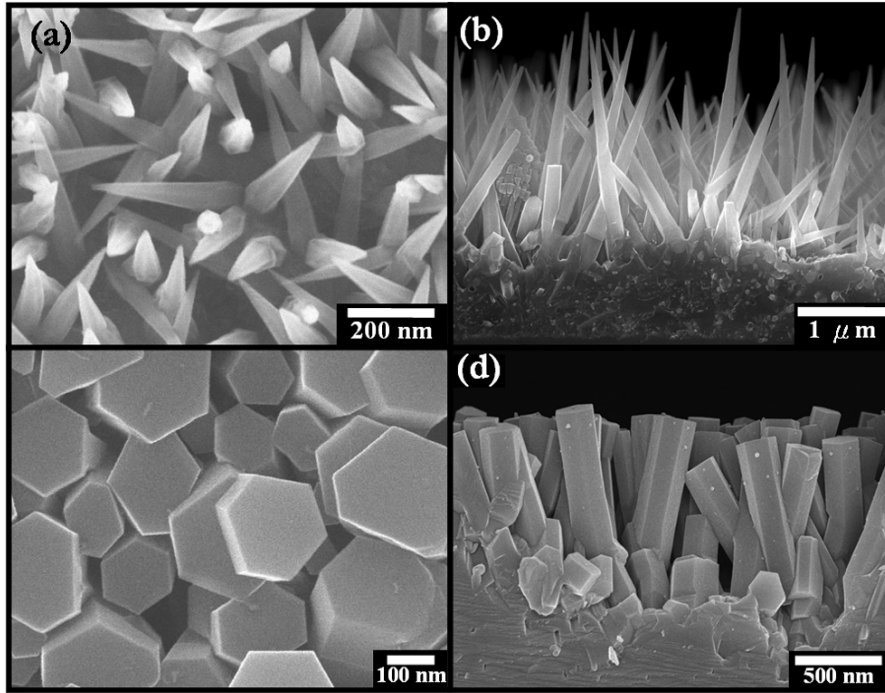
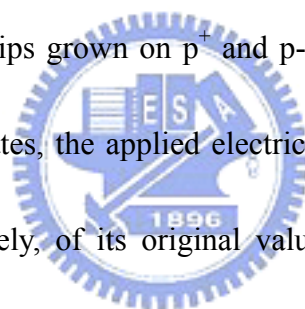


FIG. 8.2 Typical FESEM (a) top view, (b) cross section images of AlN nanotips ; (c) top view, (d) cross section images of AlN nanorods grown on p⁺-Si substrate.

The typical field emission current density (J), which is defined as the current collected per unit area of the anode, vs. applied field (E) characteristic of AlNNTs and AlNNRs is depicted in Fig. 8.3. The quasi-aligned AlN nanotips served as the cathode and an indium tin oxide coated glass was used as the anode for our FE measurement. The anode area is approximately around 0.25 cm^2 . The anode-cathode distance was kept at $70 \mu\text{m}$. If a turn-on field (V_{on}) for field emission is defined as the field required in extracting a current density of $10 \mu\text{A}/\text{cm}^2$ [232] then V_{on} for samples grown on p^+ (resistivity $\sim 2\text{-}5 \text{ m}\Omega \text{ cm}$) and p type (resistivity $\sim 10 \Omega \text{ cm}$) Si substrates were 6.0 and $8.5 \text{ V}/\mu\text{m}$, respectively. In contrast, it is difficult to obtain any field emission current of the AlN nanotips grown on n^- (resistivity $\sim 10 \Omega \text{ cm}$) and n^+ -Si (resistivity $\sim 2\text{-}5 \text{ m}\Omega \text{ cm}$) substrates as well as the AlNNRs grown on p^+ -Si. No emission current observed from AlNNRs may be due to the surface field declining attributed to high density of nanorods and flat surface. Emission currents higher than $0.22 \text{ A}/\text{cm}^2$ are observed on the case of AlNNTs grown on p^+ -Si while the applied field exceeds $10 \text{ V}/\mu\text{m}$. The obtained turn-on field of $6.0 \text{ V}/\mu\text{m}$ is comparable to the lowest E_{to} values reported so far for CNTs ($0.6 - 2.8 \text{ V}/\mu\text{m}$) [232-234], N-doped diamond film ($\sim 1.5 \text{ V}/\mu\text{m}$) [235] and amorphous carbon film ($6.0 \text{ V}/\mu\text{m}$) [236]. According to the F-N plot (see the inset), a linear relation between $\ln(J/E^2)$ and $1/E$ is observed, indicating that the field emission is intrinsically driven by the electric field. The reproducibility of

the FE properties was verified for the AlN nanotips grown on p⁺- and p-Si substrates by performing repeated cycles of measurements and is shown in Fig. 8.3(b). For practical application as an emitter material in flat panel display, emission current stability of AlNNTs has been tested under high vacuum conditions for extended periods of time. The stability study was done by extracting a constant current density of 100 $\mu\text{A}/\text{cm}^2$, which is 10 times larger than the minimal FED operation current of 10 $\mu\text{A}/\text{cm}^2$, continuously over a period of 10 hours and monitoring the flat plate electric field required for the purpose. Figure 8.3(b) demonstrates the stability of electron emission from the AlN nanotips grown on p⁺ and p-Si substrates. For AlN nanotips grown on p⁺ and p-Si substrates, the applied electric field varied by only about less than 5% and 10%, respectively, of its original value to maintain the 100 $\mu\text{A}/\text{cm}^2$ current density, it is manifesting the highly durable and robust capability of the AlNNTs. An acceptable stability of the quasi-aligned AlN nanotips was demonstrated. However, the instability in the applied field at 4 hrs into the experiment probably indicates some damage, under such high current extraction (current stressing), in the substrate-nanotip interfacial area resulting in a reduced density of the emitters. The reduced density of the nanotips can reduce the effective field screening at the tips and bring down the required field for a specific current extraction.



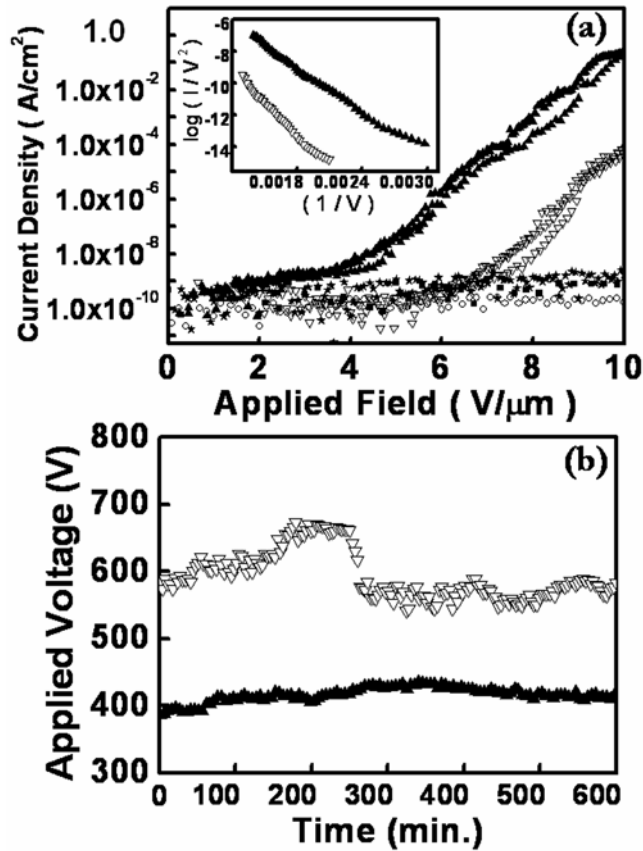


FIG. 8.3 (a) Field emission characteristic curves for quasi-aligned AlN nanotips emitter (emitting area 0.06 cm²) grown on (▲) p⁺-type Si, (▽) p-type Si, (■) n⁺-type Si and (○) n-type Si, respectively. (★) is the AlNNRs grown on p⁺-type Si. Inset shows the F-N plot for field emission of the AlN nanotips grown on (▲) p⁺ and (▽) p-type Si; (b) Emission stability of AlN nanotips grown on (▲) p⁺ and (▽) p-type Si substrates, where the emission current was kept at a constant value of 100μA/cm².

Field emission mechanism from supported nanostructures should consider electron injections from the two interfaces namely the substrate-emitter interface and the emitter-vacuum interface. Whereas the emitter-vacuum interface is widely studied and reported, the substrate-emitter interface was rarely studied. In 1996, a simplified electron emission model, proposed by Choi et al. [237], on a metal-diamond-vacuum system, which considered tunneling of electrons through the Mo-diamond Schottky barrier into the conduction band by applying an electric field. A similar model was proposed by Geis et al [238]. Furthermore, Snow et al. [239], proposed the model of electron emission mechanism based on transport across both interfaces, one is substrate-diamond interface, and the other is diamond-vacuum interface. It has been reported that the emission performance of diamond is often limited by the injection of electrons into the diamond through the metal-diamond interface. Therefore, the quantity of electrons injected from the substrate to the wide bandgap material is the determining step for the field emission of the wide bandgap materials.

To explain the electron transport phenomenon across the substrate-emitter interface, we revert to semiconductor heterojunctions. The analogy of the present system, AlN on Si, with that of a semiconductor heterojunction is valid owing to the large difference in their bandgaps and resistivities. The AlN material has a high electrical resistivity and wide bandgap (6.2 eV) [240] in comparison to the low electrical

resistivity and low bandgap (1.1 eV) of the Si substrates. The work function for AlN was found to be 4.3 eV [241] whereas that for n-type Si is ~ 4.15 eV from an independent ab-initio calculation [242]. The electron affinity (χ) of wide bandgap AlN is 0.6 eV [241] and less than that of the low bandgap Si ($\chi = 4.01$ eV) [242]. Hence for Si-AlN junction, a “straddled” heterojunction was obtained wherein the bandgap of the AlN completely overlaps the bandgap of Si. After Si and AlN forms a junction and thermal equilibrium is established, band bending occurs at the interface (Fig. 8.4). Due to a very large separation in the Fermi levels of n-type Si (E_{FN}) and AlN (E_F) a large number of electrons flow into AlN for Fermi level alignment across a Si (n-type)-AlN junction. This will bring about a severe band bending at the interface and a higher barrier for further electron movement from Si to AlN. On the other hand, for Si (p-type)-AlN heterojunction, the Fermi level in Si (E_{FP}) is slightly lower than that in AlN (E_F), causing a flow of holes from p-type Si to AlN to obtain Fermi level alignment. Therefore, the band bending at the Si(p-type)-AlN interface results in a “well”, instead of a barrier, allowing an easier electron flow across this junction under an applied field. This effect will be more pronounced for a p^+ -type Si-AlN interface since an even narrower separation exist between the E_{FP} and E_F and will lead to a more efficient electron tunneling into AlN. Therefore, AlN nanotips grown on p-type and p^+ -type substrates have higher emission currents than those grown on n-type and



n^+ -type Si substrates. This phenomenon is very similar to that of the field emission properties of one dimensional wide bandgap SiCN nanostructure where no gold catalyst was used [243]. The field emission results we obtained on differently doped substrates were not dominated by any possible gold doping which, if present, would have been identical for all the samples. The contrasting field emission results can only result from the donor/acceptor doping in the substrates which was the only distinguishing factor for the samples studied.



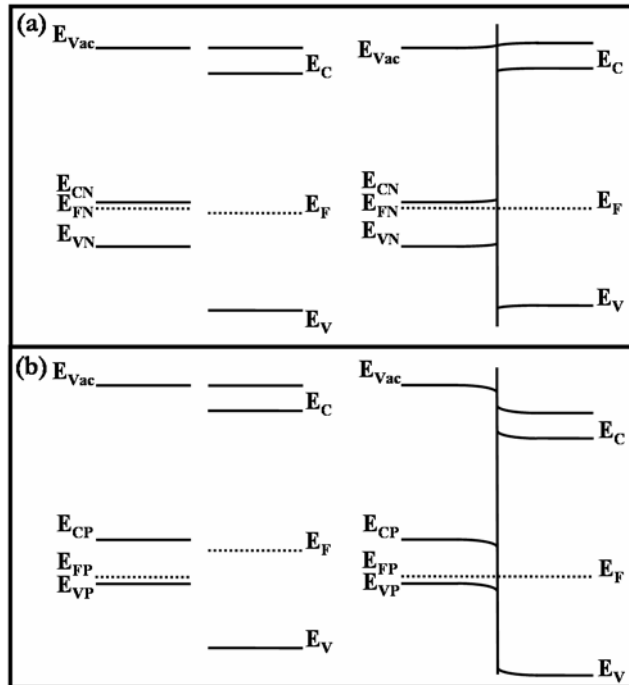
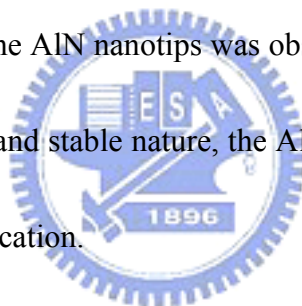


FIG. 8.4 Representative band diagram for (a) Si (n-type)-AlN and (b) Si (p-type)-AlN heterojunctions, before and after thermal equilibration. E_C , E_V , E_F stands for the conduction band, valence band and Fermi level, respectively, of AlN. E_{CN} , E_{VN} , E_{FN} stands for the conduction band, valence band and Fermi level, respectively, of n-type Si and E_{CP} , E_{VP} , E_{FP} stands for the conduction band, valence band and Fermi level, respectively, of p-type Si.

8.3 Summary

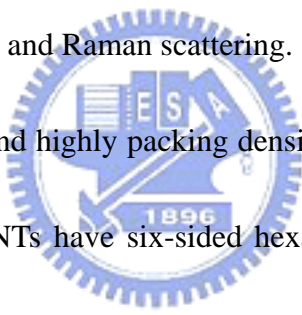
In final, FE properties of AlN nanotips and nanorods were studied. The effect of the p- and n-Si substrates in enhancing or limiting the field emission from the Si-AlN interface was demonstrated. The results of improved field emission of AlN on p⁺- and p-Si substrates were explained based on band diagram considerations in semiconductor heterojunctions. The existence of an energy barrier at the interface of n-/n⁺-type Si and AlN attenuated the electron flow whereas the absence of the same eliminated any threshold for electron flow across the p-/p⁺-type Si and AlN interface. A stable field emission from the AlN nanotips was observed over a period of 10 hours. Due to the nanosize structure and stable nature, the AlN nanotips show great potential for field emission device application.



Chapter 9

Conclusion

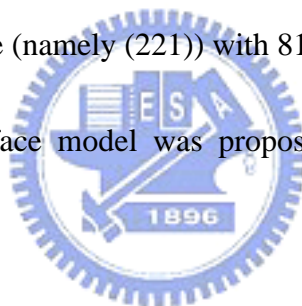
Via the technique of horizontal-flow hot-wall atmosphere pressure chemical vapor deposition (APCVD) using highly pure aluminum and ammonia gas as the CVD precursor, conductive AlN 1D nanocrystals, including NTs and NRs. A detailed characterization focusing on the morphology, structures, orientations and compositions of the various AlN samples have been carried out by means of FESEM, HRTEM, SAED, EELS, XRD, and Raman scattering.



The vertical quail-aligned and highly packing density AlNNTs are prepared via the APCVD technique. The AlNNTs have six-sided hexagonal geometry and sharp tip. The effects of variety types and thickness of metal coating on the morphology and size have been observed via FE-SEM. The size of AlNNTs can be controlled by adjusting the thickness of the Au layer. For deposition on thin (7 nm) Au-coated Si substrate, AlNNTs exhibited a mean diameter of 10 nm at the apex, 80 nm at the base, and 250 nm in length whereas NTs deposited at thicker Au layers (15-50 nm) produced longer nanotips (300-3000 nm) with wider apex (20-100 nm) and base (100-700 nm) diameters. Furthermore, AlNNTs can be prepared on Al and Pt coated substrates, even on bare Si (without metal coating). It indicated that metal coating is

not indispensable for the growth, but it does help in controlling the morphology of the AlNNTs. The Al nanocrystals nucleated within the first 20 minutes of growth and served as the base for the AlNNTs formation. AlNNTs start to germinate at the first 25 minutes of the growth and complete formation in 25-30 minutes. TEM and SAD measurements indicate that these hexagon tips have their long-axis along [002] direction. XRD patterns show that AlNNTs exhibit hexagonal crystal symmetry with a preferred growth direction of (002). The growth mechanism of AlNNTs is supposed to be different from ordinary vapor-liquid-solid or catalyst-mediated growth mechanisms.

AlNNTs possess a stable plane (namely (221)) with 81° angle with respect to the basal plane. The “*nongrowth*” surface model was proposed to be the main mechanism leading to the tip formation.



By designing a series of APCVD experiments, a morphological evolution from tip-like AlN to rod-like NRs has been observed as increasing the reaction temperature from 950 to 1200°C. The structural characterization by TEM, SAED and XRD shows the single-crystalline quality and an identical preferred *c*-axis growth direction for the AlN NTs and NRs. The diffusion mediated growth model incorporating an Ehrlich-Schwoebel barrier was proposed to explain the formation of high aspect ratio nanotips and nanorods.

Near-band edge peak (~6.2 eV) and defect luminescence (~3.4, 2.1 eV) were

observed in optical properties measurements. Spontaneous absorption from host-lattice and a series of oxygen-related defect levels were obtained from excitation spectra and UV absorption technique. Luminescence model was adapted to describe the luminescence features of AlNNTs.

The use of AlN nanostructures as nano-templates for SERS experiments were carried out by Ag coating. Nc-Ag particles are well dispersed on the h-AlN nanotips and nanorods with the mean diameter of 5-10 nm, exhibiting minimum SERS cross-section enhancement factors in the range of 2×10^6 .

The field emission performance of the quail-aligned AlNNTs has been studied in detail. TEM micrograph shows that the AlNNTs have a geometrical feature of self-assembled sharp tip with high aspect ratio, which is helpful in increasing field enhancement. The *J-E* measurement yields a low turn-on field at 6.0 V/ μm for AlNNTs, which is comparable to that of CNT, N-doped diamond film, and amorphous carbon film. After operating at $J = 100 \mu\text{A}/\text{cm}^2$ for over a period of 10 h, the long-term stability of durable and robust AlNNTs is demonstrated. Our results indicate that AlNNTs would be particularly suitable for use as field emitters, due to several advantages including nanometer structure, self-assembled sharp tips, and stable long-term emission ability. The Si-AlN heterojunctions model was proposed to explain the improved field emission of AlN on p^+ - and p-Si substrates.

Reference

1. M. A. Kastner, *Phys. Today* 46 (1993) 24.
2. R. F. Davis, *Proc. IEEE* 75 (1991) 702.
3. L. N. Lewis, *Chem. Rev.* 93 (1993) 2693.
4. Y. Cui, Q. Q. Wei, H. K. Park, C. M. Lieber, *Science* 293 (2001) 1289.
5. J. F. Smyth, *Science* 258 (1992) 414.
6. L. J. Lauhon, *Nature* 420 (2002) 57.
7. A. P. Alivisatos, *Science* 271 (1996) 933.
8. S. Iijima, *Nature* 354 (1991) 56.
9. H. Morkoc, S. Strite, G. B. Gao, M. E. Lin, B. Sverdlov, M. Burns, *J. Appl. Phys.* 76 (1994) 1363.
10. S. S. Kocha, M. W. Peterson, D. J. Arent, J. M. Redwing, M. A. Tischler, J. A. Turner, *J. Electrochem. Soc.* 142 (1995) L238.
11. E. N. Matthias, B. M. Allen, *IEEE Trans. Electron Devices* ED-34 (1987) 257.
12. A. Yamamoto, M. Tsujino, M. Ohkubo, A. Hashimoto, *Sol. Energy Mater. Sol. Cells* 35 (1994) 53.
13. W. M. Yim, E. J. Stofko, P. J. Zanzucchi, J. I. Pankove, M. Ettenberg, S. L. Gilbert, *J. Appl. Phys.* 44 (1973) 292.
14. Y. Fujii, S. Yoshida, S. Misawa, S. Maekawa, T. Sakudo, *Appl. Phys. Lett.* 31 (1977) 815.
15. G. R. Kline, K. M. Lakin, *Proc. IEEE Symp. Ultrasonics* 14 (1983) 495.
16. K. Tsubouchi, K. Sugai, *Mikoshiba Proc. IEEE Symp. Ultrasonics* 14 (1983) 340.
17. M. G. Norton, B. C. H. Steele, C. A. Leach, *Science of Ceramics* 14 (1988) 545.
18. G. A. Cox, D. O. Cummins, K. Kawabe, T. Tredgold, *J. Phys. Chem. Solids* 28 (1967) 543.
19. L. Cartz, F. G. Karioris, R. A. Fournelle, *Rad. Effects* 54 (1981) 57.

20. N. Kuramoto, H. Taniguchi, I. Aso, *Am. Ceram. Soc. Bull.* 68 (1989) 883.
21. M. A. Reed, *Sci. Am.* (1993) 118.
22. K. K. Likharev, T. Claeson, *Sci. Am.* (1992) 80.
23. V. Vijayakrishnan, A. Chainani, D. D. Sarma, C. N. R. Rao, *J. Phys. Chem.* 96 (1992) 8679.
24. B. C. Satishkumar, A. Govindaraj, K. R. Harikumar, J. P. Zhang, A. K. Cheetham, C. N. R. Rao, *Chem. Phys. Lett.* 300 (1999) 473.
25. O. Stephan, P. M. Ajayan, C. Colliex, Ph. Redlich; J. M. Lambert, P. Bernier, P. Lefin, *Science* 266 (1994) 1683.
26. R. Tenne, L. Margulis, M. Genut, G. Hodes, *Nature* 360 (1992) 444.
27. M. Brorson, T. W. Hansen, C. J. H. Jacobsen, *J. Am. Chem. Soc.* 124 (2002) 11582.
28. Y. Feldman, E. Wasserman, D. J. Srolovitz, R. Tenne, *Science* 267 (1995) 222.
29. M. Remskar, A. Mrzel, Z. Skraba, A. Jesih, M. Ceh, J. Demsar, P. Stadelmann, F. Levy, D. Mihailovic, *Science* 292 (2001) 479.
30. M. Nath, C. N. R. Rao, *J. Am. Chem. Soc.* 123 (2001) 4841.
31. M. Nath, C. N. R. Rao, *Chem. Commun.* (2001) 2236.
32. M. H. Huang, S. Mao, H. Feick, H. Yan, Y. Wu, H. Kind, E. Weber, R. Russo, Y. Yang, *Science* 292 (2001) 1897.
33. J. J. Wu, S. C. Liu, *Adv. Mater.* 14 (2002) 215.
34. X. Y. Kong, Z. L. Wang, *Appl. Phys. Lett.* 84 (2004) 975.
35. C. Ronning, P. X. Gao, Y. Ding, Z. L. Wang, D. Schwen, *Appl. Phys. Lett.* 84 (2004) 783.
36. W. I. Park, C. C. Yi, M. Kim, S. J. Pennycook, *Adv. Mater.* 14 (2002) 1841.
37. Y. C. Kong, D. P. Yu, B. Zhang, W. Fang, S. Q. Feng, *Appl. Phys. Lett.* 78 (2001) 407.

38. M. E. Spahr, P. Bitterli, R. Nesper, M. Muller, F. Krumeich, H. U. Nissen, *Angew. Chem. Int. Ed.* 37 (1998) 1263.
39. H. J. Muhr, F. Krumeich, U. P. Schonholzer, F. Bieri, M. Niederberger, L. J. Gauckler, R. Nesper, *Adv. Mater.* 12 (2000) 231.
40. F. Krumeich, H. J. Muhr, M. Niederberger, F. Bieri, B. Schnyder, R. Nesper, *J. Am. Chem. Soc.* 121 (1999) 8324.
41. A. Doble, K. Ngala, S. Yang, P. Y. Zavalij, M. S. Whittingham, *Chem. Mater.* 13 (2001) 4382.
42. K. S. Pillai, F. Krumeich, H. J. Muhr, M. Niederberger, R. Nesper, *Solid State Ionics* 141/142 (2001) 185.
43. M. E. Spahr, P. Stoschitzki-Bitterli, R. Nesper, O. Haas, P. Novak, *J. Electrochem. Soc.* 146 (1999) 2780.
44. T. Kasuga, M. Hiramatsu, A. Hoson, T. Sekino, K. Niihara, *Langmuir* 14 (1998) 3160.
45. H. Imai, Y. Takei, K. Shimizu, M. Matsuda, H. Hirashima, *J. Mater. Chem.* 9 (1999) 2971.
46. T. Kasuga, M. Hiramatsu, A. Hoson, T. Sekino, K. Niihara, *Adv. Mater.* 11 (1999) 1307.
47. S. Kobayashi, K. Hanabusa, N. Hamasaki, M. Kimura, H. Shirai, *Chem. Mater.* 12 (2000) 1523.
48. G. H. Du, Q. Chen, R. C. Che, Z. Y. Yuan, L. M. Peng, *Appl. Phys. Lett.* 79 (2001) 3702.
49. D. Gong, C. A. Grimes, O. K. Varghese, W. Hu, R. S. Singh, Z. Chen, E. C. Dickey, *J. Mater. Res.* 16 (2001) 3331.
50. R. A. Caruso, J. H. Schattka, A. Greiner, *Adv. Mater.* 13 (2001) 1577.
51. S. M. Liu, L. M. Gan, L. H. Liu, W. D. Zhang, H. C. Zeng, *Chem. Mater.* 14 (2002)

1391.

52. J. Hong, J. Cao, J. Sun, H. Li, H. Chen, M. Wang, Chem. Phys. Lett. 380 (2003) 366.

53. Y. F. Chen, C. Y. Lee, M. Y. Yeng, H. T. Chiu, Mater. Chem. Phys. 81 (2003) 39.

54. P. Hoyer, Langmuir 12 (1996) 1411.

55. J. Polleux, N. Pinna, M. Antonietti, M. Niederberger, Adv. Mater. 16 (2004) 436.

56. Z. R. Dai, J. L. Gole, J. D. Stout, Z. L. Wang, J. Phys. Chem. B 106 (2002) 1274.

57. Y. Liu, J. Dong, M. Liu, Adv. Mater. 16 (2004) 353.

58. Z. R. Dai, Z. W. Pan, Z. L. Wang, Solid State Commun. 118 (2001) 351.

59. Y. Liu, C. Zheng, W. Wang, C. Yin, G. Wang, Adv. Mater. 13 (2001) 1883.

60. D. F. Zhang, L. D. Sun, J. L. Yin, C. H. Yan, Adv. Mater. 15 (2003) 1022.

61. Y. Chen, X. Cui, K. Zhang, D. Pan, S. Zhang, B. Wang, J. G. Hou, Chem. Phys. Lett. 369 (2003) 16.

62. Z. G. Bai, D. P. Yu, H. Z. Zhang, Y. Ding, Y. P. Wang, X. Z. Gai, Q. L. Hang, G. C. Xiong, S. Q. Feng, Chem. Phys. Lett. 303 (1999) 311.

63. Y. J. Zhang, J. Zhu, Q. Zhang, Y. Yan, N. Wang, X. Zhang, Chem. Phys. Lett. 317 (2000) 504.

64. C. N. R. Rao, B. C. Satishkumar, A. Govindaraj, Chem. Commun. (1997) 1581.

65. Y. Li, Y. Bando, D. Golberg, Adv. Mater. 16 (2004) 37.

66. B. C. Satishkumar, A. Govindaraj, E. M. Vogl, L. Basumallick, C. N. R. Rao, J. Mater. Res. 12 (1997) 604.

67. Y. Q. Zhu, W. B. Hu, W. K. Hsu, M. Terrones, N. Grobert, J. P. Hare, H. W. Kroto, D. R. M. Walton, H. Terrones, J. Mater. Chem. 9 (1999) 3173.

68. J. Hwang B. Min, J. S. Lee, K. Keem, K. Cho, M. Y. Sung, M. S. Lee, S. Kim, Adv. Mater. 16 (2004) 422.

69. Z. H. Yuan, H. Huang, S. Fan, Adv. Mater. 14 (2002) 303.

70. Y. Li, Y. Bando, D. Golberg, *Adv. Mater.* 15 (2003) 581.
71. J. Lao, J. Huang, D. Wang, Z. Ren, *Adv. Mater.* 16 (2004) 65.
72. H. Z. Zhang, Y. C. Kong, Y. Z. Wang, X. Du, Z. G. Bai, J. J. Wang, D. P. Yu, Y. Ding, Q. L. Hang, S. Q. Feng, *Solid State Commun.* 109 (1999) 677.
73. Y. C. Choi, W. S. Kim, Y. S. Park, S. M. Lee, D. J. Bae, Y. H. Lee, G. S. Park, W. B. Choi, N. S. Lee, J. M. Kim, *Adv. Mater.* 12 (2000) 746.
74. B. Y. Geng, L. Zhang, G. Meng, T. Xie, X. Peng, Y. Lin, *J. Cryst. Growth* 259 (2003) 291.
75. K. W. Chang, J. J. Wu, *Adv. Mater.* 16 (2004) 545.
76. Q. Tang, Z. Liu, S. Li, S. Zhang, X. Liu, Y. Qian, *J. Cryst. Growth* 259 (2003) 208.
77. J. Wang, Q. Chen, C. Zeng, B. Hou, *Adv. Mater.* 16 (2004) 137.
78. Y. Li, Y. Bando, D. Golberg, *Adv. Mater.* 15 (2003) 1294.
79. R. S. Chen, Y. S. Chen, Y. S. Huang, Y. L. Chen, Y. Chi, C. S. Liu, K. K. Tiong, A. J. Carty, *Chem. Vap. Deposition* 9 (2003) 301.
80. R. S. Chen, Y. S. Huang, Y. M. Liang, D. S. Tsai, Y. Chi, J. J. Kai, *J. Mater. Chem.* 13 (2003) 2525.
81. R. S. Chen, Y. S. Huang, Y. M. Liang, C. S. Hsieh, D. S. Tsai, K. K. Tiong, *Appl. Phys. Lett.* 84 (2004) 1552.
82. R. S. Chen, Y. S. Huang, D. S. Tsai, S. Chattopadhyay, C. T. Wu, Z. H. Lan, K. H. Chen, *Chem. Mater.* 16 (2004) 2457.
83. R. S. Chen, Y. S. Huang, Y. M. Liang, D. S. Tsai, K. K. Tiong, *J. Alloys Compd.* 383 (2004) 273.
84. R. S. Chen, H. M. Chang, Y. S. Huang, D. S. Tsai, S. Chattopadhyay, K. H. Chen, *J. Cryst. Growth* 271 (2004) 105.
85. R. S. Chen, C. C. Chen, Y. S. Huang, C. T. Chia, H. P. Chen, D. S. Tsai, K. K.

- Tiong, *Solid State Commun.* 131 (2004) 349.
86. X. Wang, X. Sun, D. Yu, B. Zou, Y. Li, *Adv. Mater.* 15 (2003) 1442.
87. J. Hu, T. W. Odom, C. M. Lieber, *Acc. Chem. Res.* 32 (1999) 435.
88. Y. Xia, P. Yang, Y. Sun, Y. Wu, B. Mayers, B. Gates, Y. Yin, F. Kim, H. Yan, *Adv. Mater.* 15 (2003) 353.
89. G. R. Patzke, F. Krumeich, R. Nesper, *Angew. Chem. Int. Ed.* 41 (2002) 2446.
90. L. C. Chen, S. W. Chang, C. S. Chang, C. Y. Wen, J. J. Wu, Y. F. Chen, Y. S. Huang, K. H. Chen, *J. Phys. Chem. Solids* 62 (2001) 1567.
91. N. G. Chopra, R. J. Luyken, K. Cherrey, V. H. Crespi, M. L. Cohen, S. G. Louie, A. Zettl, *Science* 269 (1995) 966.
92. W. Han, Y. Bando, K. Kurashima, T. Sato, *Appl. Phys. Lett.* 73 (1998) 3085.
93. D. Golberg, W. Han, Y. Bando, L. Bourgeois, K. Kurashima, T. Sato, *J. Appl. Phys.* 86 (1999) 2364.
94. E. Bengu, L. D. Marks, *Phys. Rev. Lett.* 86 (2001) 2385.
95. E. A. Whitsitt, A. R. Barron, *Nano Lett.* 3 (2003) 775.
96. R. Z. Wang, B. Wang, H. Wang, H. Zhou, A. P. Huang, M. K. Zhu, H. Yan, *Appl. Phys. Lett.* 81 (2002) 2782.
97. C. Kimura, T. Yamamoto, T. Sugino, *J. Vac. Sci. Technol. B* 21 (2003) 544.
98. S. Dhara, A. Datta, C. T. Wu, Z. H. Lan, K. H. Chen, Y. L. Wang, C. W. Hsu, L. C. Chen, C. C. Chen, *Appl. Phys. Lett.* 84 (2004) 5473.
99. S. Dhara, A. Datta, C. T. Wu, Z. H. Lan, K. H. Chen, Y. L. Wang, Y. F. Chen, C. W. Hsu, L. C. Chen, H. M. Lin, C. C. Chen, *Appl. Phys. Lett.* 84 (2004) 3486.
100. S. Dhara, A. Datta, C. T. Wu, Z. H. Lan, K. H. Chen, Y. L. Wang, L. C. Chen, C. W. Hsu, H. M. Lin, C. C. Chen, *Appl. Phys. Lett.* 82 (2003) 451.
101. H. M. Kim, D. S. Kim, Y. S. Park, D. Y. Kim, T. W. Kang, K. S. Chung, *Adv. Mater.* 14 (2002) 991.

102. C. C. Chen, C. C. Yeh, *Adv. Mater.* 12 (2000) 738.
103. W. Han, S. Fan, Q. Li, Y. Hu, *Science* 277 (1997) 1287.
104. S. C. Shi, S. Chattopadhyay, C. F. Chen, Z. H. Lan, K. H. Chen, G. M. Hsu, J. S. Hwang, L. C. Chen, accepted, *Appl. Phys. Lett.* (2005).
105. Z. H. Lan, W. M. Wang, C. L. Sun, S. C. Shi, C. W. Hsu, T. T. Chen, K. H. Chen, C. C. Chen, Y. F. Chen, L. C. Chen, *J. Cry. Growth* 269 (2004) 87.
106. C. H. Liang, L. C. Chen, J. S. Hwang, K. H. Chen, Y. T. Hung, Y. F. Chen, *Appl. Phys. Lett.* 81 (2002) 22.
107. R. S. Wagner, W. C. Ellis, *Appl. Phys. Lett.* 4 (1964) 89.
108. Y. Wu, P. Yang, *J. Am. Chem. Soc.* 123 (2001) 3165.
109. E. A. Stach, P. J. Pauzauskie, T. Kuykendall, J. Goldberger, R. He, P. Yang, *Nano Lett.* 3 (2003) 867.
110. D. D. Koleske, A. E. Wickenden, R. L. Henry, J. C. Culbertson, M. E. Twigg, J. *Cryst. Growth* 223 (2001) 466.
111. Z. A. Munir, A. W. Searcy, *J. Chem. Phys.* 42 (1965) 4223.
112. C. L. Hsiao, Ph. D. thesis, Taiwan (2004)
113. Z. W. Pan, Z. R. Dai, Z. L. Wang, *Science* 291 (2001) 1947.
114. S. M. Zhou, Y. S. Feng, L. D. Zhang, *Chem. Phys. Lett.* 369 (2003) 610.
115. B. G. Yacobi, D. B. Holt, *Cathodoluminescence microscopy of inorganic solids*, Plenum press, New York and London, (1990).
116. J. I. Pankove, *Optical process in semiconductors*, Dover Publication, Inc. New York, (1975).
117. S. Nakamura, S. Pearton, G. Fasol, *The blue laser diodes-2nd edition*, Springer, Berlin, (2000).
118. S. Strite, H. Morkoc, *J. Vac. Sci. Technol. B* 10 (1992) 1237.
119. G. W. King, *Spectroscopy and Molecular Structure*, Holt, Rinehart and Winston,

New York, 1964.

120. F. H. Spedding, R. F. Stamm, *J. Chem. Phys.* 10 (1942) 176.
121. N. B. Colthup, L. H. Daly, S. E. Wiberley, *Introduction to Infrared and Raman Spectroscopy*, Academic Press, New York, (1990).
122. L. Liu, J. H. Edgar, *Mater. Sci. Eng. R* 37 (2002) 61.
123. M. Cardona, *Light Scattering in Solids II*, Springer, Berlin, Heidelberg, (1982).
124. C. A. Arguello, D. L. Rousseau, S. P. S. Porto, *Phys. Rev.* 181 (1969) 1351.
125. T. C. Damen, S. P. S. Porto, B. Tell, *Phys. Rev.* 142 (1966) 570.
126. M. Kuball, J. M. Hayes, A. D. Prins, N. W. A. van Uden, D. J. Dunstan, Y. Shi, J. H. Edgar, *Appl. Phys. Lett.* 78 (2001) 724.
127. T. Prokofyeva, M. Seon, J. Vanbuskirk, M. Holtz, S. A. Nikishin, N. N. Faleev, H. Temkin, S. Zollner, *Phys. Rev. B* 63 (2001) 125313.
128. K. Karch, F. Bechstedt, *Phys. Rev. B* 56 (1997) 7404.
129. D. Temple, *Mater. Sci. Eng. R* 24 (1999) 185.
130. S. M Sze, *Physics of Semiconductor Devices*, Wiley, New York, (1981).
131. I. Brodie, P. R Schwoebel, *Proceedings of the IEEE* 82. p1006 (1994).
132. N. A. Cade, R. Johnston, *Proc. 3rd Int. Vacuum Microelectronics Conf.*, Monterey, CA, (1990).
133. R. Greene, H.E Gray, *Proc. 1st Int. Vacuum Microelectronics Conf.*, Williamsburg, VA, (1988).
134. L. M. Baskin, O.I. Lvov, G.N. Fursey, *Phys. Stat. Sol.* 47 (1971) 49.
135. S. Kanemaru, T. Hirano, H. Tanoue, J. Itoh, *J. Vac. Sci. Technol. B* 14 (1996) 1885.
136. K. L. Jensen, *J. Vac. Sci. Technol. B* 13 (1995) 516
137. K. L. Jensen, A. K. Ganguly, *J. Vac. Sci. Technol. B* 11 (1993) 371.
138. C. C. Chen, C. C. Yeh, C. H. Chen, M. Y. Yu, H. L. Liu, J. J. Wu, K. H. Chen,

- L. C. Chen, J. Y. Peng, Y. F. Chen, *J. Am. Chem. Soc.* 123 (2001) 2791
139. R. F. Egerton, *Electron Energy Loss Spectroscopy in the Electron Microscope*, Plenum Press, New York (1986).
140. P. R. Perkes, “Center for high resolution electron microscopy”,
“<http://www.asu.edu/clas/csss/chrem/>”.
141. C. Furetta, *Handbook of thermoluminescence*, River Edge, N. J. (2003).
142. L. Trinkler, B. Berzina, *J. Phys.: Condens. Matter* 13 (2000) 8931.
143. L. Trinkler, L. Bøtter-Jensen, P. Christensen, B. Berzina, *Radiation Measurement* 33 (2001) 731.
144. Jean-Marc Bonard, Jean-Paul Salvetat, Thomas Stöckli, Walt A. de Heer, László Forró, André Châtelain. *Appl. Phys. Lett.*, 73 (1998) 918.
145. C. F. Chen, C. L. Tsai, C. L. Lin, *Diamond Relat. Mater.* 10 (2001) 834
146. H. C. Lo, D. Das, J. S. Hwang, K. H. Chen, C. H. Hsu, C. F. Chen, L. C. Chen, *Appl. Phys. Lett.* 83 (2003) 1420.
147. G. Y. Zhang, X. Jiang, E. G. Wang, *Science* 300 (2003) 472.
148. C. L. Tsai, C. F. Chen, C. L. Lin, *Appl. Phys. Lett.* 80 (2002) 1821.
149. C. C. Striemer, P. M. Fauchet, *Appl. Phys. Lett.* 81 (2002) 2980.
150. J. J. Hickman, D. Ofer, P. E. Laibinis, G. M. Whitesides, M. S. Wrighton, *Science* 252 (1991) 688.
151. V. S. Y. Lin, K. Motesharei, K. P. S. Dancil, M. J. Sailor, M. R. Ghadiri, *Science* 278 (1997) 840.
152. D. Kovalev, V. Y. Timoshenko, N. Kunzner, E. Gross, F. Koch, *Phys. Rev. Lett.* 87 (2001) 68301.
153. F. A. Ponce, D. P. Bour, *Nature* 386 (1997) 351.
154. C. C. Williams, R. C. Davis, P. Neuzil, US patent 1999, 5 969 345.
155. F. G. Tarntair, L. C. Chen, S. L. Wei, W. K. Hong, K. H. Chen, H. C. Cheng, J.

- Vac. Sci. Tech. B 18 (2000) 1207.
156. P. D. Kichambare, F. G. Tarntair, L. C. Chen, K. H. Chen, H. C. Cheng, J. Vac. Sci. Tech. B 18 (2000) 2722.
157. C. H. Hsu, C. F. Chen, H. C. Lo, D. Das, J. Tsai, J. S. Hwang, L. C. Chen, K. H. Chen, Nano Lett. 4 (2004) 471.
158. Q. Wu, Z. Hu, Y. Lu, K. Huo, S. Deng, N. Xu, B. Shen, R. Zhang, Y. Chen, J. Mater. Chem. 13 (2003) 2024.
159. Q. Wu, X. Wang, Y. Chen, Y. Liu, J. Phys. Chem. B 107 (2003) 9726.
160. C. Carlone, K. M. Lakin, H. R. Shanks, J. Appl. Phys. 55 (1984) 4010.
161. R. Di Felice, J. E. Northrup, Phys. Rev. B 54 (1996) R17351.
162. Q. Wu, Z. Hu, X. Wang, Y. Lu, X. Chen, H. Xu, Y. Chen, J. Am. Chem. Soc. 125 (2003) 10176.
163. D. Zhuang, J. H. Edgar, L. H. Liu, B. Liu, L. Walker, MRS Internet J. Nitride Semicond. Res. 7 (2004) 1.
164. Y. Wu, A. Hanlon, J. F. Kaeding, R. Sharma, P. T. Fini, S. Nakamura, J. S. Speck, Appl. Phys. Letts. 84 (2004) 912.
165. R. S. Williams, M. J. Ashwin, T. S. Jones, J. N. Neave, J. Appl. Phys. 95 (2004) 6112.
166. S. C. Shi, C. F. Chen, S. Chattopadhyay, Z. H. Lan, K. H. Chen, L. C. Chen, Adv. Func. Mater. 15 (2005) 781.
167. S. Chattopadhyay, S. C. Shi, Z. H. Lan, C. F. Chen, K. H. Chen, L. C. Chen, J. Am. Chem. Soc. 127 (2005) 2820.
168. D. L. Smith, Thin-Film Deposition: Principles and Practic, McGraw-Hill, New York (1995).
169. J. Tersoff, R. M. Tromp, Phys. Rev. Lett. 70 (1993) 2782.
170. A. M. S. ElAhl, M. He, P. Z. Zhou, G. L. Harris, L. Salamanca-Riba, F. Flet, H. C.

- Shaw, A. Sharma, M. Jah, D. Lakins, T. Steiner, S. N. Mohammad, J. Appl. Phys. 94 (2003) 7749.
171. Y. G. Cao, M. H. Xie, Y. Liu, Y. F. Ng, H. S. Wu, S. Y. Tong, Appl. Phys. Lett. 83 (2003) 5157.
172. M. F. Gyure, J. J. Zinck, C. Ratsch, D. D. Vvedensky, Phys. Rev. Lett. 81 (1998) 4931.
173. M. D. Johnson, C. Orme, A. W. Hunt, D. Graff, J. Sudijono, L. M. Sander, B. G. Orr, Phys. Rev. Lett. 72 (1994) 116.
174. I. V. Markov, Crystal Growth for Beginners, World Scientific, Singapore 1995, Ch. 3.
175. D. Zhuang, J. H. Zdgar, L. H. Liu, B. Liu, L. Walker, MRS Internet J. Nitride Semicond. Res. 7 (2002) 4.
176. S. Kitamura, K. Hiramatsu, N. Sawaki, Jpn. J. Appl. Phys. 34 (1995) L1184
177. L. Tinkler, L. Bøtter-Jensen, B. Berzina, Radiation Protection Dosimetry 100 (2002) 313.
178. H. Hirayama, J. Appl. Phys. 97 (2005) 091101.
179. X. Tang, F. Hossain, K. Wongchotigul, M. G. Spencer, Appl. Phys. Lett. 72 (1998) 1501.
180. J. A. Freitas, Jr., G. C. B. Braga, E. Silveira, J. G. Tischler, M. Fatemi, Appl. Phys. Lett. 83 (2003) 2584.
181. E. Silveira, J. A. Freitas, Jr., M. Kneissl, D. W. Treat, N. M. Johnson, G. A. Slack, L. J. Schowalter, Appl. Phys. Lett. 84 (2004) 3501.
182. E. Kuokstis, J. Zhang, Q. Fareed, J. W. Yang, G. Simin, M. A. Khan, R. Gaska, M. Shur, C. Rojo, L. Schowalter, Appl. Phys. Lett. 81 (2002) 2755.
183. J. Li, K. B. Nam, M. L. Nakarmi, J. Y. Lin, H. X. Jiang, Appl. Phys. Lett. 83 (2003) 5163.

184. M. Benabdesselam, P. Iacconi, D. Lapraz, P. Grosseau, B. Guilhot, *J. Phys. Chem.* 99 (1995) 10319.
185. L. Trinkler, B. Berzina, S. C. Shi, L. C. Chen, M. Benabdesselam, P. Iacconi, *Phys. Stat. Sol. C2* (2005) 334.
186. L. Chen, B. J. Skromme, R. F. Dalmau, R. Schlessner, Z. Sitar, C. Chen, W. Sun, J. Yang, M. A. Khan, M. L. Nakarmi, J. Y. Lin, H. X. Jiang, *Appl. Phys. Lett.* 85(2004) 4334.
187. R. A. Youngman, J. H. Harris, *J. Am. Ceram. Soc.* 73 (1990) 3238.
188. N. Teofilov, K. Thonke, R. Sauer, D. G. Ebling, L. Kirste, K. W. Benz, *Diamond Relat. Mater.* 10 (2001) 1300.
189. Y. Shishkin, R. P. Devaty, W. J. Choyke, F. Yun, T. King, H. Morkoç, *Phys. Status Solidi A* 188 (2001) 591.
190. M. Strassburg, J. Senawiratne, N. Dietz, U. Haboeck, A. Hoffmann, V. Noveski, R. Dalmau, R. Schlessner, Z. Sitar, *J. Appl. Phys.* 96 (2004) 5870.
191. S. C. Shi, C. F. Chen, S. Chattopadhyay, K. H. Chen, L. C. Chen, *Appl. Phys. Lett.* 87 (2005) 073109.
192. Q. Zhao, H. Zhang, X. Xu, Z. Wang, J. Xu, D. Yu, G. Li, F. Su, *Appl. Phys. Lett.* 86 (2005) 193101.
193. R. A. Youngman, J. H. Harris, D. A. Chernoff, in *Ceramic Transactions*, Vol. 5, (edited by W. S. Young, G. L. McVay, G. E. Pike), American Ceramic Society, Westerville, OH, 1989.
194. T. Onuma, S. F. Chichibu, T. Sota, K. Asai, S. Sumiya, T. Shibata, M. Tanaka, *Appl. Phys. Lett.* 81 (2002) 652.
195. J. Chen, W. Z. Shen, H. Ogawa, Q. X. Guo, *Appl. Phys. Lett.* 84 (2004) 4866.
196. B. Berzina, L. Trinkler, J. Sils, K. Atobe, *Radiation Effects Defects in Solids*, 157 (2002) 1089.

197. G. A. Slack, *J. Phys. Chem. Solids*, 34 (1973) 321.
198. S. Nie, S. R. Emory, *Science* 275 (1997) 1102.
199. K. Kneipp, Y. Yang, H. Kneipp, L. T. Parleman, I. Itzkan, R. R. Dasari, M. S. Feld, *Phys. Rev. Lett.* 78 (1997) 1667.
200. H. Xu, E. J. Bjerneld, M. Kall, L. Borjesson, *Phys. Rev. Lett.* 83 (1999) 4357.
201. M. Fleishmann, P. J. Hendra, A. J. McQuillan, *Chem. Phys. Lett.* 26 (1974) 163.
202. M. Moskovits, *Rev. Mod. Phys.* 57 (1985) 783.
203. E. Betzig, R. J. Chichester, *Science* 262 (1993) 1422.
204. X. S. Xie, R. C. Dunn, *Science* 265 (1994) 361.
205. R. Geßner, C. Winter, P. Rösch, M. Schmitt, R. Petry, W. Keifer, M. Lankers, J. Popp, *Chem. Phys. Chem.* 5 (2004) 1159.
206. D. A. Higgins, J. K. Kerimo, D. A. vanden Bout, P. F. J. Barbara, *Am. Chem. Soc.* 118 (1996) 4049.
207. D. Birnbaum, S. K. Kook, R. J. J. Kopelman, *Phys. Chem.* 97 (1993) 3091.
208. W. Tan, Z. Y. Shi, S. Smith, D. Birnbaum, R. Kopelman, *Science* 258 (1992) 778.
209. R. Petry, M. Schmitt, J. Popp, *Chem. Phys. Chem.* 4 (2003) 14.
210. F. Ni, T. M. Cotton, *Anal. Chem.* 58 (1986) 3159.
211. R. P. Van Duyne, J. C. Hulteen, D. A. Treichel, *J. Chem. Phys.* 99 (1993) 2101.
212. V. L. Schlegel, T. M. Cotton, *Anal. Chem.* 63 (1991) 241.
213. S. Miller, A. Baiker, M. Meier, A. J. Wokaun, *Chem. Soc. Faraday Trans. I* 80 (1984) 1305.
214. L. M. Sudnik, K. L. Norrod, K. L. Rowlen, *Appl. Spectrosc.* 50 (1996) 422.
215. L. Gunnarsson, E. J. Bjerneld, H. Xu, S. Petronis, B. Kasemo, M. Kall, *Appl. Phys. Lett.* 78 (2001) 802.
216. M. Green, F. M. Liu, *J. Phys. Chem. B* 107 (2003) 13015.
217. R. Zenobi, V. Deckert, *Angew. Chem. Int. Ed.* 39 (2000) 1746.

218. P. Hildebrandt, M. Stockburger, *J. Phys. Chem.* 88 (1984) 5935.
219. F. J. Garcia-Vidal, J. B. Pendry, *Phys. Rev. Lett.* 77 (1996) 1163.
220. B. Nikoobakht, J. Wang, M. A. El-Sayed, *Chem. Phys. Lett.* 366 (2002) 17.
221. H. Dai, J. H. Hafner, A. G. Rinzler, D. T. Colbert, R. E. Smalley, *Nature* 384 (1996) 147.
222. M. Y. Jung, D. W. Kim, S. S. Choi, *Microelectron. Eng.* 53 (2000) 399.
223. E. S. Snow, P. M. Campbell, J. P. Novak, *J. Vac. Sci. Technol. B* 20 (2002) 822.
224. V. V. Zhirnov, G. J. Wojak, W. B. Choi, J. J. Cuomo, J. J. Hren, *J. Vac. Sci. Technol. A* 15 (1997) 1733.
225. D. Kang, V. V. Zhirnov, R. C. Sanwald, J. J. Hren, J. J. Cuomo, *J. Vac. Sci. Technol. B* 19 (2001) 50.
226. C. J. Lee, T. J. Lee, S. C. Lyu, Y. Zhang, H. Ruh, H. J. Lee, *Appl. Phys. Lett.* 81 (2002) 3648.
227. Z. S. Wu, S. Z. Deng, N. S. Xu, Jian Chen, J. Zhou, Jun Chen, *Appl. Phys. Lett.* 80 (2002) 3829.
228. T. H. Yang, C. H. Chen, A. Chatterjee, H. Y. Li, J. T. Lo, C. T. Wu, K. H. Chen L. C. Chen, *Chem. Phys. Lett.* 379 (2003) 155.
229. F. G. Tarntair, C. Y. Wen, L. C. Chen, J.-J. Wu, K. H. Chen, P. F. Kuo, S. W. Chang, Y. F. Chen, W. K. Hong, H. C. Cheng, *Appl. Phys. Lett.* 76 (2000) 2630.
230. C. L. Tsai, C. F. Chen, C. L. Lin, *J. Appl. Phys.* 90 (2001) 4847.
231. M. C. Kan, Ph. D thesis, 2003.
232. J. M. Bonard, J. P. Salvetat, T. Stockli, W. A. de Heer, L. Forro, A. Chatelain, *Appl. Phys. Lett.* 73 (1998) 918.
233. J. M. Bonard, F. Maier, T. Stockli, A. Chatelain, W. A. de Heer, J. P. Salvetat, L. Forro, *Ultramicroscopy* 73 (1998) 7.
234. Z. W. Pan, F. C. K. Au, H. L. Lai, W. Y. Zhou, L. F. Sun, Z. Q. Liu, D. S. Tang, C.

- S. Lee, S. T. Lee, S. S. Xie, J. Phys. Chem. B, 105 (2001) 1519.
235. K. Okano, S. Koizumi, S. R. P. Silva, G. A. J. Amaratunga, Nature 381(1996) 140.
236. B. S. Satyanarayana, A. Hart, W. I. Milne, J. Robertson, Appl. Phys. Lett. 71 (1997) 1430.
237. W. B. Choi, J. Liu, M. T. McClure, A. F. Myers, V. V. Zhirnov, J. J. Cuomo, J. J. Hren, J. Vac. Sci. Technol. B 14 (1996) 2050.
238. M. W. Geis, J. C. Twichell, T. M. Lyszczarz, J. Vac. Sci. Technol. B 14(1996) 2060.
239. Y. Show, F. Matsuoka, M. Hayashi, H. Ito, M. Iwase, T. Izumi, J. Appl. Phys. 84 (1998) 6351.
240. H. Yamashita, K. Fukui, S. Misawa, S. Yoshida, J. Appl. Phys. 50 (1979) 896.
241. V. M. Bermudez, T. M. Jung, K. Doverspike, A. E. Wickenden, J. Appl. Phys. 79 (1996) 110.
242. Semiconductor Physics and Devices, Donald A. Neamen, Second Edition, McGraw-Hill (2003), p328.
243. C. S. Chang, S. Chattopadhyay, L. C. Chen, K. H. Chen, C. W. Chen, Y. F. Chen, R. Callazo, Z. Sitar, Phys. Rev. B 68 (2003) 125322.

Publication list

(I) Paper

1. S. C. Shi, C. F. Chen, S. Chattopadhyay, Z. H. Lan, K. H. Chen, L. C. Chen, "Growth of single-crystal wurtzite aluminum nitride nanotips with self-selective apex angle", *Adv. Func. Mater.* 15 781 (2005).
2. S. C. Shi, C. F. Chen, S. Chattopadhyay, K. H. Chen, L. C. Chen, "Field emission from quasi-aligned aluminum nitride nanotips", *Appl. Phys. Lett.* 87, 073109 (2005).
3. S. C. Shi, C. F. Chen, G. M. Hsu, J. S. Hwang, S. Chattopadhyay, Z. H. Lan, K. H. Chen, L. C. Chen, "Reduced temperature quenching of photoluminescence from indium nitride nanotips grown by metalorganic chemical vapor deposition", *Appl. Phys. Lett.* accepted (2005).
4. S. C. Shi, S. Chattopadhyay, C. F. Chen, K. H. Chen, L. C. Chen, "Structural Evolution of AlN Nano-structures: Nanotips and Nanorods", *Chem. Phys. Lett.* accepted (2005).
5. S. Chattopadhyay, S. C. Shi, Z. H. Lan, C. F. Chen, K. H. Chen, L. C. Chen, "Molecular Sensing with Ultrafine Silver Crystals on Hexagonal Aluminum Nitride Nanorod Templates", *J. Am. Chem. Soc.* 127 (2005) 2820.
6. L. Trinkler, B. Berzina, S. C. Shi, L. C. Chen, M. Benabdesselam, P. Iaconi, "UV light induced luminescence processes in AlN nanotips and ceramics", *Phys. Stat. Sol. C2* (2005) 334.
7. Y. C. Cheng, C. M. Wu, C. C. Yang, G. A. Li, A. Rosenauer, K. J. Ma, S. C. Shi, L. C. Chen, "Effects of interfacial layers in InGaN/GaN quantum-well structures on their optical and nanostructural properties", *J. Appl. Phys.* 98 (2005) 014317.
8. Y. C. Cheng, E. C. Lin, C. M. Wu, C. C. Yang, J. R. Yang, A. Rosenauer, K. J. Ma, S. C. Shi, L. C. Chen, C. C. Pan, J. I. Chyi, "Nanostructures and carrier localization behaviors of green-luminescence InGaN/GaN quantum-well structures of various silicon-doping conditions", *Appl. Phys. Lett.* 84, 2506 (2004).
9. C. H. Hsu, S. C. Shi, C. F. Chen, "Growth of chromium carbide capped-carbon nanotip using bias-assisted microwave plasma chemical vapor deposition", *Thin solid film* 469 (2004) 131.

10. Z. H. Lan, W. M. Wang, C. L. Sun, S. C. Shi, C. W. Hsu, T. T. Chen, K. H. Chen, C. C. Chen, Y. F. Chen, L. C. Chen, "Growth mechanism, structure and IR photoluminescence studies of indium nitride nanorods", J. Cry. Growth 269 (2004) 87.
11. C. L. Lin, C. F. Chen, S. C. Shi, "Field emission properties of aligned carbon nanotubes grown on stainless steel using CH₄/CO₂ reactant gas", Diam. & related mater. 13 (2004) 1026.
12. C. M. Chen, M. Chen, F. C. Leu, S. Y. Hsu, S. C. Wang, S. C. Shi, C. F. Chen, "Purification of multi-walled carbon nanotubes by microwave digestion method", Diam. & related mater. 13 (2004) 1182.
13. M. Chen, C. M. Chen, S. C. Shi, C. F. Chen, "Low-temperature synthesis multiwalled carbon nanotubes by microwave plasma chemical vapor deposition using CH₄-CO₂ gas mixture", Japan. J. Appl. Phys. 42 (2003) 214.



(II) Conference

1. S. C. Shi, C. F. Chen, K. H. Chen, L. C. Chen, "Structural and Optical Properties of In_xAl_{1-x}N, and In_xGa_{1-x}N Nanowires Grown by Metalorganic Chemical Vapor Deposition", The International Conference On Metallurgical Coatings And Thin Films (ICMCTF), 2003, **Oral presentation**.
2. S. C. Shi, C. F. Chen, K. H. Chen, L. C. Chen, "Growth and field emission properties of quasi-aligned aluminum nitride nanotips", 14th European Conference on Diamond, Diamond-like Materials, Carbon Nanotubes, Nitrides and Silicon Carbide, 2003.
3. S. C. Shi, C. F. Chen, K. H. Chen, L. C. Chen, "Structural, Optical and Field Emission Properties of AlN Nanotips", The International Conference On Metallurgical Coatings And Thin Films (ICMCTF), 2004, **Oral presentation**.
4. S. C. Shi, C. F. Chen, K. H. Chen, L. C. Chen, "Oxygen Implantation Induced Defect Luminescence in AlN Nanotips", 15th European Conference on Diamond, Diamond-like Materials, Carbon Nanotubes, Nitrides and Silicon Carbide, 2004.

作者簡歷

姓 名： 施 士 塵 (Shih-Chen Shi)

性 別： 男

出生日期： 民國 66 年 9 月 1 日

籍 貫： 台灣省花蓮縣

學 歷： 國立成功大學機械工程學系畢業 (84-88)

國立成功大學機械工程研究所碩士畢業 (88-90)

國立交通大學材料科學與工程研究所博士畢業 (90-94)



論文題目： 一維奈米氮化鋁的製備與光電特性分析

Synthesis and Characterization of One-Dimensional AlN
nanostructures